Preparation and Magnetoelectric Effect of Multiferroic Cobalt Ferrite-Barium Titanate Composites

Der Fakultät für Ingenieurwissenschaften der Universität Duisburg-Essen

Abteilung Bauwissenschaften

zur Erlangung des akademischen Grades

Doktor der Ingenieurwissenschaften

eingereichte Dissertation von

M. Sc. Morad Etier

aus Al-Ramtha

Tag der mündlichen Prüfung: 14 August, 2015

Gutachter:

Prof. Dr. rer. nat. Doru C. Lupascu

Prof. Dr. rer. nat. Heiko Wende

ACKNOWLEDGMENTS

I thank several people because of their collaboration in the success of this project especially in the laboratories on the Essen and Duisburg campuses. Sincere thanks for my advisor professor Lupascu for the continuous support from the first step of the project to the end. He was always supporting by suggestions, ideas and even in practical experiments. I am also grateful to Dr. Vladimir Shvartsman who provided me the experimental skills especially in magnetic and magnetoelectric experiments. He was also spending his time to me in reading, analyzing, modifying, and improving the experiments. Great thanks that I would like to send Yanling Gao for a powerful experimental help specially in chemical synthesizing and procedures. A lot of thanks should be sent to Prof. Wende and his group who gave me the opportunity to access his labs easily and at any time. The efforts of Dr. Carolin Schmitz-Antoniak in beam-line measurements are strongly acknowledged. Special thanks should be sent to Joachim Landers and Soma Salamon for their assistance in SQUID measurement. The assistance of Mrs. Anna Yelsukova in TEM measurement is also acknowledged. Also I have a huge respect to the technical supports offered by Patrick Dubray, I thank him because he was providing all equipment and stuff that I needed. Special thanks to my friends in the department, they were the best supporters. The financial support from DAAD-GRISEC program (Grant 50750877) and Deutsche Forschungsgemeinschaft via Forschergruppe 1509 Ferroic Functional Materials during the Ph.D period is highly acknowledged.

DECLARATION

Herein, I do declare that this thesis is a product of my own original work without any help from a third party or other aids apart from those listed. Thoughts, ideas, and information taken or used from others or previously published ideas have been correctly cited and acknowledged in the references. Further, all persons who helped me with the sorting and interpretation of material used in this thesis have been clearly acknowledged. Otherwise, no further people were involved in this work. In particular, I neither obtained the help of a Ph.D. consultant nor pay a third party for any work related to the content of this thesis. This work has never been presented to an examining authority in this or any similar form for an award of academic qualification, and it has not been published in this or any similar form anywhere else. I never presented any other thesis of mine to an examining authority in this or any similar form for an award of the academic degree of Doctors of Engineering. I confirm that I accept the doctoral guidelines of the Faculty of Engineering of the University of Duisburg-Essen.

Morad Etier

ZUSAMMENFASSUNG

Herstellung und magnetoeletrischer Effekt an multiferroischen Kobaltferrit/Bariumtitanat Kompositen

Von

M. Sc. Morad Etier

Universität Duisburg-Essen, Essen, 2015

Magnetoelektrische Materialien sind vielversprechend durch potenzielle Anwendungsgebiete für neuartige und effiziente Technologien z.B. im Bereich der Mikroelektronik. Das Schalten von elektrischer Polarisation durch Magnetfelder bzw. von Magnetisierung durch elektrische Felder ist eines der höchsten Ziele für magnetoelektrische Materialien. In Laufe dieses Dissertationsprojekts wurden multiferroische und magnetoelektrische $CoFe_2O_4$-$BaTiO_3$ Komposite durch den neuartigen Ansatz der Organsolmethode hergestellt und untersucht. Zunächst wurden $CoFe_2O_4$ Nanopulver (30-40 nm) mithilfe der Kopräzipitation hergestellt. Hierbei wird die Partikelgröße hauptsächlich durch die Menge des zugegebenen Fällungsmittels beeinflusst. Verschiedene Zusammensetzungen von $CoFe_2O_4$-$BaTiO_3$ nanopartikulären Core-Shell-Strukturen mit $CoFe_2O_4$ Anteilen von 20, 30, 40, 50 und 70 % wurden erfolgreich durch die Kombination der Kopräzipitation und der Organosolmethode hergestellt. Die Core-Shell-Partikel hatten eine durchschnittliche Größe von 112±18 nm.

Diese Core-Shell-Nanopartikel wurden gesintert, wodurch keramische Komposite vom Typ (0-3) hergestellt wurden. Ein Komposit vom Typ (3-0) wurde mithilfe von Spark-Plasma-Sintern erhalten. Korrelationen zwischen dielektrischen und magnetischen Eigenschaften und deren Auswirkung auf die magnetoelektrischen Eigenschaften werden diskutiert. Der magnetoelektrische Effekt wurde umfassend charakterisiert, wobei der Effekt in Abhängikeit von Temperatur, magnetischen Gleichfeld und Probenorientierung gemessen wurde. Der direkte magentoelectrische Effekt wurde über die Lock-In Technik für verschiedene Proben gemessen, wobei dieser mit dem konversen Effekt gemessen an einem SQUID Suszeptometer verglichen wurde. Der maximale direkte und konverse magnetoelectrische Effekt wurde für Proben mit 50 % $BaTiO_3$ mit 3.2 mV/cm·Oe bzw. 25 ps/m gemessen. Es wurde festgestellt, dass der magnetoelektrische Effekt von Elektrische Widerstand und Polung der Proben abhängt. Der magnetoelektrische Effekt als Funktion der Temperatur in $CoFe_2O_4$-$BaTiO_3$ Kompositen folgt dem Trend der Permittivität und erreicht das Maximum beim Phasenübergang von rhomboedrscher zu tetragonaler Struktur für Bariumtitanat. Als Funktion des magnetischen Feldes folgt der Effekt hingegen dem piezomagnetischen Koeffizienten von Kobaltferrit. Die Abhängigkeit der Polarisation vom Magnetfeld an der Probenoberfläche wurde für (0-3) und (3-0) Komposite mithilfe von linearem und zirkularem Röntgendichoismus gemessen.

ABSTRACT

Preparation and Magnetoelectric Effect of Multiferroic Cobalt Ferrite-Barium Titanate Composites

By

M. Sc. Morad Etier

University of Duisburg-Essen, Essen, 2015

Interesting technological applications and the efficiency of magnetoelectric materials nowadays make them a special topic for more scientific investigations. In memories fabrication, the switching of polarization and magnetization by magnetic and electric fields is the ultimate goal for magnetoelectric effect materials. In this dissertation, the multiferroic $CoFe_2O_4$-$BaTiO_3$ magnetoelectric composite was synthesized using the organsol method. First the $CoFe_2O_4$ nanopowder (30-40nm) was successfully synthesized using the co-precipitation method. The particle sizes were mainly affected by the addition of the precipitation agent. Composites of $CoFe_2O_4$-$BaTiO_3$ core shell structure nanoparticles were successfully synthesized using a combination of the co-precipitation and the organosol method. The core shell particle size was distributed in the range of 112±18 nm. The phase contents of $CoFe_2O_4$ with respect to $BaTiO_3$ were chosen to 20, 30, 40, 50 and 70 percent. The core shell nanoparticles were sintered in order to form dense (0-3) ceramic samples.

For comparison, a (3-0) connectivity was fabricated using spark plasma sintering. The correlation between dielectric, magnetic, and ferroelectric properties on the magnetoelectric effect is discussed. A comprehensive magnetoelectric effect measurement was presented for different compositions. The effect of temperature, dc magnetic field, and sample orientation on the ME effect were illustrated. The direct magentoelectric effect was measured using the lock-in technique for different samples. The values of the direct magnetoelectric effect were compared to the converse ME measured in a SQUID susceptometer. It was found that the maximum direct and converse ME effects are recorded for the sample of 50% $BaTiO_3$ with values 3.2 mV/cm·Oe and 25 ps/m, respectively. The ME effect was found to be composition dependent and mainly affected by resistivity and the poling state of the samples. The difference between the two values can be related to the permittivity value that is used in the conversion between them and the discharging process which reduces the effective polarization in the direct measurement. For the dependence of the ME effect on temperature, it was found that the magnetoelectric effect in $CoFe_2O_4$-$BaTiO_3$ composites tracks the permittivity values and shows a maximum effect at the orthorhombic/tetragonal phase transition of barium titanate. For the ME effect dependence of dc magnetic field, it was found that the effect tracks the cobalt ferrite piezomagnetic coefficient dependence of dc magnetic field. The magnetic field dependence of electric polarization at the surface was measured for both (0-3) and (3-0) connectivity using X-ray absorption spectroscopy and its associated linear and circular dichroisms. In spite of low coupling value of the (3-0) in the macroscopic scale, it showed larger electric polarization dependence of magnetic field extracted by X-ray Linear Dichroism (XLD) measurements.

LIST OF PUBLICATIONS

[1] **M. Etier**, Y. Gao, V. V. Shvartsman, A. Elsukova, J. Landers, H. Wende, and D. C. Lupascu, $CoFe_2O_4/BaTiO_3$ core/shell nanoparticles, *Ferroelectrics 2012; 438: 115-122*.

[2] **Morad Etier** , Vladimir V. Shvartsman, Yanling Gao, Joachim Landers, Heiko Wende, and Doru C. Lupascu, Converse magnetoelectric effect in (0-3) $CoFe_2O_4$-$BaTiO_3$(20/80) composite ceramics prepared by the organosol route, *Ferroelectrics 2013; 448: 77-85*.

[3] **M. Etier**, V. V. Shvartsman, F. Stromberg, J. Landers, H. Wende, and D. C. Lupascu, Synthesis and magnetic properties of $CoFe_2O_4$ nanoparticles. *Mater. Res. Soc. Symp. Proc. 2012; 1398*.

[4] **Morad Etier**, Vladimir V. Shvartsman, Yanling Gao, Joachim Landers, Heiko Wende, and Doru C. Lupascu, Magnetoelectric properties of $0.2CoFe_2O_4$-$0.8BaTiO_3$ composite prepared by the organosol route. *ISAF/ECAPD/PF, 2012 Intl. symp. DOI: 10.1109/ISAF.2012.6297820*.

[5] M. Labusch , **M. Etier** , D. C. Lupascu , J. Schröder , M. Keip. Product Properties of a two-phase magneto-electric composite: Synthesis and numerical modelling. *Comput. Mech. 2014; 54: 71-83*.

[6] Doru C. Lupascu, HeikoWende, **M. Etier**, Ahmadshah Nazrabi, Irina

Anusca, Harsh Trivedi, Vladimir V. Shvartsman, Joachim Landers, Soma Salamon and Carolin Schmitz-Antoniak. Measuring the Magnetoelectric Effect Across Scales. *GAMM-Mitt.;2015; 38[1]:25-74*.

[7] **Morad Etier**, Carolin Schmitz-Antoniak, Soma Salamon, Harsh Trivedi, Yanling Gao,Ahmadshah Nazrabi, Joachim Landers, Devendraprakash Gautam, Markus Winterer, Detlef Schmitz, Heiko Wende, Vladimir V. Shvartsman and Doru C. Lupascu. Magnetoelectric coupling on multiferroic cobalt ferrite-barium titanate ceramic composites with different connectivity schemes. *Acta Materialia; 2015; 90:1-9*.

CONFERENCES

[1] **M. Etier**, V. V. Shvartsman, Y. Gao, H. Trivedi, J. Landers, S. Salamon, I. Anusca, A. Nazrabi, H. Wende, J. Schröder, M. Labusch, M.-A. Keip and D. C. Lupascu Magnetoelectric coupling of biphasic $CoFe_2O_4$-$BaTiO_3$ (0-3) particulate composite, invited speaker in *Electroceramic XIV, 16-20 Juni, 2014, Bucharest, Romania.*

[2] **M. Etier**, V. V. Shvartsman, H. Trivedi, S. Salamon, H. Wende and D. C. Lupascu Direct and converse magnetoelectric coupling in cobalt ferrite-barium titanate (0-3) particulate composite, *International symposium of application of piezoelectrics ISAF, 12-16 May, 2014, Penn state, USA.*

[3] **M. Etier**, V. V. Shvartsman, Y. Gao , D. Gautam, J. Landers H. Wende and D. C. Lupascu Multiferroic $CoFe_2O_4$/ $BaTiO_3$ from core shell nanoparticles to (0-3) ceramic composite, *Euro Intelligent Materials, 25-27 September 2013, Kiel-Geramany.*

[4] **M. Etier**, V. V. Shvartsman, Y. Gao , J. Landers H. Wende and D. C. Lupascu Multiferroic $CoFe_2O_4$/ $BaTiO_3$ with core shell structure nanoparticles, *Deutsche Physikalische Gesellschaft (DPG), 9-15 March 2013, Regensburg-Germany.*

[5] **M. Etier**, V. V. Shvartsman, Y. Gao , J. Landers H. Wende and D. C. Lupascu (Magnetoelectric Properties of $BaTiO_3$-$CoFe_2O_4$ (80/20) Composite Prepared by the Organosol Route, *Functional Ferrroic Material (FFM-2012), 21-22 November 2012 Dortmund-Germany.*

[6] **Morad Etier**, Vladimir V. Shvartsman, Frank Stromberg, Joachim Landers, Heiko Wende, Fbio G. Figueiras, Doru C. Lupascu Synthesis and magnetic properties of cobalt ferrite nanoparticles , *DPG (Deutsche Physikalische Gesellschaft), 25-30 March 2012, Berlin-Germany.*

[7] **Morad Etier**, Yaling Gao,Vladimir Shvartsman, Anna Elsukova, Joachim Landers, Heiko Wende and Doru Lupascu Multiferroic cobalt ferrite barium titanate core shell nanoparticles prepared by organosol method, *ISAF-ECAPD-PFM 201, 9-13 July 2012, Aveiro-Portugal.*

LIST OF SYMBOLS

Symbol	Meaning	SI Units
P	Polarization	C/m^2
P_i	Ionic polarization	C/m^2
P_e	Electronic polarization	C/m^2
P_o	Orientation polarization	C/m^2
H	Magnetic field strength	A/m
B	Magnetic induction	T
M	Magnetization	A/m
χ	Magnetic susceptability	-
E	Electric field	V/m
T_c	Curie Temperature	K
λ_{ij}	Magnetostrictive strain	-
d_{ijk}	Piezoelectric coefficient	m/V
q_{ijk}	Piezomagnetic coefficient	m/A
Q_{ijkl}	Electrostriction coefficient	m^4/C^2
X_{ij}	Stress	N/m^2
x_{ij}	Strain	-
c_{ijkl}	Stiffness	N/m^2
ME_H	Direct magnetoelectric effect	s/m
ME_E	Converse magnetoelectric effect	s/m
P_s	Saturation polarization	C/m^2
P_r	Remnant polarization	C/m^2
E_c	Coercive electric field	V/m
E_s	Saturation electric field	V/m
M_s	Saturation magnetization	A/m
M_r	Remnant magnetization	A/m
H_c	Coercive magnetic field	A/m
α_{33}	Longitudinal magnetoelectric coefficient	s/m
α_{31}	Traverse magnetoelectric coefficient	s/m
α	Magnetoelectric coupling coefficient	s/m
t	Sample thickness	m
μ_o	Permeability of free space	H/m
μ_{ij}	Magnetic permeability	H/m
M_{ME}	Induced magnetic moment	A/m
E_{ac}	AC electric field	V/m

Symbol	Meaning	SI Units
a	Lattice constant	m
c	Lattice constant	m
n	Number of windings	-
R	Radius	m
H_T	True magnetic field	T
H_d	Demagnetization field	T
N_d	Demagnetization factor	-
N_{ijkl}	Magnetostrictive coefficient	kg^2/A^2m^4
I	Current	A
δ^+, δ^-	Charges in orientation polarisation	C
ϵ_r	Material relative permittivity	-
ϵ_o	Free space permittivity	F/m
γ_{ijk}	Higher order ME effect	s/V
β_{ijk}	Higher order ME effect	s/A
Z	Impedance	Ω
λ	X-ray wave length	Å
k	Shape factor	-
C	Capacitance	F
A	Electrode area	m^2
ω	Angular frequency	rad/s
f	Frequency	Hz
Φ	Magnetic flux	Wb
s	Inversion parameter	-
β_l	Line broadening at half maximum intensity	radian
θ	Bragg angle	radian
D	Particle size	m
Γ	Full line length at half maximum	m/s
δ	Isomer shift	m/s
Δ	Quadrapole splitting	m/s
B_{hf}	Magnetic hyperfine field	T
μ_B	Bohr magneton moment	Am^2

LIST OF ABBREVIATIONS

Abbreviation	description
ME	Magnetoelectric
AFM	Atomic Force Microscopy
MFM	Magnetic Force Microscopy
PFM	Piezo Force Microscopy
SPS	Spark Plasma Sintering
SEM	Scanning Electron Microscopy
SAED	Selected Area Electron Diffraction
HRTEM	High Resolution Transmission Electron Microscopy
FFT	Fast Fourier Transformation
XRD	X-ray Diffraction
SQUID	Superconducting Quantum Interference Device
FE	Ferroelectric
FM	Ferromagnetic
MRI	Magnetic Resonance Imaging
PLD	Pulsed laser deposition
XLD	x-ray Linear Dichroism
XMCD	X-ray Magnetic Circular Dichroism
XANES	X-ray Absorption Near Edge Structure
HZB	Helmholtz-Zentrum Berlin

TABLE OF CONTENTS

LIST OF FIGURES

LIST OF TABLES

DEDICATION

To my wife and children, Tharaa, Banan, Leen and Karam.

1. INTRODUCTION

1.1 Framing the dissertation

I divided the dissertation into main chapters. In chapter one I discussed the main terminologies which are related to multiferroics and the magnetoelectric effect as well as the state of art, motivations, objectives, and the importance of this study. I listed in chapter two the main technological instruments that were used in this project including brief descriptions of their importance and their relation to the experimental part. As a starting point chapter three explains different characterizations of $CoFe_2O_4$ nanoparticles such as synthesizing method, morphology, and characteristics and magnetic properties. Chapter four explains the new method of synthesizing core shell nanoparticles of $CoFe_2O_4$ and $BaTiO_3$. This chapter explains the structural characteristics of the nanoparticles as well as ferroelectric and ferromagnetic properties. Chapter five shows an analysis of the microstructure of different composite ceramic samples. The sintering routes, the connectivity type, and the resistivity are also analyzed. I show the atomic force microscopy scans for different samples in this chapter. A comparison in magnetic properties is also done in addition to the impedance and the leakage analysis. In chapter six a comprehensive analysis of magnetoelectric coupling measurement techniques is presented. Different methods of measuring the magnetoelectric effects are explained and discussed. A comprehensive analysis and differences between the direct and the converse ME coupling are discussed in this chapter, as well as dichroic x-ray absorption spectroscopy and its linear and circular dichroisms. In the last chapter a summary of the most important outcomes is listed.

1.2 Preface

Nowadays, it is important to look for the future in the way of investigating new materials and developing new composites and advanced materials. These materials can be used for a new generation of sensors and efficient data storage techniques. Among them, multiferroic materials are the main choice because they exhibit electric, magnetic, and piezoelectric properties. These properties can be coupled/connected to each other resulting in new effects that can be used in different applications [1, 2]. People or inventors are willing to reduce the size of all communication tools and going forward into the nanotechnology. Ferroelectric and ferromagnetic materials are one choice for the manufacturing of the new computers hard disks and non-volatile random access memories. The development of the new magneteoelectric materials results in new technological applications. Different groups have suggested and fabricated different devices based on magnetoelectrics. The main applications are found in the field of sensors, memories, current/voltage converstors, energy harvestors, and electric field tunable devices [3–14], **Figure (1.1)** illustrates all possible applications of the ME materials. In spite of fabricating and prototyping most of these applications, 4-state logic gate or random access memories based on magnetoelectric effect are still theoretical studies and need more researches in order to convert them into reality.

In some materials, the application of a magnetic field causes a change in material electrical resistivity which is denoted as magnetoresistance. Recently, it has been proposed that the use of the magnetoeletric effect rather than magnetoresistance effect is better where in magnetoelectric materials the electric field and magnetic field are coupled in the same material so that the energy stored are easier to convert and control [15]. The advantages of using magnetoelectric rather than magnetoresistive effect first is: (1) keeping the sensitivity of the device by reducing the thickness of the sensor (2) elimination of permanent magnets for horizontal biasing and (3) reduction of power consumption

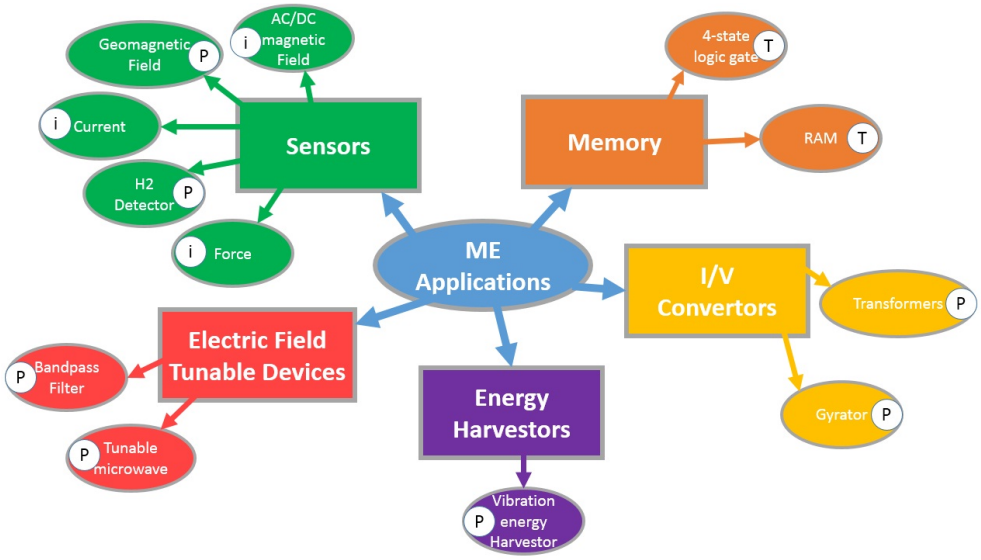

Fig. 1.1: Main applications of magnetoelectric materials, the letters beside each device mean [i: the device is in the market, P still prototype and T means still theoretical study].

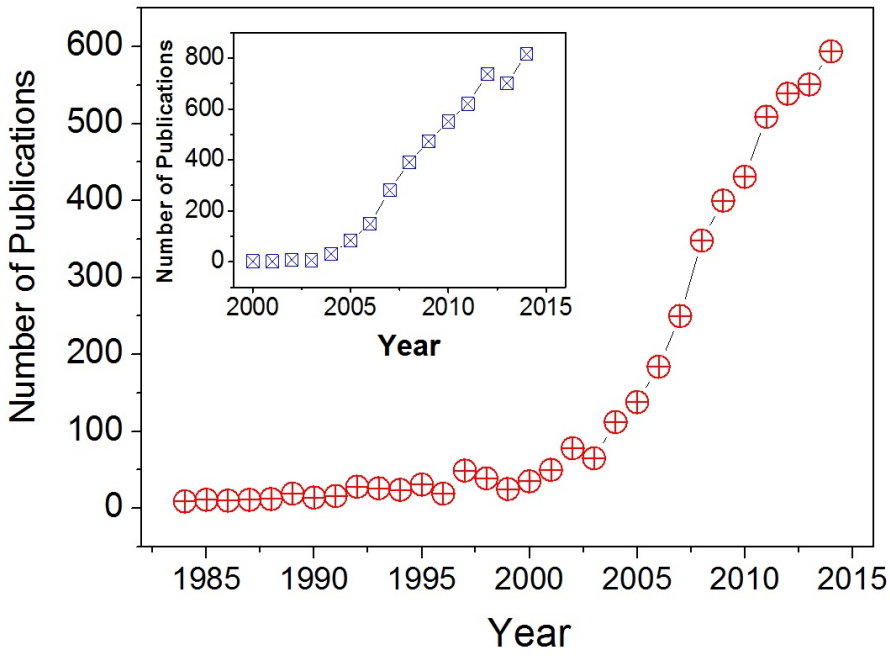

Fig. 1.2: Number of publications per year according the website Web of Knowledge using keyword "Magnetoelectric", the inset shows number of publications for keyword "Multiferroic".

which can remove the usability of dc current in the sensor, for example in the case of reading head of magnetoresistance material, the data is read back as a voltage which causes a thermal heating and energy consumption [15]. Many researchers focused on the magnetoelectric (ME) effect for both single-phase materials for example Cr_2O_3 and $RMnO_3$ (R=rare earth element), and composite materials, like $CoFe_2O_4$-$BaTiO_3$ and $NiFe_2O_4$-$BaTiO_3$ have also been studied. Magnetoelectric materials are the most promising candidates for the new spintronic devices which can control the magnetic state for the material by an electric field [16] and also the new sensors which can be used as a magnetic field detector replacing SQUIDs with a room temperature system. [17]. **Figure (1.2)** illustrates the importance of the topic nowadays where the number of publications has been increasing rapidly starting in 2005 and reached about 600 publications per year in 2014 for the topic magnetoelectric. The inset in the figure shows the number of publication per year for the keyword multiferroic. In the upcoming sections of this chapter, some important terms and works related to mutliferroics and the magnetoelectric effect are introduced and discussed.

1.3 Multiferroics, definition and applications

In spite that the first magnetoelectric material Cr_2O_3 (which is not a multiferroic) was synthesized by Astrov in 1960 [18], the exact term multiferroic was first used by Schmid in 1994. He focused on the primary ferroic orders: ferroelectricity, ferromagnetism, ferroelasticity, and ferrotoroidicity. Multiferroics are materials that have two or more ferroic orders in the same phase [19]. The most interesting mutliferroics are those that exhibit ferroelectric and ferromagnetic orders. The symmetry consideration is very important in multiferroics where the inversion symmetry is broken for ferroelectrics and ferrotoroids and preserved for ferromagnets and ferroelastics. **Table (1.1)** shows the dependency of the four ferroic orders on inversion and time reversal

symmetry operations [20]. There are many multiferroic single phase materials such as the perovskite compounds like $BiFeO_3$, the multiferroics with formula $RMnO_3$ (R is the rare earth element such as Lu, Sc), the boracites like $Cr_3B_7O_{13}Cl$, barium fluoride compounds such as $BaMgF_4$ [21–23], etc..

Tab. 1.1: Classification of the primary ferroic orders and their dependency on inversion symmetry and time reversal [20].

Order	Parameter	Stimulus	Inversion symmetry	Time reversal
Ferroelectric	Polarisaion	Electric field	Broken	Preserved
Ferromagnetic	Magnetization	Magnetic field	Preserved	Broken
Ferroelastic	Deformation	Stress	Preserved	Preserved
Ferrotoroidic	Toroidal moment	Source vector	Broken	Broken

Classification of single phase multiferroic materials was introduced by Khomskii in 2009 [23]. Perovskite multiferroics belong to the first group. He focused on the ferroelectric properties of the materials, the reason of ferroelectricity, and the mechanism of magnetism in single phase materials. For example the ferroelectricity in $BiFeO_3$ comes from the lone electron pair in the 6s orbital of the Bi^{+3} ion. The magnetic properties come from Fe^{+3} ions. In the second classification, ferroelectricity comes from charge ordering, like in $TbMn_2O_5$. In the third type, ferroelectricity comes from a geometric ferroelectricity . For example, in $YMnO_3$ it is caused by tilting the MnO_5 blocks which caused closer packing so that the oxygen ions are moved nearer to the Y^- ion [23].

In case of composite multiferroics, the multiferroic properties appear when combining two materials, for example a ferroelectric with a ferromagnet, or a ferroelectric with an aniferromagnet. Different composite mutliferroics have been synthesized and studied such as e.g. ferrimagentic $CoFe_2O_4/NiFe_2O_4$ with ferroelectric $BaTiO_3$ [24] or lead zirconium titanate (PZT) [25], other composite systems are $Fe_3O_4/BaTiO_3$ [26] or $PZT/La_{0.7}Sr_{0.3}MnO_3$ [27].

Potential applications of multiferroics come from the magnetoelectric materials applications such as magnetic tunnel junctions, weak magnetic field detectors [28] and quaternary logic memory [29]. The multiferroic tunnel junc-

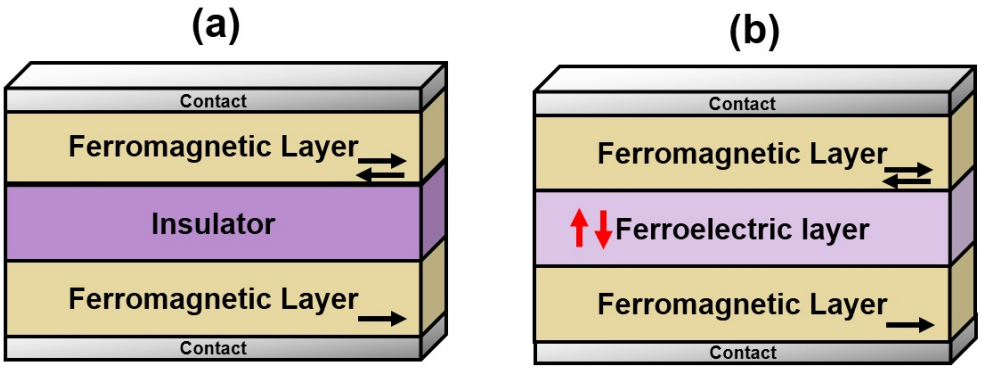

Fig. 1.3: Schematic representation of tunnel junctions (a) magnetic tunnel junction (b) multiferroic tunnel junction

tion rather than the magnetic tunnel junction is the most important potential application see **Figure (1.3.a)**. Two ferromagnetic layers are separated by an insulator. The magnetic configuration for the two layers can be altered by applying a magnetic field. When applying the electric field using the upper and lower contact, the electrons may pass from layer to the other if the magnetization of the two layers is in the same direction. If the magnetization state in the two layers are aniparallel that may prevent the electrons to pass. These two states represent the situation of high and low resistivity of the layers. In case of multiferroic tunnel junction **Figure (1.3.b)**, a ferroelectric layer plays the important role as the tunneling barrier. The resistivity of the layers may exist in four states rather than in two states in case of magnetic tunnel junction where the magnetization of the magnetic layers can be switched using magnetic field and also the polarization in ferroelectric layer can be switched using electric field [30].

1.4 Ferromagnetism and ferrimagnetism

Magnetization is a vector which corresponds to the sum of all induced and permanent magnetic moments in a material per unit volume. The magnetic dipole moments are the moments or the torques that are produced by the application of a magnetic field and as a result of the resulting magnetic forces. The origin of magnetic moments comes from the moments generated by the

individual electrons in the atom. They can be divided into three main sources, first is the moment generated when the electron is rotating around the nucleus, that causes a small magnetic moment perpendicular to the rotating plane. The second source of a magnetic moment comes from the spin of the electron itself which is denoted by Bohr magneton μ_B and the third one is the change in the orbital moments induced when an external magnetic field is applied. In SI units the vector magnetic flux density ($\vec{B}$) for a magnetic material placed in a magnetic field ($\vec{H}$) is:

$$\vec{B} = \mu_o(\vec{H} + \vec{M}) \tag{1.1}$$

where

$\vec{B}$=magnetic flux density in T

μ_o=free space magnetic permeability = 1.256637×10^{-6} in T·m/A

$\vec{H}$=magnetic field strength in A/m

$\vec{M}$=magnetization in A/m

The degree of magnetization of a certain material can be indicated by the magnetic susceptibility (χ) where:

$$\chi = \partial M/\partial H \tag{1.2}$$

Therefore, the magnetic susceptibility and its magnetic field and temperature dependencies χ(T,H) determine the magnetic behavior for different magnetic materials. Different types of magnetism are found in material science and classified according to response of atomic magnetic dipoles to the application of external magnetic field. For example, *diamagnetic* materials like copper, silver and lead are the materials that possess magnetization only when an external magnetic field is applied and creates magnetic moments in the opposite direction, typical negative susceptibility values are 10^{-4}-10^{-6}. These magnetic moments come from the change in spin orbital moment induced by

an applied magnetic field. *Paramagnetic* materials are materials that linearly react with external magnetic field like aluminum, tungsten and lithium. The source of magnetism in these materials are the spin moments and their orbital momentum about the nucleus. The typical susceptibility values are 10^{-3}-10^{-5}. The susceptibility of a paramagnetic material depends on the inverse of temperature by the Curie law:

$$\chi(T) = C/T \tag{1.3}$$

where C is the Curie constant and T is temperature. *Ferromagnets* are another type of magnetic materials. These materials posses spontaneous magnetization in the absence of an external magnetic field. The major source of magnetization of these materials is the magnetization which comes from the spin of the electron in comparison to the weak effect from the orbital magnetic moments contribution. Ferromagnetic materials are different from paramagnetic and diamagnetic materials in several aspects, first the exchange coupling between neighboring moments will lead them to align parallel to each other. Second, the ferromagnetic materials follow the Curie-Weiss law:

$$\chi = C/(T - T_c) \tag{1.4}$$

where T_c is the Curie temperature. The magnetic moments are ordered at temperatures below the Curie temperature, but above the Curie temperature, the magnetic ordering is lost and the material shows paramagnetic behavior. Ferromagnetic materials include cobalt, nickel and iron. The existence of the spontaneous magnetic moments in the ferromagnetic materials suggests that electron spins and magnetic moments are arranged in a regular manner as shown in **Figure 1.4** [31]. The adjacent spins can also be aligned in antiparallel direction producing a zero net moment at zero magnetic field, these materials are *antiferromagnets* which include chromium, iron manganese and nickel oxide. In case of *ferrimagnetic* materials, some of the adjacent spin

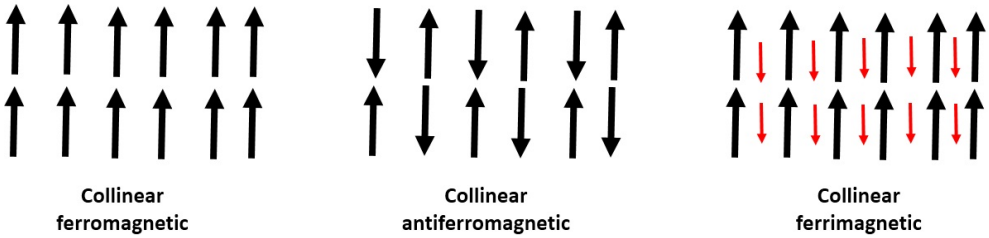

Fig. 1.4: Electron spin arrangements [31]

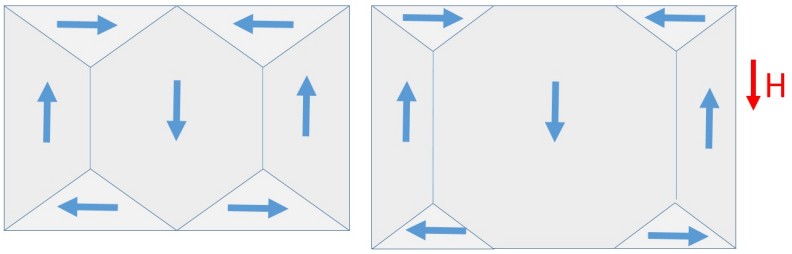

Fig. 1.5: Schematic representaion of magnetic domains before and after applying external magnetic field

moments are pointed in the opposite direction with unequal magnitude of the magnetic moments so that the spontaneous magnetization remains, these materials include iron oxide, cobalt ferrite and nickel ferrite.

The magnetic *domains* are defined as the regions inside the ferromagnetic material with a uniform magnetization. When an external magnetic field is applied to the sample, the domain walls are altered and the domains are aligned in the same direction of the magnetic field. Domains are separated by domain boundaries or domain walls, these walls separate two domains with different magnetization directions (see **Figure (1.5)**). The domains are arranged in a way that the overall magnetostatic energy of the system is minimized. The application of an external magnetic field will cause a growth of the magnetic domains.

It is important here to specify that when we ensure all of the domains are aligned in the same direction or in the direction of the magnetic field, we reach a *saturation magnetization* usually indicated by the symbol M_s as shown in **Figure (1.6)**. When applying more magnetic field (H), no further increase of magnetization happens, because all of the magnetic moments are aligned

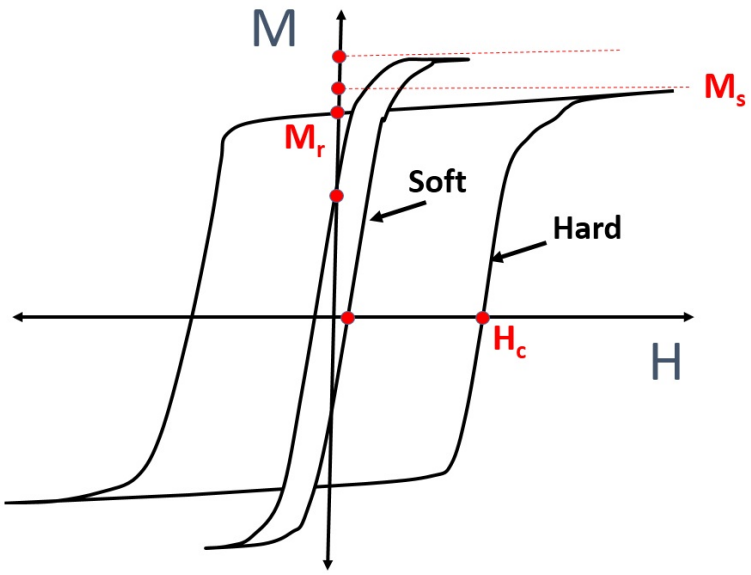

Fig. 1.6: Example of magnetic hysteresis loop for both hard and soft magnets.

in the direction of the field. When the external field is removed and returns to zero, ferromagnetic material keeps some *remnant magnetization* (M_r) see **Figure (1.6)**. The squareness value which is calculated by M_r/M_s is usually used to illustrate how square the loops is and the amount of remaining magnetization after removing the field. In fact, the squareness value can also provide information about the magnetocrystalline anisotropy and the exchange interaction. To reach negative magnetization we need a magnetic field applied in the opposite direction in order to cancel all the remnant magnetization of the material at the *coercive field* (H_c) . The values of coercive field depend on the magnetic material (hard, soft) and the magnetic structure. The difference between hard and soft magnetic materials is illustrated in **Figure (1.6)**. In case of hard magnetic material, the coercive field, the remnant magnetization and the magnetic dissipated energy are larger than in a soft one. These materials can keep their magnetism even after removing the applied magnetic field so that they are usually used as permanent magnet.

To illustrate the difference between ferromagnetism and ferrimagnetism, let us take iron oxide Fe_3O_4 as an example. It contains both Fe^{+2} and Fe^{+3} ions . The Fe^{+2} ions are located in octahedral sites. The Fe^{+3} ions can be located on

both octahedral and tetrahedral sites. The magnetic moments of the ions Fe^{+3} in the octahedral sites are antiparallel to the moments of the Fe^{+3} ions on the tetrahedral sites. This causes a reduction of the net magnetization. In addition to ferromagnetics, the term antiferromagnetism describes magnetic materials where the magnetic moments are aligned in opposite directions. In this case the total magnetic moment is equal to zero. Examples of antiferromagentic materials include chromium oxide and manganese oxide.

1.5 Ferroelectricity and piezoelectricity

The phenomenon ferroelectricity was discovered in 1921 by J. Valasek for Rochelle Salt (Potassium Sodium Nitrate) [32]. Ferroelectricity indicates materials that have a crystal structure which allow spontaneous polarization. The polarization direction can be altered by an external electric field. The polarization is defined as the total electric dipole moment divided by the volume. One can distinguish between different types of polarization, the electronic, ionic, and orientation polarization as shown in **Figure (1.7)**. The *electronic* polarization comes from dipole moment induced via a displacement (d) between the positive and negative charge in an atom under an electric field. The electronic polarization is denoted by the symbol P_e. In ionic materials, which contain cations and anions as shown in **Figure (1.7.b)**, the electric field may cause an extension of bonds resulting in the displacement of the ionic sublattices in opposite directions. The *ionic* polarization is denoted by the symbol P_i. The third source of polarization comes from the *orientation* polarization P_o which occurs in molecules that have permanent dipole moments as shown in **Figure (1.7.c)** by the arrows. In these molecules there is always a separation between the partial charges (δ^+, δ^-). The dipoles may be aligned in the direction of the electric field developing a net polarization of the material.

In some materials, a fourth type of polarization may also occur which is called *space charge* polarization. This kind of polarization can be produced

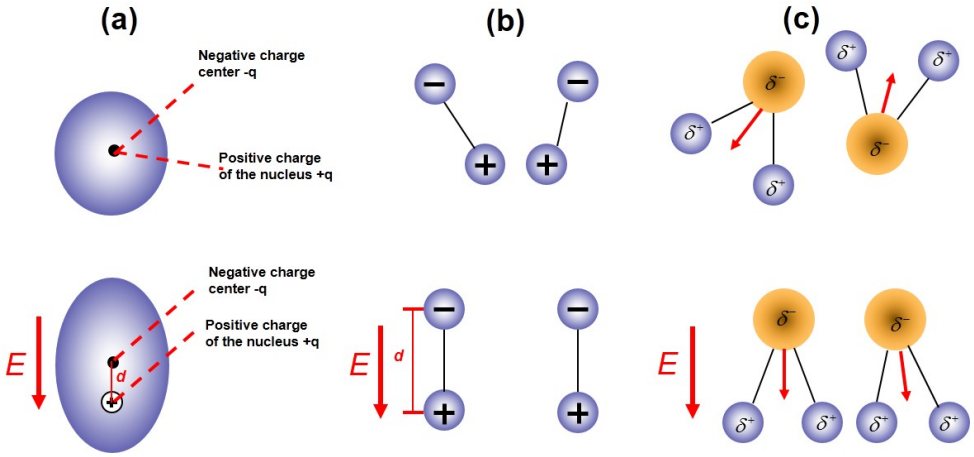

Fig. 1.7: Mechanism of polarization showing (a) Electronic polarization (b) ionic polarization (c) orientation polarization

by free charge carriers. When the movement of these charge carriers is impeded by interfaces, pores or grain boundaries, space charge is produced.

Ferroelectric materials can be used in different kinds of applications such as in random access memories (RAM), pyroelectric detectors, ultrasonic sensors and actuators. F. Jona and G. Shirane classified ferroelectrics into four main categories [33]:

- according to crystal-chemical classification: such as the hydrogen-bonded crystals like KH_2PO_4 and rochelle salt or the double oxides like $BaTiO_3$ and $PbTa_2O_6$
- according to the number of directions allowed to the spontaneous polarization: such as single axis of the spontaneous polarization like Rochelle salt and KH_2PO_4 or crystals with polarization along several axes like $BaTiO_3$ and $Cd_2Nb_2O_7$.
- according to the existence or lack of a center of symmetry in the non-polar phase: for example non-centrosymmetrical paraelectric phase as Rochelle salt and KH_2PO_4, the centrosymmeterical non-polar phase such as $BaTiO_3$ and $Cd_2Nb_2O_7$.
- according to the phase changes with respect to the Curie temperature for

example a transition of order-disorder type like KH_2PO_4 and transition of the displacive type such as $BaTiO_3$.

Like ferromagnets, ferroelectrics may consist of domains, the regions where the direction of the spontaneous polarization is uniform. The domain borders separate the different domains from each other. Usually in ferroelectrics, not all of the domains are aligned in the same direction and they need an external electrical field to be aligned as illustrated in **Figure (1.8)**. Ferroelectrics usually contain many domains so the net polarization is close to zero in the not poled state. These domains can be classified by the angle between the polarization in adjacent domains. For example 180^o indicates anti-parallel domains. Below the Curie point, any ferroelectric is in the polar state whether it is poled or not. The domains grow in the direction of the applied electric field that forces them to reorient as shown in **Figure (1.8.b)**. This process is called poling. A single domain state in a single crystal can be reached by poling if the mechanical constrains will permit it (see **Figure (1.8.c,d)**). In the poling process a suitable field, temperature, and time should be applied. The external poling field must be larger than the coercive field in order to align the domains. Of course the poling process needs more attention, because it depends on the resistivity of the poled sample, the temperature, the thickness of the sample and the value of the applied field so that a breakdown may occur to the sample, if the sample could not sustain this field.

The ferroelectric state appears after cooling below the Curie temperature. For example in $BaTiO_3$, at temperatures above the Curie temperature (T_c=393K) the crystal structure is cubic where Ba^{+2} ions are located at the corners of the cube and O^{-2} at the faces and Ti^{+4} at the center (see **Figure 1.9)**. At temperatures below T_c, the structure becomes tetragonal and the Ti^{+4} ions and O^{-2} move slightly relative to each other causing a dipole moment along one of cube edges.

The polarization hysteresis loop can be measured e.g. by a Sawyer-Tower

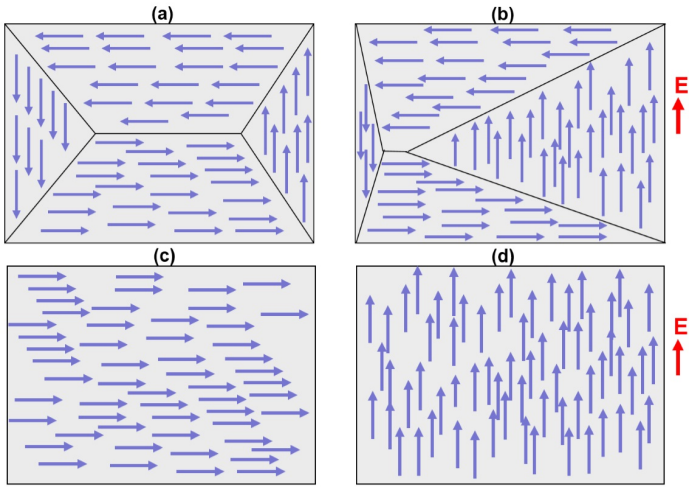

Fig. 1.8: Ferroelectric material shows 90° and 180° domain walls (a) before poling (b) after partial poling (the typical case in ceramics) and (c) before poling (d) complete poling only present in single phase crystals, the arrows show the polarization directions.

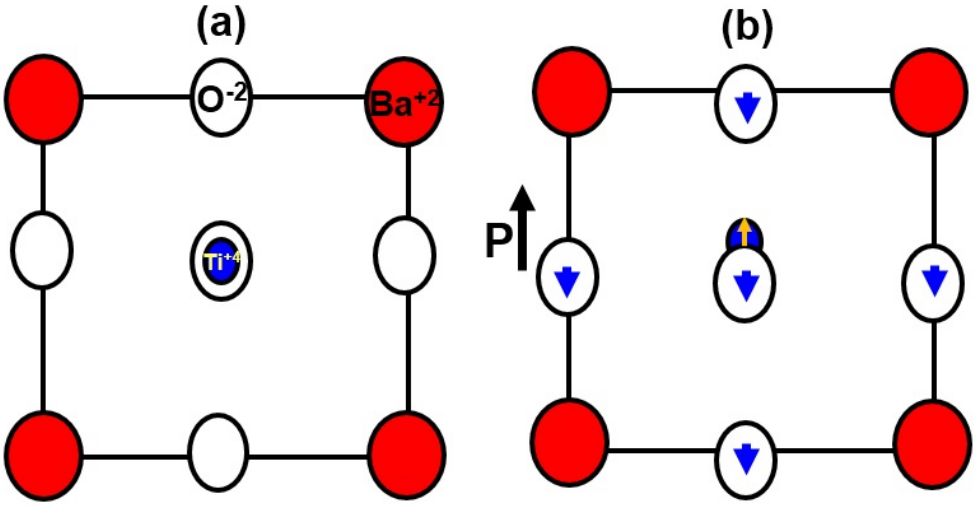

Fig. 1.9: Side view of (a) cubic and (b) tetragonal $BaTiO_3$.

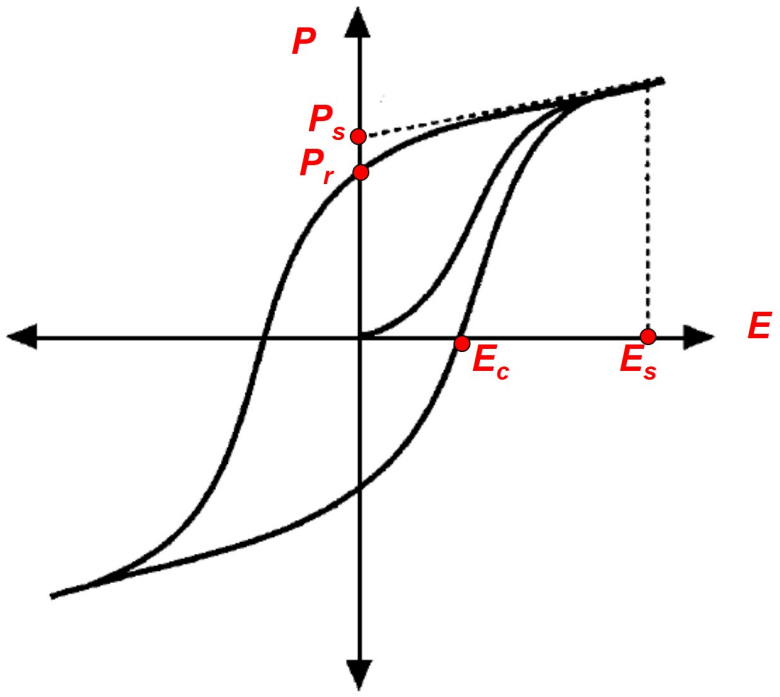

Fig. 1.10: Polarization-electric field hysteresis loop in polycrystalline ferroelectrics.

circuit [34] by plotting the polarization for the ferroelectric specimen versus the applied electric field which will be described in detail in chapter two. If a certain field was applied for a specimen and then decreased to zero, the domains of the ferroelectric material are still polarized and the sample has a *remnant polarization* P_r as shown in **Figure (1.10)**. This remnant polarization depends on the domain state existing in the crystal. Polarization of the sample can be reduced to zero when applying an electric field in the opposite direction and this field is called *coercive field* (E_c). When reaching the point that all domains are in the same direction this is called *saturation polarization* (P_s) and that can happened at a certain electric field called *saturation field* (E_s). Typically polycrystalline samples only permit partial poling, so that the saturation polarization for polycrystalline samples is much lower than for single crystal [35].

The phenomenon of *piezoelectricity* was discovered by Pierre and Jacques Curie in 1880. They noted that the crystals of tourmaline, quartz, topaz, cane sugar, and Rochelle salt produce surface charges when subjected to a

mechanical stress. Piezoelectric material is the material that can generate voltage when applying a mechanical stress and also it can produce strain when subjected to an electric field. Many industrial applications nowadays use piezoelectric materials such as quartz watches, dampers, sensors, printers etc..

The *direct piezoelectric effect* which describes a linear relation between applied stress and induced electric displacement, can be described by the following linear equation [36]:

$$D_i = d_{ijk} X_{jk} \tag{1.5}$$

where d_{ijk} is a third rank tensor expressing piezoelectricity, D_i is the induced electric displacement, and X_{jk} is the stress applied. The *converse piezoelectric effect* results from the relation between the strain and the electric field where:

$$x_{ij} = d_{kij} E_k \tag{1.6}$$

where the electric field here E_k is a vector and x_{ij} is the strain which is a second rank tensor. In terms of symmetry, there are 21 point groups that do not have a center of symmetry, and 20 of them, except point group (432), allow piezoelectricity [37]. Among these 20 point groups, 10 allow ferroelectricity so all ferroelectrics are piezoelectrics at the same time.

1.6 Magnetoelectric effect

1.6.1 Magnetoelectric effect definition, units and applications

The magnetoelectric effect was conjectured in 1894 [38] but the name magnetoelectric was formulated by Debye in 1926 [39]. In thermodynamics, it is important to study the relations between electrical, mechanical and magnetic properties for a certain material. These relations can be illustrated by the *Heckmann diagram* shown in **Figure (1.11)**. The mechanical properties indicate the relationship between stress (X) and strain (x) in terms of elasticity

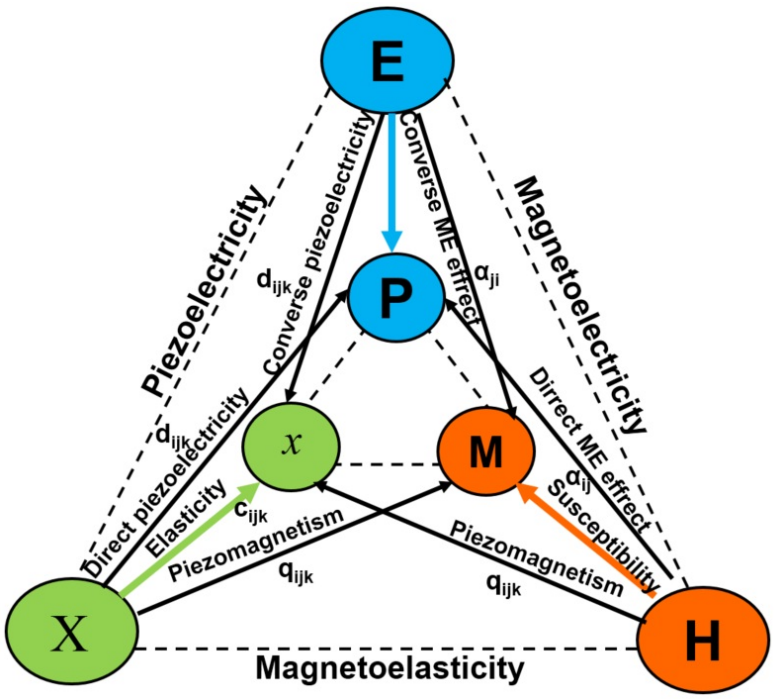

Fig. 1.11: Heckmann diagram showing the relation between electrical, mechanical and magnetic properties of a material, the stress X and the strain x are denoted in some books by σ and ϵ respectively [Reproduced from [40]].

as the principal effect. The electrical properties describe polarization response P to an electric field E, and the magnetic properties are the magnetization response M with respect to magnetic field H.

Electric field, magnetic field and stress can also be connected among each other defining the *coupling coefficients* in a linear approximation. For example, in piezoelectric materials a stress can produce an electric polarization which is the direct piezoelectric effect and an electric field can produce a strain in case of the converse piezoelectric effect. Some materials can change their shape with elongation or contraction according to the magnetic field via the piezomagnetic effect. It is commonly known that the magnetic field (H) can control magnetization (M) and the electric field (E) can control polarization (P), and the stress (X) can control strain (x). When we can control polarization by magnetic filed and control the magnetization by electric field, we speak of the magnetoelectric effect (ME).

The history of the ME studies and the development of single phase ME ma-

terials is summarized in **Table (1.2)**. Thanks to Röntgen who knew that a moving dielectric can be magnetized by the application of an electric field [41]. The inverse effect was then discovered in 1905 by Wilson, he found that the polarization of a dielectric can be changed in a magnetic field [42]. The name of magnetoelelctric only appeared in 1926 by Debye [39]. The experimental results of electric field induced magnetization in Cr_2O_3 was found by Astrov in 1960 [18] and the magnetic field induced polarization were confirmed by Rado and Folen in 1961 [43, 44]. In 2003, Kimura et al. discovered the ferroelectricity in perovskite manganite $TbMnO_3$ [45]. They found that the spin frustration causes sinusoidal antiferromagnetic ordering. The revival of the magnetoelectric effect occurred by Fiebig in 2005 who presented a comprehensive study and extensive review of the magnetoelectric research development particularly in the context of the manganites [46]. Recently, creative studies have been done concerning the experimental and theoretical investigation for bulk and nanostructured magnetoelectric composites [2, 47, 48].

Tab. 1.2: History of the ME effect for single phase materials [46]

Year	Event	Reference
1888	Moving dielectric are magnetized when placed in electric field	[41]
1894	Intrinsic ME effect was predicted	[38]
1905	Polarisation of a moving dielectric in a magnetic field	[42]
1922	First static experiment for ME effect (unsuccessful)	[49, 50]
1926	The name magnetoelectric appeared	[39]
1959	Violation of time-reversal symmetry of Cr_2O_3	[51]
1960	ME response allowed in time-asymmetric media	[52]
1961	Magnetic field induced polarization in Cr_2O_3	[43, 44]
1963-1964	ME effect of TiO_3, $GaFeO_3$ and other materials	[53, 54]
2003	ME effect in manganites	[45]
2005	Revival of the Magnetoelectric effect	[46]

1.6.2 Converse and direct magnetoelectric effect

In principle, two magnetoelectric coefficients and their inverses can be extracted from the Heckmann diagram shown in **Figure (1.11)**. These coefficients relate either magnetic field with polarization or electric field with magnetization. They are the coupling coefficients between the intensive fields, E or H and the corresponding extensive variables, M and P, respectively [55]. The values of the two coefficients should be identical due to Maxwell's relations [2]. The cross coefficients:

$$\alpha_{ij}^{P} = \frac{dP_i}{dH_j} \tag{1.7}$$

which is called the magnetoelectric polarization coefficient. In the case of intrinsic multiferroic it is numerically identical to the converse magnetoelectric coefficient:

$$\alpha_{ij}^{M} = \frac{\mu_o dM_i}{dE_j} = \alpha_{ji}^{P} \tag{1.8}$$

In literature, the symbols (α_D) and (α_C) have been used for α_{ij}^{P} and α_{ij}^{M} for direct and converse magnetoelectric coefficients, respectively. These two coefficients are measured by completely different measurement setups. The magnetoelectric effect can also be described by the magnetoelectric voltage coefficient which is a different coefficient in the Heckmann diagramm:

$$\alpha_{ij}^{E} = \frac{dE_i}{dH_j} \tag{1.9}$$

This equation couples the two intensive material properties, E and H. In the linear system, the equation should be identical to the coupling between the two extensive variables μ_oM and P. Including the free space and relation for the field follows from Maxwells relations [2, 56, 57]:

$$\alpha'_{ij} = \frac{dB_j}{dD_i} \tag{1.10}$$

where D is the dielelctric displacement. The new symbol α' here is the magnetoelectric susceptibility tensor, it is related to the cross coefficients through the dielectric constant where:

$$\alpha^P_{ij} = \epsilon_o \epsilon^r_{ik} \cdot \alpha'_{kj} \tag{1.11}$$

where ϵ^r_{ik} here is the relative dielectric permittivity tensor. It should be mentioned here that this equation is applicable for single phase multiferroics but still argumentative in composites because of difficulty to define which dielectric constant should be used.

Often, ME measurements are done for a capacitor plate geometry when the voltage produced is measured in the sample according to applied magnetic field where:

$$\alpha_E = \frac{\partial V}{t \cdot \partial H} \tag{1.12}$$

Where V is the voltage produced in the sample with thickness t when applying a magnetic field H. The magnetoelectric coefficient is unitless in cgs and has unit of s/m in SI. The magnetoelectric measurements depend on the direction of the applied fields and measured response regarding the sample geometry. For example the longitudinal magnetoelectric effect is measured across the sample thickness when the electric field, polarization, and the magnetic field are perpendicular to the sample surface. The transverse magentoelectric effect is measured across the sample thickness when the applied electric field and the polarization are perpendicular to the sample surface when the magnetic field is parallel to it. However, some authors used the term in-plane ME effect when the magnetic field is perpendicular to the polarization direction and the term out of plane ME effect when it is in the same direction with polarization.

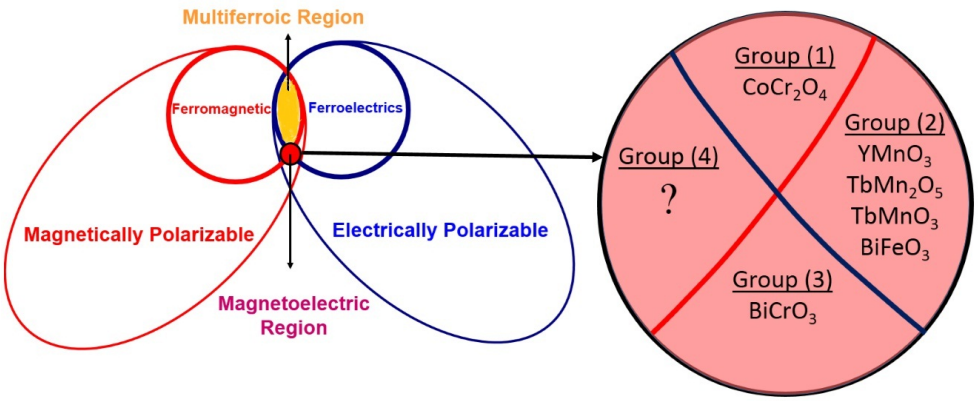

Fig. 1.12: The link between magnetoelectric and multiferroic in single phase materials. The circle in the right is a zoom of magnetoelectric region, reproduced from [2].

1.6.3 Theory of the magnetoelectric effect

In order to distinguish between mutliferroic and magnetoelectric materials, **Figure (1.12)** shows the relationship between them. The electrically polarizable materials may include, ferroelectrics, paraelectrics and antiferroelectrics. The magnetically polarizable materials consist of ferromagnets, paramagnets and antiferromagnets. The intersections between the two circles (ferroelectric and ferromagnetic circles) with orange color are the multiferroics. The magnetoelectric materials are located in the small circle in the figure in pink color are the materials that can be ferroelectric and ferromagnet like $CoCr_2O_4$ in groupe 1 in **Figure (1.12)**, or the materials that are ferroelectric but not ferromagnet such as $YMnO_3$ and $BiFeO_3$. These materials are also electrically and magnetically polarizable (see group 2 in the figure). Another type of magnetoelectric materials is shown in group 3 in **Figure (1.12)**. These materials are not ferroelectric nor ferromagnet but still electrically and magnetically polarizable such as $BiCrO_3$. To the date of submission this thesis, materials in group 4 are still missing, the materials which are ferromagnet but not ferroelectric, and are electrically and magnetically polarizable. We can say that not all of multiferroics are magnetoelectric and also not all magnetoelectric materials are multiferroics.

For more explanation in a thermodynamic context, materials in general under external fields of $\vec{E}$ and $\vec{H}$ have a free energy expressed as [46]:

$$\begin{aligned} F(\vec{E},\vec{H}) = F_o - P_i^S E_i - M_i^S H_i - \frac{1}{2}\epsilon_o\epsilon_{ij}E_iE_j - \frac{1}{2}\mu_o\mu_{ij}H_iH_j \\ -\alpha_{ij}E_iH_j - \frac{1}{2}\beta_{ijk}E_iH_jH_k - \frac{1}{2}\gamma_{ijk}E_iE_jH_k \end{aligned} \tag{1.13}$$

Differentiation of this equation result in polarization and magnetization as follows:

$$P_i(\vec{E},\vec{H}) = -\frac{\partial F}{\partial E_i} = P_i^S + \epsilon_o\epsilon_{ij}E_j + \alpha_{ij}H_j + \frac{1}{2}\beta_{ijk}H_jH_k + \gamma_{jik}E_jH_k \tag{1.14}$$

$$\mu_o M_i(\vec{E},\vec{H}) = -\frac{\partial F}{\partial H_i} = M_i^S + \mu_o\mu_{ij}H_j + \alpha_{ji}E_j + \beta_{jik}E_jH_k + \frac{1}{2}\gamma_{ijk}E_iE_j \tag{1.15}$$

Here M_i^S and P_i^S are the spontaneous magnetization and polarization, respectively. Magnetic and electric susceptibility are expressed by μ_{ij} and ϵ_{ij}. The linear magnetoelectric effect is expressed by the tensor α_{ij} . The higher order magnetoelectric effect appears when the coefficients β_{ijk} and γ_{ijk} are $\neq 0$. The linear magnetoelectric effect can be expressed as:

$$P_i(\vec{E},\vec{H}) = \alpha_{ij}H_j \tag{1.16}$$

$$\mu_o M_i(\vec{E},\vec{H}) = \alpha_{ji}E_j \tag{1.17}$$

where **Equation (1.16)** represents the direct and **(1.17)** the converse effect. For the linear ME effect, α_{ij} for the direct effect is equal to the converse one in intrinsic multiferroics and the linear approximation. The linear magnetoelectric coupling coefficient is limited by magnetic permeability and dielectric

permittivity [58] where:

$$\alpha_{ij} \leq \sqrt{\epsilon_{ii}\mu_{jj}} \tag{1.18}$$

However, large permittivity value is not an important condition for a material to be ferroelectric and also it is not necessary for ferromagnet to have large permittivity, and consequently, a large magnetoelectric coupling is not restricted to multiferroics [2]. In composites or in two phase systems, the magnetoelectric effect is produced by strain mediated via the interface between the piezomagnetic and piezoelectric phases so that the strength of the coupling in this case is not restricted by **Equation (1.18)**.

1.6.4 Single phase magnetoelectric materials

The magnetoelectric effect of Cr_2O_3 was first discovered by Astrov in 1960. It has a rather weak magnetoelectric coefficient $\simeq$ 4x10^{-12} s/m [18] at T=263 K. Most of the bulk single-phase magnetoelectric materials exhibit low values of the ME coefficient so that they are not usable for applications. Furthermore, the ME coefficient drops to zero above the phase transition temperature making them useless in applications with wide temperature range. The best value of ME effect for a single phase material α=36.7x10^{-12} s/m was recorded for $TbPO_4$ at T = 2K which is far away from room temperature [59]. The best room temperature ME effect was recorded for bulk Cr_2O_3, 2.67x10^{-12} s/m [60]. **Table (1.3)** summarizes some single phase magnetoelectric materials with their magnetic order and magnetoelectric coupling coefficient at certain measuring temperature.

Tab. 1.3: ME effect of some single-phase magnetoelectric materials.

Material	Magnetic order	Measuring Temperature (K)	α (ps/m)	Ref.
$TbPO_4$	Antiferromagnetic	2	36.7	[59]
Cr_2O_3	Antiferromagnetic	300	2.67	[60]
$Ga_xFe_{(2-x)}O_3$	Ferromagnetic	77	1.33	[61]
$TbMnO_3$	Antiferromagnetic	7	7	[45]

The single phase magnetoelectric materials show weak effect at low temperatures. Large effect at room temperature can be achieved in composites as shown in the following section.

1.6.5 Coupling via stress/strain at the interface

The most popular mechanisms of ME coupling in composites is the strain-mediated coupling. When an electric field is applied to a ferroelectric phase, a strain is produced due to the converse piezoelectric effect. If the ferroelectric and ferromagnetic phases are in direct contact, the resulting strain can be transferred to the magnetic phase through the interface causing a stress and a change of the magnetization via magnetostriction. The most interesting ME composites that have large coupling values via strain-mediated interaction are the laminate or layered structures as well as the epitaxially deposited nano-thin film structures where the contact between the ferroemagnetic and ferroelectric is direct, so that the strain can be easily transferred from one phase to the another due to the large interface. It was shown previously [62] for epitaxial $CoFe_2O_4$ films on $BaTiO_3$ single crystal that the magnetic domain configuration and the magnetic anisotropy can be altered via strain-mediated interaction between the ferromagnetic and ferroelectric phases. The majority of literature about stress-strain coupling at the interface related to the heterstructures consist of ferroelectric substrates such as, lead zirconium titanate) (PZT), lead magnesium niobate-lead titanate (PMN-PT), or $BaTiO_3$ (BTO) with magnetic films such as $CoFe_2O_4$ (CFO) and $NiFe_2O_4$ (NFO) grown on them forming of what is called (2-2) composite type [63–65].

1.6.6 Composite magnetoelectric materials

There are many composite materials that exhibit magnetoelectric effect. In composite magnetoelectics, a ME effect of more than one hundred times the values of single-phase materials can be achieved. This is the main driving force for studying composite magnetoelectric materials. In composites, the coupling

between piezoelectric and piezomagnetic phases is significantly influenced by mechanical constraints, e.g. for ferroelectric films, the ferroelectricity, the dielectric and piezoelectric properties are influenced by the lattice misfit between the film itself and the substrate as well as the compressive residual stress which cause more clamping effect and consequently weak magnetoelectric coupling interaction [66].

For composite materials, the magnetoelectric effect depends on the following important factors: (1) both phases piezoelectric and piezomagnetic phase should be non-reactive during processing and in the final product, (2) the magnetostrictive coefficient and the piezoelectric coefficient should be high for both phases in order to get a high α, and (3) high resistivity of the composite in order to pole the sample easily [21]. The coupling of ferroelectric materials and ferromagnetic materials has been intensively studied, for example with classical ferroelectrics $BaTiO_3$, $PbTiO_3$ or $(PbZr)TiO_3$/PZT), such as $CoFe_2O_4$-$BaTiO_3$ [67], $CoFe_2O_4$-$PbTiO_3$ [68] and $NiFe_2O_4$-PZT [25] have been successfully synthesized and studied. In fact, a high magnetoelectric coupling coefficient was also reported for the magnetostrictive/pizeofiber laminate of (FeBSiC alloy/PZT-5A) in the range of 22 V/cm·Oe which corresponds to the main unit value of $4x10^{-7}$ s/m [9]. However, they did not mention the value of permittity in their unit conversion. A nice study was also presented by Gao et al. [69] for both metglas with $Pb(Mg_{1/3}Nb_{2/3})O_3$-$PbTiO_3$ (PMN-PT) and metglas with $Pb(Zr,Ti)O_3$ (PZT) laminate composites. They reported direct magnetoelectric coupling coefficients for both materials as 45 V/(cm ·Oe) and 15 V/(cm·Oe) respectively.

1.7 Magnetostriction and electrostriction

1.7.1 Magnetostricition

The phenomenon *magnetostriction* was first discovered by James Joule in 1842 in nickel. It is a property which can be found in all magnetic materials. Mag-

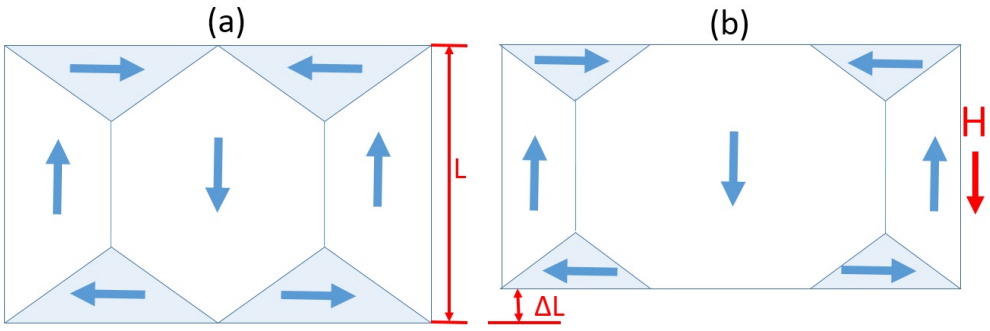

Fig. 1.13: Magnetic domain walls (a) before applying magnetic field (b) alignment of the domain walls and contraction after applying external field.

netostrictive materials change their shape when subjected to a magnetic field. Strong magnetostriction is related to domain reorientation. When applying a magnetic field, the magnetic moments begin to align their directions with respect to magnetic field direction. The rotation or the movement of magnetic domains cause elongation or contraction depending of the strength of the magnetic field, the direction of the magnetic field, magnetic properties of the materials and also the geometry of the sample. **Figure (1.13)** shows an example of contraction ΔL (e.g. for cobalt ferrite) when applying an external magnetic field.

Magnetostriction (λ) is defined as λ=ΔL/L . It can be different along different crystallographic directions. The value of λ can be positive or negative according to the response of the domains in the material. In experiments, the magnetostriction is usually measured when the magnetic field (H) is parallel to the sample plane and strain gauge as shown in **Figure (1.14)** or when the H field is perpendicular to sample plane and strain gauge. However, in all cases λ represent the strain value x_{ij} and the magnetostrictive coefficient N_{ijkl} is related to the strain x_{ij} and the square of magnetization $M_k M_l$ by the equation [36]:

$$x_{ij} = N_{ijkl} M_k M_l \tag{1.19}$$

For single crystal $CoFe_2O_4$, a large magnetostriction value was recorded

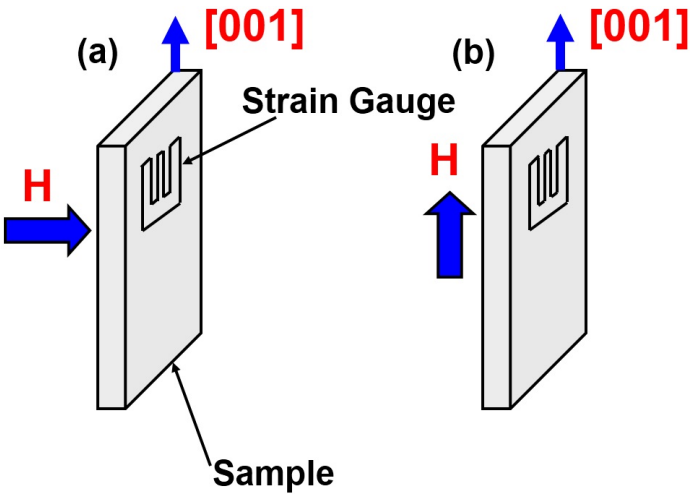

Fig. 1.14: Orientation of strain gauge and the magnetic field with respect to the measured sample, the measuring direction is along plane [001] and (a) H is perpendicular to the strain gauge and (b) H is parallel.

λ=-540·10^{-6} in the [100] direction as shown in **Figure (1.15)** [70]. The figure also shows the value of transverse and longitudinal magnetostriction for [100] and [110] planes. The transverse magnetostriction here is measured when the strain gauge is perpendicular to the applied magnetic field, and in longinutinal measurement both the elongation of the strain gauge and the applied magnetic field are in the same direction.

For polycrystalline $CoFe_2O_4$, it was found that the magnetostriction value can reach to 400 ppm [71]. **Table (1.4)** summarizes room temperature strain values for some materials. The low cost for synthesis and high magnetostriction make $CoFe_2O_4$ good candidate for sensors applications, e.g. stress and noncontact torques sensors [72–74].

Tab. 1.4: Saturation strain values for different polycrystalline magnetic materials.

Material	RT saturation strain (ppm)	Reference
Fe_3O_4	+60	[75]
$Tb_{0.3}Dy_{0.7}Fe_{1.9}$	1000-2000	[76]
$CoFe_2O_4$	-167	[77]
$Tb_{0.5}Zn_{0.5}$	+5500	[75]
$NiFe_2O_4$	-39	[78]
$DyFe_3$	+528	[78]
Y_2Co_{17}	+120	[78]

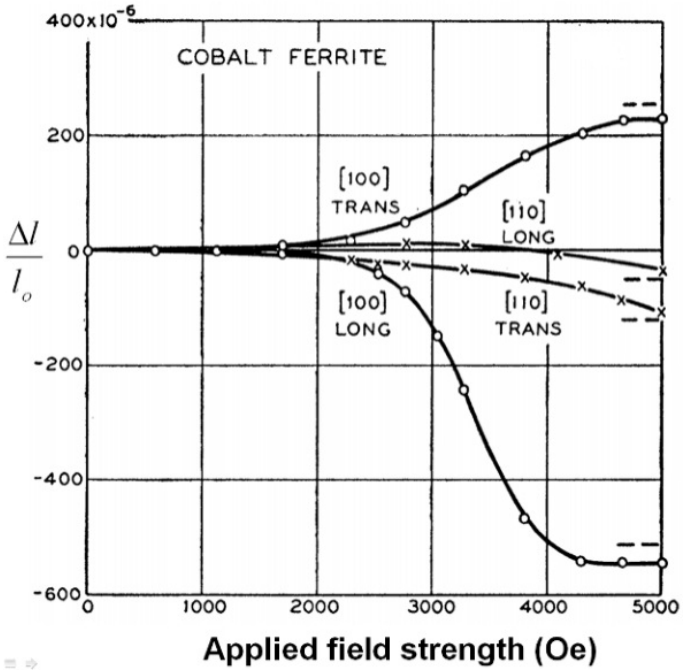

Fig. 1.15: Magnetostriction of single crystal cobalt iron oxide versus the applied field strength [70].

1.7.2 Electrostriction

Electrostriction is the change of the dimensions of a dielectric material by applying an electric field. Materials with large electrostriction are usually used in actuators such as $BaTiO_3$ [79]. Eelectrostriction is defined by the following equation [36]:

$$x_{ij} = Q_{ijkl} P_k P_l \tag{1.20}$$

The term Q_{ijkl} is a fourth rank electrostriction tensor, x_{ij} is the strain and $P_k P_l$ are the polarization vectors.

To illustrate the electrostriction phenomenon, **Figure (1.16)** shows a typical strain x-electric field E dependence for a ferroelectric material also termed butterfly loop. At point A the strain value is zero where no strain has occurred prior to the field application (origin state after sintering). When applying field, the strain increases through the curve AB. The point C is defined to be the

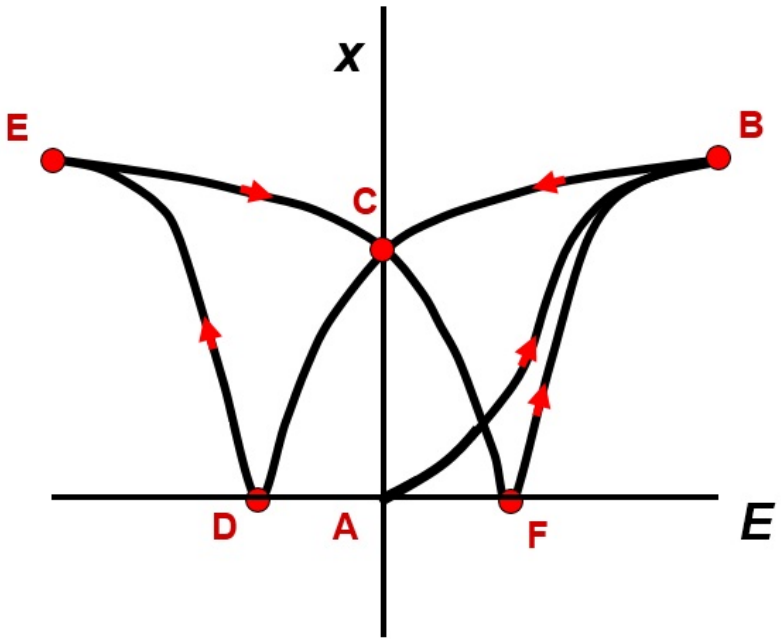

Fig. 1.16: Strain-electric field hysteresis loop for ferroelectrics.

remnant strain when removing the electric field back to zero. For negative fields through the curve CD, the strain decreases until reaching zero at point D. Point D corresponds to the coercive field or the depoling field where polarization is starting to reverse its direction. By increasing the negative field more and more it increases according to the curve DE until reaching the saturation strain value again at point E. **Table (1.5)** shows room temperature strain values for different materials.

Tab. 1.5: Room temperature strain values for different materials

Material	Maximum RT strain(%)	Ref.
Lead Lanthanum Zirconate-Titanate Ceramic (PLZT)	0.12	[80]
$BaTiO_3$ single crystal	0.8	[81]
poly(vinylidene uoride-triuoroethylene) P(VDF-TrFE)	5	[82]
$Pb(Mg_{1/3}Nb_{2/3})O_3$(PMN)	0.24	[83]

Due to the effective electrostriction and magnetostriction properties, in the following two sections I will describe the structure and the properties of both barium titanate and cobalt iron oxide and why I chose these two substances to synthesize the composite.

1.7.3 Product properties

The magnetoelectric coupling is the product property of magnetostrictive effect in the magnetic phase and the piezoelectric effect in the piezoelectric phase as shown in these equations [84]:

$$ME_H = \frac{magnetic}{mechanical} \times \frac{mechanical}{electrical} \tag{1.21}$$

$$ME_E = \frac{electrical}{mechanical} \times \frac{mechanical}{magnetic} \tag{1.22}$$

Where the term ME_H is the magnetoelectric effect in terms of producing magnetization by applying electric field which is called the converse effect, and the term ME_E is the direct effect by producing electric polarization according to a subjected magnetic field.

Becuase the coupling orginates from the stress strain relation, the shape of the curve e.g. $M_{ME}(H)$ is determined by the product of the piezoelectric component times the piezomagnetic one. A modified meaningful version for **Equation (1.22)** was introduced by Lupascu et al. [55]. They introduced the coupling coefficient by the following equation:

$$\alpha_{ij}(H) = \frac{\mu_o dM_i(H)}{dE_j} \tag{1.23}$$

The equation above can be also written as:

$$\alpha_{ij}(H) = \frac{\mu_o dM_i(H)}{d\sigma_{mn}} \cdot \frac{d\sigma_{mn}}{d\epsilon_{kl}} \cdot \frac{d\epsilon_{kl}}{dE_j} = q_{imn} \cdot c^*_{mnkl} \cdot d_{jkl} \tag{1.24}$$

where q_{imn}, c^*_{mnkl} and d_{jkl} are the piezomagnetic coefficient, an effective stiffness of the composite, and the piezoelectric coefficient, respectively. In this equation the magnetoelectric response tracks the H_{dc} dependence of the magnetostrictive strain coefficient:

$$q_{ikl}(H) = \frac{d\lambda_{kl}(H)}{dH_i} = \frac{\mu_o dM_i(H)}{d\sigma_{kl}} \tag{1.25}$$

If we consider Heckmann diagram in **Figure (1.11)**, the effect of the dc magnetic field on the ME effect and by looking at **Equation (1.24)**, we can notify that the value of $\mu_o dM_i(H)/d\sigma_{mn}$ is equal to the piezomagnetic coefficient $q_{ikl}(H)$ which is equal to $d\lambda_{kl}(H)/dH_i$ where λ_{ij} is the magnetostrictive strain. "At the individual interfaces between the magnetic and piezoelectric phases, λ_{ij} is identical to ϵ_{ij} in the piezoelectric phases. But most of the material is not at the interface but rather in a volume around it experiencing an effective stress. The overall response is thus given by an effective stiffness c_{mnkl}=$d\sigma_{mn}/d\epsilon_{kl}$ of the microstructure or device, respectively, transferring the interface constraint into the material volume [55]".

For explaining the behavior of the magnetoelectric coupling coefficient curve, **Figure (1.17.a,b)** shows both the experimental strain curve for polycrystalline cobalt iron oxide and the magnetoelectric effect curve at various dc magnetic field. It is obvious that the magnetic field dependence of the magnetoelectric effect must track the tangents of the polycrystalline magnetostriction. Referring to **Equation (1.24)**, and in case of converse magnetoelectric effect, the curve $\alpha_{ij}(H)$ tracks the curve of (q_{ijk}=$d\lambda_{jk}/dH_i$). In case of direct magnetolelectric effect **(Figure 1.17.c,d)**, the electric field dependence of the $\alpha_{ij}(E)$ curve tracks the curve of strain-electric field (d_{ijk}=dx_{jk}/dE_i) for polycrystalline barium titanate.

1.8 Barium titanate ($BaTiO_3$)

Barium titanate ($BaTiO_3$) is the best known ferroelectric material. It is often used in capacitors and actuators. The first publication of the ferroelectric properties of $BaTiO_3$ was published on 1946 by von Hippel et al. [85]. $BaTiO_3$ has the cubic perovskite and stays tetragonal at room temperature as shown in **Figure (1.18)**. The material has three phase transitions, it is cubic above

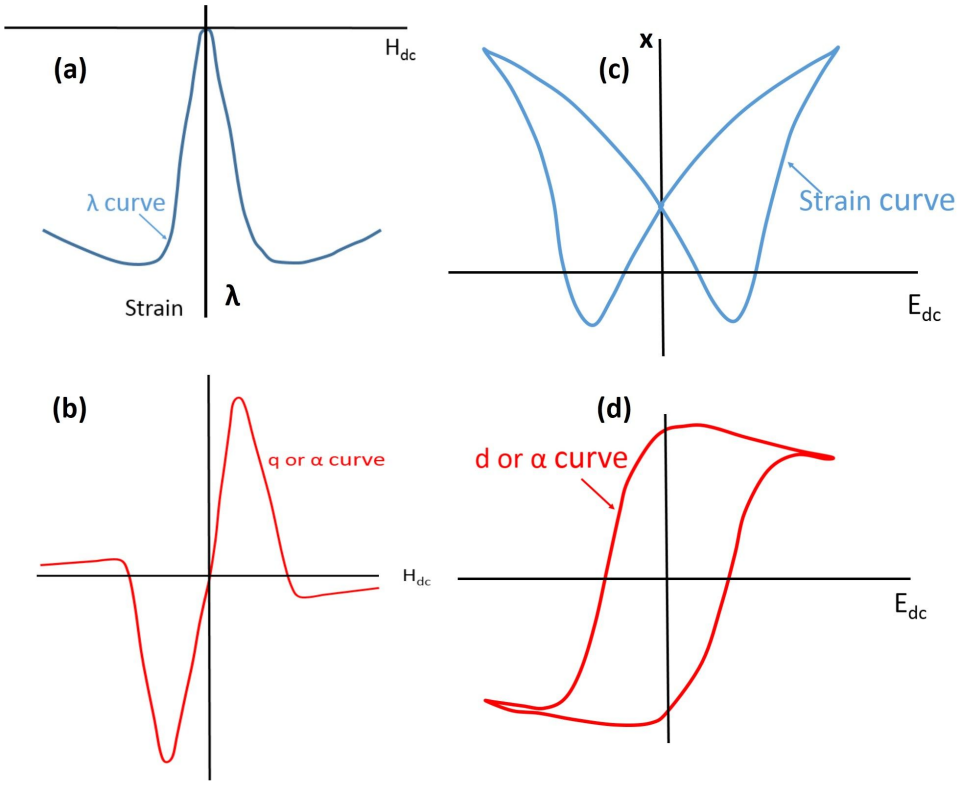

Fig. 1.17: (a) Strain-magnetic field curve for polycrystalline cobalt iron oxide and (b) the corresponding magnetoelectric coupling curve dependence of dc magnetic field (c) strain-electric field curve of polycrystalline barium titanate and (d) the corresponding magnetoelectric coupling curve dependence of dc electric field.

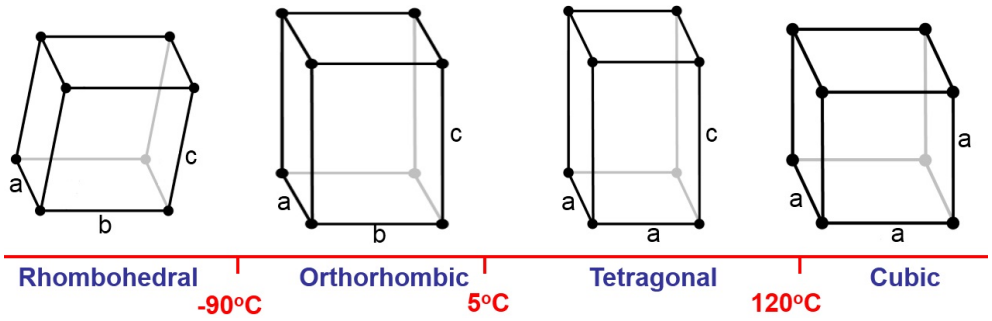

Fig. 1.18: Sequence of phase transitions for $BaTiO_3$ unit cell [86].

120°, tetragonal between 120° and 5°, orthorhombic between 5C° and -90C°, and rhombohedral at lower temperatures [33, 86].

Figure (1.19.a) shows the unit cell of $BaTiO_3$ in the paraelectric phase. The Ba^{+2} ions are located in the corners, and Ti^{+4} is placed in the center of the cube. The O^{-2} ions are face centered on the six faces of the cube. In the cubic phase $BaTiO_3$ has no spontaneous polarization but can be polarized by an electric field. The direction of the polarization is the same as the applied field. It returns to zero after removing the field. For the tetragonal phase, Ti^{+4} moves in [001] direction (see **Figure (1.19.b)**). This yields a small dipole moment inside the unit cell. The reason of that the sum of Ti^{+4} and O^{-2} radii is about 0.196 nm, and the distance between the two ions is equal to 0.2005 nm so that there is free space 0.0045 nm for Ti^{+4} to move freely. The displacement of the Ti^{+4} can be along six possible [001] directions. The tetragonal phase has a unit cell parameter of a =b= 3.992 Å, and c = 4.036 Å with tetragonality value of c/a $\simeq$ 1.011 [33].

1.9 Cobalt iron oxide ($CoFe_2O_4$)

$CoFe_2O_4$ is one of the most important materials that is used in magnetic recording material. It belongs to the spinel family with the general chemical formula $(Co_{1-x}Fe_x)[\ Co_xFe_{2-x}]O_4$ where the round bracket indicates the tetrahedral A-sites and square brackets indicates octahedral B sites. If x=1, the structure is called *inverse spinel* and if x=0, the structure is *normal spinel*,

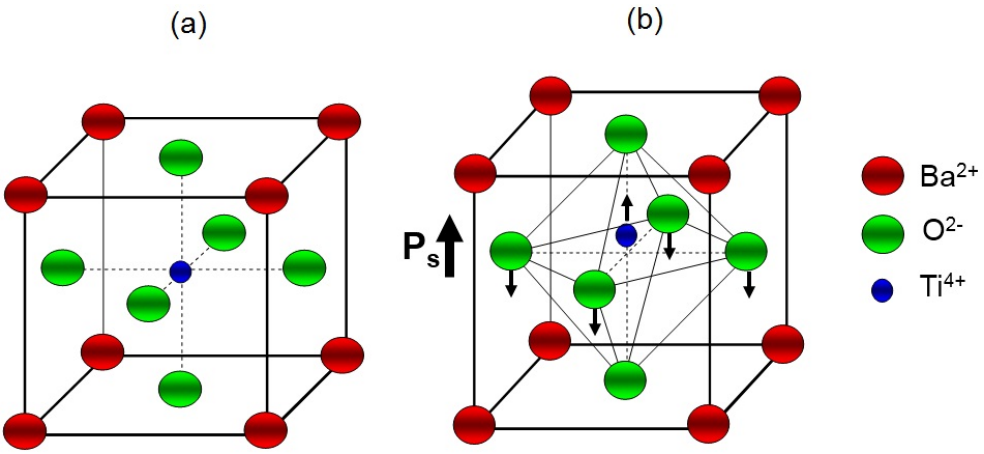

Fig. 1.19: perovskite structure of $BaTiO_3$ (a) cubic (b) tetragonal.

otherwise the structure is mixed spinel [87]. The difference between inverse and normal spinel structures is shown in **Figure (1.20)**. $CoFe_2O_4$ has an inverse spinel structure where the Co^{+2} occupy one half of the octahedral coordination sites and Fe^{+3} cations occupy the other half of the octahedral sites, as well as tetrahedral sites see **Figure (1.20)**. $CoFe_2O_4$ also was reported to be not fully inverse spinel and the degree of inversion depends on the heat treatment [88].

For the inverse spinel structure, the magnetic moments of the atoms located on the tetrahedral (A) sites are antiparallel those on the octahedral (B) sites so that $CoFe_2O_4$ has a collinear ferrimagnetic structure. In case of cobalt ferrite, the general chemical formula for the inverse spinel structure can be written as $(Fe^{+3})O[Co^{+2}Fe^{+2}]O_3$ so that the value of magnetic moments will be expressed by the equation:

$$M = [\mu_B(Fe^{+3}) + \mu_B(Co^{+2}) - \mu_B(Fe^{+3})] = (5 + 3 - 5)\mu_B = 3\mu_B \quad (1.26)$$

where μ_B is the Bohr magneton. However, the measured magnetic moment per unit cell is about $3.7\mu_B$. The reason for having different values between experimental and theoretical values is that the iron distribution on its sites is not perfect. The orbital magnetic contribution is not zero as assumed. Also

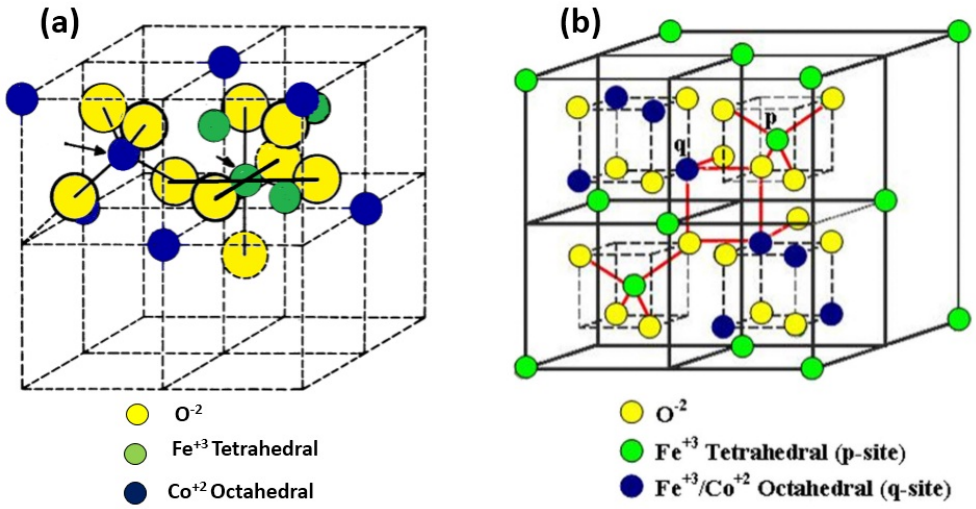

Fig. 1.20: (a) Normal spinel structure showing A-sites and B-Sites distribution [Reproduced from [89] (b) inverse spinel structure showing A-sites and B-sites distribution [90].

the direction of spins is not antiparallel but also canted [91]. Sometimes in experiment it is difficult to know whether $CoFe_2O_4$ is a fully or partially inverse spinel. In fact, Mössbauer spectroscopy is a way to determine the degree of inversion which will be described in detail in the next chapter. $CoFe_2O_4$ is one of the most used magnetic materials, because of the high coercivity about (430 kA/m) and moderate magnetization about (84 Am^2/kg) , good chemical stability, good hardness, wear resistance, high cubic magnetocrystalline anisotropy, high electromagnetic and photomagnetic performance [87, 92, 93]. $CoFe_2O_4$ also has a high Curie temperature of about 520^oC and large magnetostriction coefficient values. All of these properties make $CoFe_2O_4$ a candidate for a number of applications such as: high density recording disks, magnetic resonance imaging, magneto optic devices, actuators, and sensors. The magnetic properties of cobalt ferrite and its applicability depend on grain size, synthesis method, chemical stoichmetry etc. [93–95]. The particle size of the $CoFe_2O_4$ plays an important role. Below a critical size; usually around (1-10 nm), $CoFe_2O_4$ exhibits superparamagentic behavior [96].

1.10 Binary $CoFe_2O_4/BaTiO_3$ composite

Composites containing $BaTiO_3$ and $CoFe_2O_4$ have received much attention, because of the piezoelectric and piezomagnetic properties of both materials. Due to the spinodal decomposition of the barium titanate-cobalt ferrite binary system it is possible to obtain pure phases of both constituents in the composite even after high temperature treatment [97]. Spinodal decomposition -which is phase separation- was first discussed by John Cahn in 1961 [98]. When a homogeneous mixture of a two phase system is quickly cooled, two finely separated phases appear. The first attempt to synthesize $BaTiO_3$-$CoFe_2O_4$ composite ceramics was related to Van Suchetelen in 1972 [84] and the first ME effect was measured for the $CoFe_2O_4$-$BaTiO_3$ system by Van Run [99].

Particulate composites of both materials have been synthesized by mixing the $BaTiO_3$ and $CoFe_2O_4$ powders, pressing them into pellets and subsequent sintering. The distribution of ferrite phase in the $BaTiO_3$ matrix is usually non-homogeneous. The cobalt ferrite phase forms percolated clusters and therefore it is difficult to pole these samples due to large conductivity of cobalt ferrite. The achieved values of magnetoelectric coefficients were in the range of 0.04-16 mV/cm·Oe [100–103]. Sol-gel methods have been also used for synthesizing particulate composites [100, 104, 105] and the value of the ME coefficient reached about 8.5 mV/cm·Oe. Nie et al. (2009) [106] proposed a simple and environmental friendly synthesis method to prepare $CoFe_2O_4/BaTiO_3$ bulk composite by the molten-salt route. They measured a ME coefficient for the sample using lock-in technique and the longitudinal method, where the dc magnetic field, the ac magnetic field and poling of the sample are in the same direction. They found coupling value of 17.04 mV/(cm·Oe). For ensuring better contact between the two phases, to increase the insulating properties and to enlarge the interface area, the idea of a core shell structure was proposed [107] where particles of $CoFe_2O_4$ should be completely separated by shells of

$BaTiO_3$. However, the core-shell structure was difficult to preserve during higher temperature ceramic processing. This explains relatively low values of ME coupling which reached a maximum of 1.5 mV/(cm·Oe) for a composite containing 50 percent of $BaTiO_3$ and 50 percent of $CoFe_2O_4$ [105]. Synthesis of composites with core shell structure was also reported by Duong et al. [101]. The value of the ME coupling was reported to be 3.5 mV/(cm·Oe). However, the authors did not show any evidence of the core shell structure neither for powders nor for the ceramics. $CoFe_2O_4$-$BaTiO_3$ core shell structures were successfully synthesized by Corral-Flores et al. [108], but the values of ME coupling were not measured for these nanopowders because of the high porosity and difficulties to make dense ceramic samples from such nanopowders. The converse ME coupling $2.2x10^{-11}$ s/m was measured for a ceramic core shell composite containing 50 percent of $BaTiO_3$ prepared using the sol-gel method [104]. These values are still lower than the theoretical value for different compositions of $BaTiO_3$ and $CoFe_2O_4$ $25x10^{-10}$ s/m predicted by Nan [109]. Raidongia et al. [110] have synthesized $CoFe_2O_4$-$BaTiO_3$ core shell nanoparticles and nanotubes using the sol gel method. They measured the magnetocapacitance (change of the dielectric permittivity by magnetic field) for these structures. The core shell nanoparticles exhibited 1.7 percent change in magnetocapacitance at T=134 K and H=1 T while the core shell nanotubes exhibited 4.5 percent change at T=310 K and H=2 T.

Besides particulate composite, (2-2) layer structures were sintered. In this case ferromagnetic layers are in direct contact with the ferroelectric layers and the ferromagnetic layers here are completely insulated from each other. Pulsed laser deposition (PLD) has been commonly used for making thin films, layers and heterostructures, so $CoFe_2O_4$-$BaTiO_3$ heterostructures were grown on the (001) $SrTiO_3$ using PLD [63]. The values of ME coupling measured were 104 mV/(cm·O and 66 mV/(cm·Oe) for the out of plane and in plane ME voltage coefficient respectively. These values are larger than those for the particulate

composite but still far away from the theoretical value 800 mV/(cm·Oe) [66] for (2-2) composites. The (1-3) $CoFe_2O_4$-$BaTiO_3$ composite with $CoFe_2O_4$ nanorods embedded in $BaTiO_3$ matrix were successfully synthesized and studied [111]. The films were deposited and grown using PLD on (001) $SrTiO_3$ single crystal. The authors estimated the ME effect for such films using SPM (scanning probe microscopy) by subtracting the phase of MFM (magnetic force microsocpy) before and after applying electric field. They estimated the value to be in the range of 1.2 V/cm·Oe. This value is larger than the theory value for (2-2) connectivity composite of $CoFe_2O_4$-$BaTiO_3$. Moreover, theoretical comparison between coupling values of (1-3) and (2-2) for the same composite showed that the (1-3) composite exhibit larger coupling values [66].

1.11 Role of connectivity

Essentially, magnetoelectric properties of the composite depend on the type of connectivity between the phases. For example 3-0 connectivity represents particulate composite with one phase dispersed in the other, 2-2 represents the layered structure, and in 1-3 one of the two phases is in the shape of pillars. In case of magnetoelectric composite with piezoelectric and piezomagnetic phases the first number indicates the connectivity type for the piezomagnetic materials and the second one for the piezoelectric. The most important connectivity types are shown in **Figure (1.21)**. To manufacture these ceramic types, different methods are used such as extrusion tape casting, dicing, injection and hot pressing [112]. To ensure better distribution of $CoFe_2O_4$ areas in $BaTiO_3$ matrix, the (0-3) connectivity type is chosen and used. In this work, it is not easy to form this type of connectivity especially by conventional sintering methods.

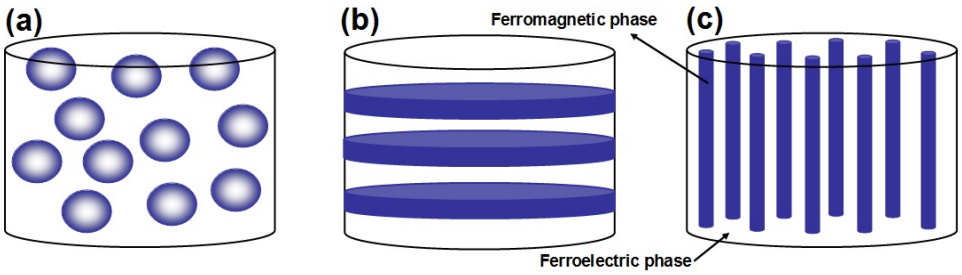

Fig. 1.21: Illustration of Piezomagnetic/Piezoelectric common connectivity mode in composites showing (a) 0-3 particulate composite (b) 2-2 layer or laminate structure (3) 1-3 rod structure .

1.12 Core shell and (0-3) composites

In 0-3 magnetoelectric composites, it is important to have a well distribution of ferromagnetic phase in the ferroelectric matrix. The better distribution of the ferromagnetic phase in the matrix ensures better contact between the two phases and consequently may result in better magnetoelectric effect. Therfore it is attractive to synthesize nanoscale composite powders with ferromagnetic cores surrounded by ferroelectric shells forming piezomagnetic-piezoelectric core shell structures. However, It is important to convert this nanoscale composite powder to the ceramics keeping the core shell structure. The benefits of that can be summarized as: better isolated magnetic particles result in a relatively high resistivity of the samples and improvement of the poling process, see **Figure (1.22)**. In this case, we will also have a large interface area between the two phases. The first attempt to sinter core-shell structure of $CoFe_2O_4$ and $BaTiO_3$ was reported by Correl-Flores et al. in 2006 [107] where they investigated the ME effect for different compositions of ceramic samples. They found that the core-shell powder structure was lost after sintering at 1200°C due to diffusion and agglomeration of magnetic particles and the composite contained individual micro regions of agglomerated $CoFe_2O_4$ grains surrounded by $BaTiO_3$ matrix.

Islam et al. (2008) [113] synthesized a core shell structure composite of Pb(Zr, Ti)O_3 (PZT) and $NiFe_2O_4$ (NFO) using a conventional chemical syn-

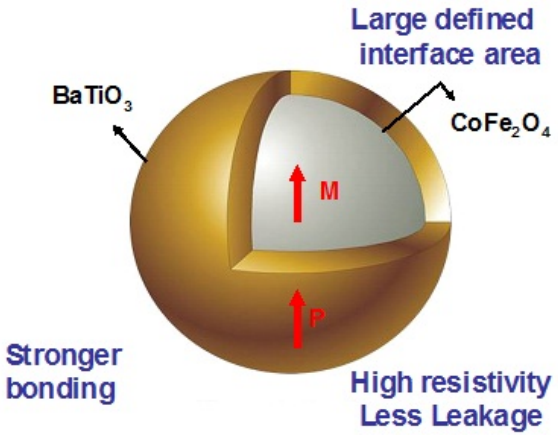

Fig. 1.22: Schematic drawing showing the proposed $CoFe_2O_4$-$BTiO_3$ core shell particle structure.

thesis technique. It was not clear, whether the core shell structure persisted in the ceramic form. However, transmission electron microscopy (TEM) showed areas of PZT grains surrounded by nickel ferrite. The measured longitudinal ME coefficient was 195 mV/(cm·Oe) at 454 Oe. This value is about 130 times higher than that reported for $CoFe_2O_4$-$BaTiO_3$ core shell structures.

1.13 Scientific challenge

Magnetoelectric (ME) materials are promising for a number of applications including novel memory elements and high sensitivity magnetic field detectors. However, a rather weak effect makes single phases materials not beneficial for applications. Contrarily, composite multiferroics exhibit much larger ME effect. For this reason more efforts should be placed in order to design composites with improved ME coupling at temperatures close to room temperature. Nowadays, much effort is directed to synthesize scalable materials with high coupling values. The main challenges here are the synthesizing procedures, which are affected by different factors such as temperature, time, chemical composition and others. Other challenges include the measuring methods and the measuring parameters. For most systems these parameters are not well defined up to now, for example the relation between the converse and the di-

rect ME effect measurement, the frequency dependence of the ME coupling and the interrelationship between the macroscopic materials properties and the magnetoelectric effect.

1.14 Motivation

It is important these days to investigate new composites with new structures and new properties and with high mangetoelectric effect in order to fabricate new instrumentation used in applications. The nanotechnology brought these days new tools and scientific equipment to the industry, especially in fields of sensors, memories, and electrical circuits. Less power consumption, higher sensitivity and faster processing times are expected from the nanotechnology. In sensors for example, the design of nanomaterial will allow to go through molecular levels which may improve the sensitivity. The design of these sensors is based on multiferroic materials. Several work groups have studied multiferroics single and composite materials with ferroelectric/ferromagnetic phases. Core shell composite nanoparticles are still an issue because of many factors. First, the difficulty in chemical synthesis such as the particles morphology control, agglomeration of the magnetic particles, and reaction temperature control, second, the difficulty in measuring techniques for such core shell nanoparticles, third, the certainty that all of the core nanoparticles are covered by shells, and finally the persistence of the structure at higher temperatures. For composites in ceramic form, the effect of microstructure and constituents on the magnetoelectric coupling properties is also rarely reported. Regarding the magneto electric measuring techniques, the converse magnetoelectric effect is also rarely reported as well as the relation between the direct and the converse effect. Despite of the development of new synthesizing procedures for magnetoelectric composites, composites containing $CoFe_2O_4$ and $BaTiO_3$ are still of high interest due to the high magnetostriction and electrostriction properties previously discussed. These properties are the key factor for the

strain-mediated magnetoelectric effect. The variety of experimental magnetoelectric coupling values are still far away from the theoretical modeling values which motivates this research. Several issues should be explained here such as the relation between the magnetoelectric effect and the dielectric properties, the effect of resistivity and microstructure on the coupling and the behaviour of magnetoelectric coupling itself. For better properties in electroceramic the percolation should be also avoided especially in the (0-3) composite which is the main challenge of this project [2]. The structure of core shell is the best choice to ensure the best larger area between the two phases. One of the project challenges is keeping this core shell structure in the ceramic form. It is proposed that the bigger sizes of shells surrounded magnetic particles are expected to have higher resistivity and better poling.

1.15 Research goals

The goal of the project is to establish a well designed material that is able to generate a representative experimental data-set for the constitutive behavior of bulk multiferroic composites. This can only be achieved via reliable material synthesis. The starting choice of materials is the ferroelectric $BaTiO_3$ and the ferrimagnetic $CoFe_2O_4$. These two materials have large piezoelectric and piezomagnetic properties as described before. The main objectives of the project are:

a. obtaining a nanoscale (0-3) $CoFe_2O_4$-$BaTiO_3$ composite with large magnetoelectric coupling.

b. revealing the interrelationship between ME response and composition and microstructure of studied composites.

to reach these goals I:

- develop a route to synthesis composite $CoFe_2O_4/BaTiO_3$ nanopowders with core shell structure

- develop routes to synthesize dense ceramic with high resistivity
- develop a setup to measure the magnetoelectric effect, and
- perform a comprehensive characterization of the ME constitutive behavior of different samples compositions.

2. REVIEW OF SCIENTIFIC INSTRUMENTS AND MEASURING TECHNIQUES

In this chapter, I introduce details about the instruments that were used in this project in order to analyze the structural, electrical, magnetic and magnetoelectric properties of pure cobalt ferrite barium, cobalt ferrite-titanate nanopowder and cobalt ferrite-titanate ceramic composites.

2.1 XRD (x-ray diffraction)

The x-ray here is generated by colliding high speed electrons on metal target like copper. This metal is placed between cathode and anode. An accelerating voltage is applied between them in order to generate the electrons. The idea of x-ray diffraction is the use of x-rays (which have a high energy and short wavelengths) to detect materials structure. The x-ray waves are subjected to the object and then encounter obstacles that diffract them in different patterns and directions.

In non-crystalline (amorphous) materials the diffractions of the rays are random so that no phases will be detected. In case of crystalline material the atoms diffract the waves in certain pattern, so that any repeating or arrangement of atoms diffract for sure a specified pattern. The x-ray waves can be subjected to the sample in a certain angle (θ) as illustrated in **Figure (2.1.a)**. The relation between the incident wave length, the incident angle θ and the interplanar spacing d is expressed using Bragg's law:

$$n\lambda = 2dsin\theta \tag{2.1}$$

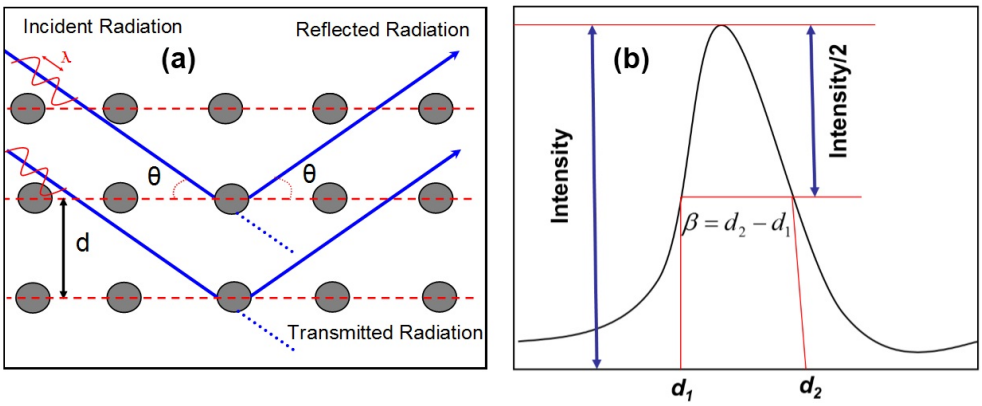

Fig. 2.1: (a) Diffraction of x-rays by planes of atoms (b) part of x-ray spectrum showing Scherrer equation parameters.

where n here is an integer, λ is the wave length and d is the interplanar spacing

The diffraction patterns for crystalline materials show many distinct peaks. These peaks correspond to different interplanar spacings d. The relationship between the interplanar spacing and the lattice parameters can be geometrically determined depending on the crystal structure, e.g. for the cubic structure the distance between two adjacent and parallel planes of atoms can be determined by the following equation:

$$d_{hkl} = \frac{a}{\sqrt{h^2 + k^2 + l^2}} \tag{2.2}$$

Where a is the lattice parameter and (hkl) are the Miller indices. The same thing can be done for the tetragonal structure, the interplanar space is related to the lattices parameters by the following equation:

$$d_{hkl} = \frac{1}{\sqrt{\frac{h^2+k^2}{a^2} + \frac{l^2}{c^2}}} \tag{2.3}$$

where c here is the lattice parameter representing the height.

Using x-ray diffraction spectrum one can estimate the particle size (D) by the Scherrer equation:

$$D = k\lambda/\beta_l cos\theta \tag{2.4}$$

where

k= the shape factor

β_l= is the line broadening at half the maximum intensity (FWHM) in radians

The explanation of using Scherrer equation is illustrated in **Figure (2.1.b)**. This equation is limited to nano-scale particles. It is not applicable to particles larger than 0.1μm [114]. The x-ray diffraction can also be used for measuring residual stresses, strains, and phase contents. In this project, I used x-ray diffraction for structural analysis for both powder and ceramic samples. I utilized Siemens D-5000 diffractometer (Cu-Kα radiation with λ= 1.54056 Å) to detect the crystal phases in the sample with angles ranging between $20° \leq 2\theta \leq 80°$ with 0.01° step size and 1s as time constant. The powders were inserted into the circular cavity of a plastic sample holder and then slightly pressed in order to make the surface of the sample flat and in the same plane as the sample holder surface. For samples in ceramic form, they were placed in the sample holder using a gum. The top surface of the sample was at the same level as the sample holder surface.

2.2 TGA/DTA Thermogravimetric Analysis/Differential Thermal Analysis

To investigate the thermal properties of my materials, I applied thermogravimetric analysis/differential thermal analysis (TGA/DTA). DTA provides information about reactions and phase changes during heating or cooling cycles. This method is done by detecting the temperature difference between the sample and a known reference. When heat is supplied to the system, both the reference and the sample have the same conditions before heating starts. DTA detects the release or the absorption of heat, and gives information by

plotting the temperature for both the sample and the reference versus the time. In this case, we can estimate the heat of crystallization and the transition temperature. In TGA, the heat is utilized in order to make reactions and physical changes in the materials. This can be done by recording the changes of material mass versus different temperature range so that phase transitions, decomposition, sublimation and dehydration can be observed. A Mettler Toledo (TGA/DSC 1 star) device was used here.

2.3 SEM (scanning electron microscopy)

The morphology of the samples surfaces was studied by SEM. The principle of SEM is that a beam of electron is subjected to the surface of the specimen. The reflected beam is collected and displayed using a cathode ray tube. This image represents surface textures and features characterizing the sample surface. Using SEM, the grain arrangement, size and shape can be easily seen. The main parts of SEM instrument as shown in **Figure (2.2)** include: electron gun, detectors (secondary and backscattered electron detectors), magnetic coils, display, stage and control system. SEM is a non-destructive test which can be used for different kinds of materials and even in biology. The backscattered electron images in SEM result from different atomic number of the material elements and their distribution. Energy dispersive spectroscopy (EDS) is combined with SEM to identify these elements and their proportions. (Quanta 400 FEG) SEM was used with cooperation of Dipl.-Ing Yanling Gao to study the morphology for different samples. The powder and the ceramic samples were analyzed by SEM. All samples were covered by a thin layer (3-10 nm) of gold in order to reduce sample charging and improve the secondary electron emission. Ceramic samples were mirror-like polished, thermally etched at 100 degrees lower than the sintering temperature and then sputtered before scanned by SEM. Thermal etching is important here in order to reveal the grains.

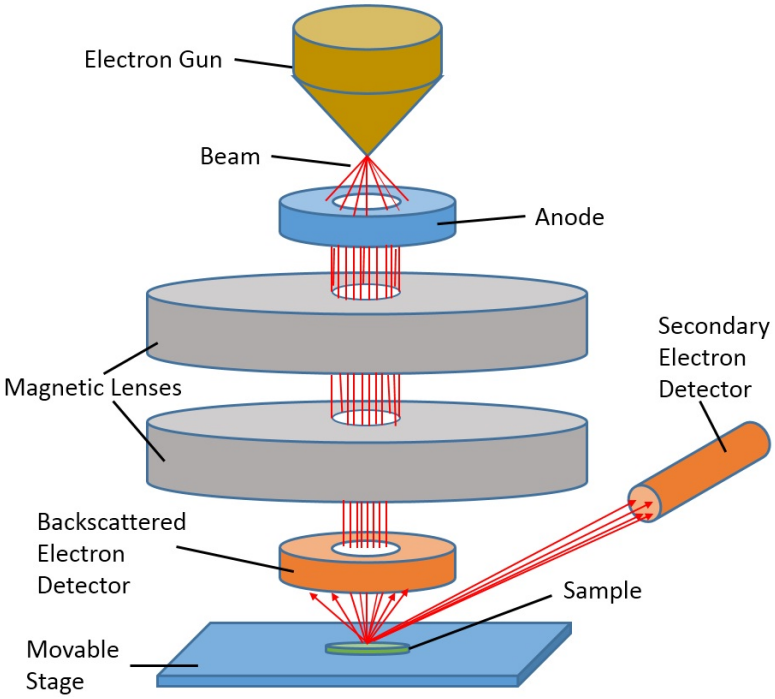

Fig. 2.2: Schematic diagram of the scanning electron microscopy

2.4 TEM (transmission electron microscopy)

TEM is based on the transmitted electrons. The electrons pass through the samples and then generate an image. In TEM the electrons can scattered and transmitted. The transmitted electrons pass through an objective lens and are then projected onto a scintillating material which can then be recorded photographically. The tested samples should be very thin in order to allow more transmission of the electrons. TEM can better magnify than SEM and the resolution is better and can reach the atomic resolution level. TEM requires good preparation of the samples especially the samples which are in ceramic form. A transmission electron microscope (TECNAI F20) with high resolution capability was used by Dr. Anna Elsukova to identify the crystal structure for a variety of samples. For sample preparation for the samples in powder form, a small amount of solvent (ethanol) was added to the powder and an ultrasonic machine was used to disperse the particles. Then a small drop of the suspension was added to the TEM grid sample holder and transferred to

the chamber of the microscope.

2.5 AFM (Atomic force microscopy)

AFM is a versatile technique for surface investigation at the nano-scale. The principle of atomic force microscopy is to measure the force between the atoms surfaces and the tip of the cantilever which moves over the sample surface. The cantilever tip which is usually in nanometer range radius touches the measured surface exactly. Any forces such as attractive, repulsive and friction forces generate a deflection of the cantilever. Vertical and horizontal deflections of the cantilever can be measured. The interaction between the surface and the tip depends on the tested material, the type of the tip, and the distance between the sample surface and the tip, see **Figure (2.3)**. AFMs uses a reflected laser beam on the back of the cantilever. Deflection of the cantilever causes angular deflection of the laser beam which strikes a photo-detector consisting of four side photo-diodes, the differences between the four photo-diode signals indicate the position of the laser spot on the detector and thus the deflection of the cantilever. Piezoresponse force microscopy (PFM) is a special modification of atomic force microscopy. The tip (see **Figure (2.3)**) acts as a movable electrode where an AC voltage is applied to the tip and a lock-in amplifier is used to measure the vertical surface strain as a phase and a magnitude due to the piezoelectric effect. The direction of the polarization of the sample and the direction of the applied field determine the direction of the elongation or the contraction of a certain detection point. PFM is also a tool for studying *domain switching*. If the applied voltage is higher than the coercive voltage, the spontaneous polarization can be switched and this will give information about the local coercive field for the domain, the nucleation of new domains and the velocity of the domain walls movement. If a triangular voltage is applied, a *local domain switching loop* can also be measured by PFM.

MFM (magnetic force microscopy) measures in a non-contact mode. It is

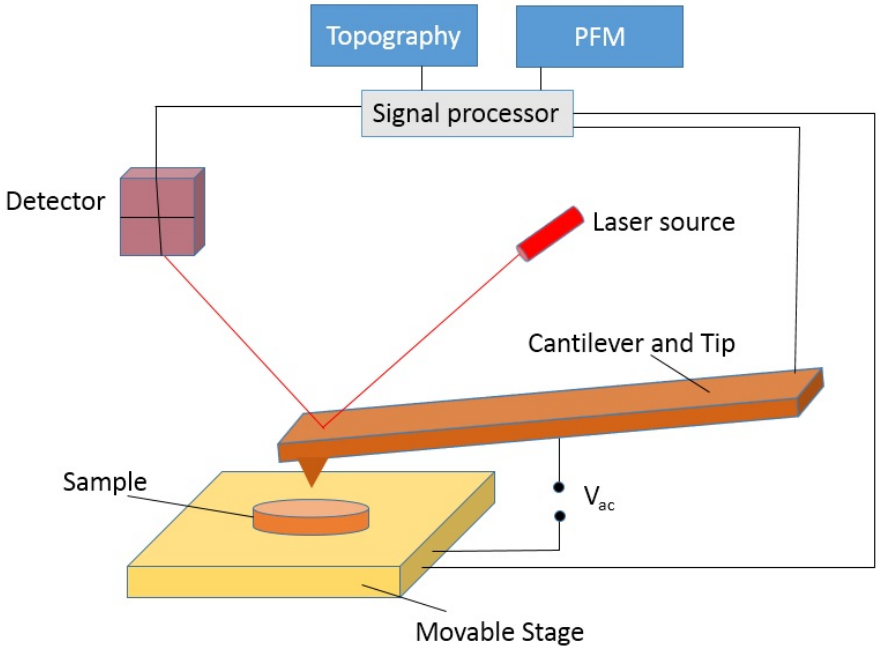

Fig. 2.3: Basic principle of AFM (atomic force microscopy)

used to detect magnetic regions on the material surface using a ferromagnetic tip. The first experimental setup for mapping magnetic fields by force microscopy was described Martin et al. [115]. The static forces caused by the interaction between the tip of the cantilever and the magnetic surface can be scanned and detected. MFM can also be used for detecting magnetic regions in pure magnetic materials or magnetoelectric composites, in magnetic recording studies [116] magnetoelectric effect [111] and even to find magnetic phase transitions [117]. For mirror-like polished ceramic samples, MFP 3D (Asylum Research) was used in this dissertation with cooperation of M. Sc Harsh Trivedi to detect the magnetic and the ferroelectric phases using MFM and PFM techniques respectively.

2.6 Sawyer Tower circuit for ferroelectric hysteresis loop measurements

Different methods are used to measure the polarization hysteresis loops such as pulse switching, Sawyer-Tower circuit, and constant current [34, 118, 119].

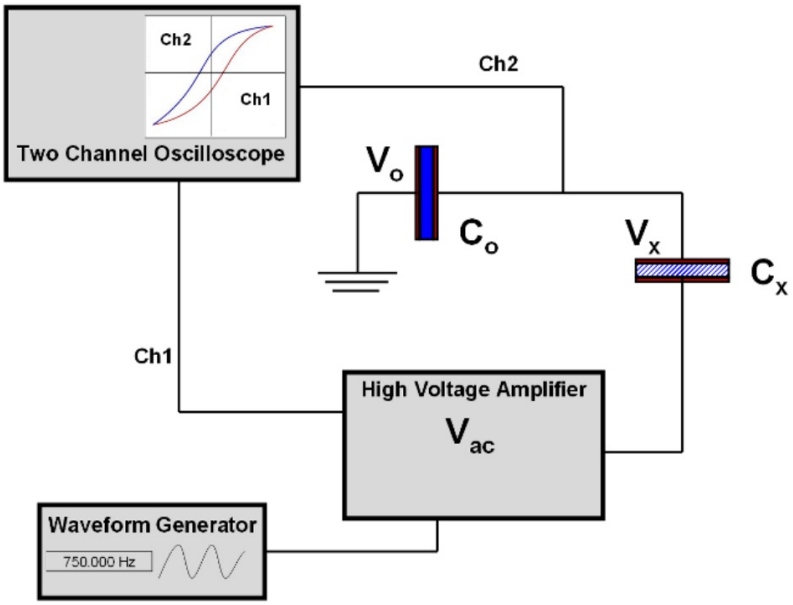

Fig. 2.4: Sawyer-Tower circuit setup for measuring polarization.

The commonly used method is the Sawyer-Tower circuit which is illustrated by **Figure (2.4)**. Both the measured sample with capacitance (C_x) and a known capacitor (C_o) with higher capacitance value are connected together in series. An ac voltage is applied to the circuit using high a voltage amplifier. Both the applied ac voltage and the voltage across the known capacitor are measured using an oscilloscope. Because the charge is equal in both capacitors, the charge of the sample can be calculated from voltage and capacitance of the known capacitor and the polarization is equal to P=(V_o·C_o)/A where, V_o is the measured voltage across the capacitor, and A is the sample electrode area. The P-E loop is the plot of the applied electric field versus the polarization. This measurement is more accurate when the sample leakage current is small. The ceramic samples were coated by two parallel electrodes using (silver paste) and tested their P-E loops in silicon oil. The ac applied voltage was in triangular form at different frequencies.

2.7 Dielectric measurement

By dielectric measurement the ceramic sample is considered as a parallel plate capacitance. The permittivity (ϵ) can be expressed by:

$$\epsilon = C \cdot d/A \tag{2.5}$$

Where (C) here is the capacitance in Farad, d is the separation between the two planes or the thickness of the sample in m and A is the electrode area in m^2. The permittivity (ϵ) here is equal to $\epsilon_o\epsilon_r$ where ϵ_o=8.85x10^{-12} F/m is the permittivity of free space and ϵ_r is the relative permittivity of the measured dielectric material. In dielectric measurement the capacitance C^* is a complex number where:

$$C^* = C' - jC'' \tag{2.6}$$

C' is the real part and C'' is the imaginary part so that the permittivity (ϵ) consists also of a real and an imaginary part where:

$$\epsilon^* = \epsilon' - j\epsilon'' \tag{2.7}$$

The capacitance is calculated from the measured value of the impedance (Z^*),

$$C^* = \frac{1}{j\omega Z^*} \tag{2.8}$$

where, ω=2πf, $Z^*(\omega)$=V(ω)/I(ω), V(ω) and I(ω) are the corresponding ac voltage and current respectively. In an ideal capacitor the phase shift between the voltage and the current is 90^o, any deviation (δ) from the angle 90^o is described as the loss of power or the dissipation in energy. The measure of this power loss is tan(δ):

$$tan(\delta) = C''/C' = \epsilon''/\epsilon' \tag{2.9}$$

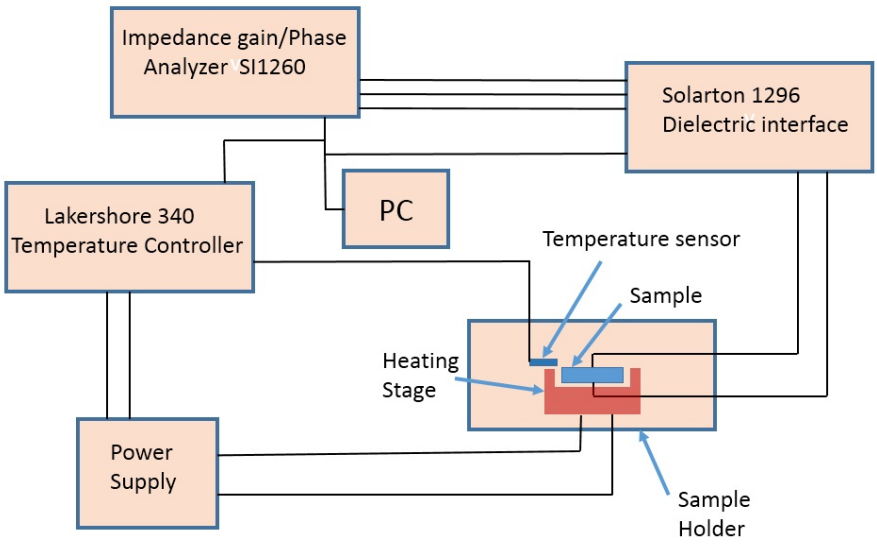

Fig. 2.5: Schematic illustration of the dielectric measurement setup

The dielectric relaxation denotes the change of sample poalrization after application of an electric field. For materials with high permittivity values, the dielectric relaxation is an issue, where the charge carriers (electrons, ions, holes) can contribute in the dielectric polarization. To explain this contribution, Maxwell-Wanger polarization was reported and known also as space charge polarization or interfacial polarization. If we consider composite with two materials, the Maxwell-Wanger effect accounts for charge accumulation at the interface between the two materials. In ferrimagnetic-ferroelectric magnetoelectric composites and when e.g. the polairsation is induced by magnetic field, the accumulation of free charges at the interface causes dielectric dipsersion and losses when applying alternating elelctric fields, this mechanism is knows as the Maxwell-Wagner relaxation [120].

For the dielectric measurement of the different samples we used a Solarton impedance analyzer with temperature control. The setup is schematically illustrated in **Figure (2.5)**. For this measurement the ceramic samples were coated by two parallel electrodes using silver paste and measured using the dielectric setup in the temperature range (300-430K) in the frequency range (1Hz-1Mz).

2.8 SQUID magnetometry

To investigate the magnetic properties of my samples, I used a superconducting quantum interference device (SQUID) magnetometer. A superconducting interference device is one of the most sensitive instruments used for magnetization measurements. It has high sensitivity for measuring small changes in magnetic flux with a magnitude less than Φ_o (2.07 x 10^{-15} Wb) [121]. The main part of the SQUID design is a Josephson tunnel junction which consists of two superconducting materials separated by a weak and thin link. **Figure (2.6)** shows a schematic representation of a SQUID. The measured voltage oscillates with the changes in current phase at the two junctions depends on the change of the magnetic flux. Counting the oscillations allows to evaluate the flux change occurring. Two types of SQUIDs exist, the Radio Frequency (RF) SQUID and the DC SQUID, RF-SQUID (Quantum Design MPMS-5S) was used with cooperation of M.Sc. Soma Salamon and Dipl.-Phys. Joachim Landers to measure the magnetic moments, magnetization hysteresis loops, and temperature dependence of magnetization for different samples. For experiments, a small amount of sample powder was inserted into a gelatin capsule and a piece of paper was inserted in order to fix the powder inside the capsule. After that the capsule was inserted into a plastic straw as a sample holder. The ceramic samples were attached directly to the middle of the straw. The M-H loops were measured by applying maximum magnetic fields of $\pm$1T.

2.9 Mössbauer spectroscopy

This technique is based on the Mössbauer effect which was discovered by Rudolf Mössbuer in 1957. It can be used in chemistry, biology, mineralogy, metallurgy and magnetism [122]. It is based on absorption and emission of nucleus emitted gamma rays in solids. Mössbauer spectroscopy can measure the changes in energy levels of the nucleus. The Mössbauer technique is illustrated in **Figure (2.7)**. It includes a radioactive source with an excited

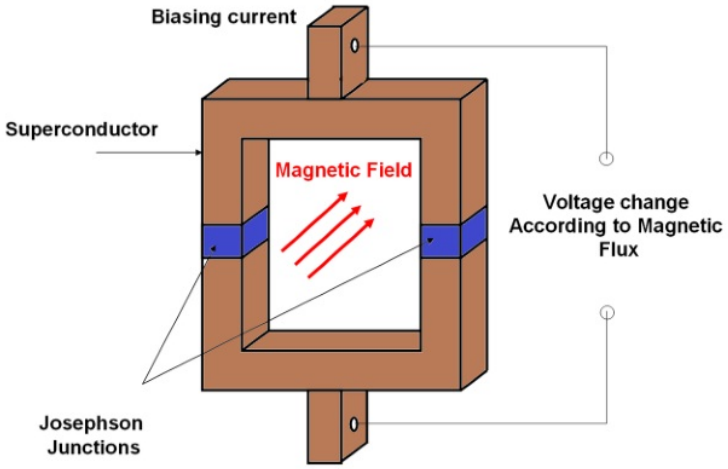

Fig. 2.6: The Josephson device showing two parallel Josephson junctions.

state isotope. In our case ^{57}Fe is used in Mössbauer due to its low gamma ray energy (14.4 keV) and long-lived excited state. The gamma rays here may be partially absorbed by the sample and pass through to an appropriate detector. The source of gamma ray is moving toward and backward to provide the energy scan via the Doppler effect.

Different parameters and nuclear interactions are observed using this technique. The *isomer shift* (δ) is an indication of the measured energy difference between the source energy (E_s) and the absorber energy (E_a). The shift in energy of the nucleus due to the transition of electrons within its orbital can be measured. The isomer shift is useful to find valence states, ligand bonding states, and electron shielding. The *quadrupole splitting* (Δ) can give information about the electric interaction between the electric quadrupole moment of the nucleus and electric field gradients in the surrounding of the probe nucleus [122]. Measuring the splitting can give information about the electron configuration of iron in the material. The *magnetic hyperfine field* (B_{hf}) is the sum of external magnetic field and local magnetic field generated by the surroundings spins. In powder form, a custom built setup was used to study the magnetic structure and all of the Mössbauer measurements mentioned in

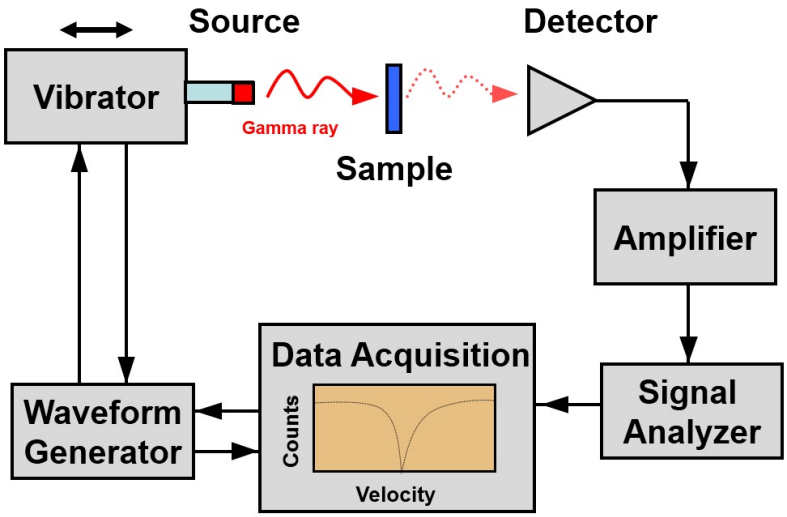

Fig. 2.7: Schematic representation of Mössbauer spectroscopy.

this dissertation are measured and analyzed by Dipl.-Phys. Joachim Landers.

2.10 Magnetoelectric measurement techniques

Two kinds of magnetoelectric measurement routes are usually used to measure the effect. These two routes depend on the mutual orientation of polarization, electric field, and magnetic field. The first route is called the longitudinal magnetoelectric effect (α_{33}) where the specimen surface is placed perpendicular to the applied magnetic field and electrical polarization as shown in **Figure (2.8.a)**. The voltage produced by the sample in the case of direct effect is measured across the sample. The second route is the transverse ME effect (α_{31}) where the applied magnetic field is parallel to the sample surface, and the polarization direction is perpendicular to the sample surface as shown in **Figure (2.8.b)**.

For effective measurements, the sample should be first poled by applying a high dc electrical field and then applying a bias magnetic field with bias electric field at the same direction for the longitudinal measurement and then using a lock in amplifier to measure the output voltage across the sample. A low value of α sometimes results, because of the low resistivity of the ferromagnetic phase (for example $CoFe_2O_4$ in this case), bad poling of the sample according to

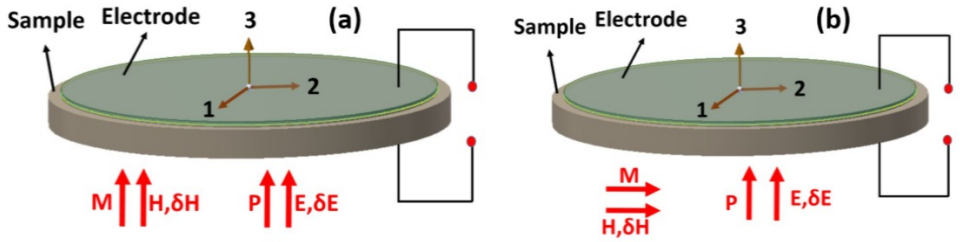

Fig. 2.8: Coordinate system for (a) longitudinal (α_{33}) (b) transverse (α_{31}) ME effect measurement [reprinted with permission from Springer] [55].

wrong connections or bad electrodes, or a high leakage current which may pass through the sample making the poling process impossible. Different fields can be applied to the magnetoelectric sample such as a static field, dynamic field, and pulsed fields. In the next sections, the main techniques and setups used for measuring ME effect and their advantage and disadvantages are presented.

2.10.1 Static method

In this method the magnetoelectric signal is measured as a function of increasing magnetic field [123]. The value of (dE/dH) is measured by the change of voltage produced by the sample according to the dc magnetic field. The output is usually measured using an electrometer with high input impedance. The problem of this method are charges that may accumulate e.g. at grain boundaries and move toward the electrodes during the measurement [124].

2.10.2 Qusai-static method

This method depends on applying a time dependent dc magnetic field with a high impedance electrometer. It relies mainly on increasing the magnetic field with time as indicated in reference [57]. The dc magnetic field is kept constant for 30 seconds and the charges are measured using an electrometer, the time interval is 30 seconds up to 20kOe and then return to zero with the same procedure. This method has also the disadvantage of charges accumulation e.g. in the grain boundaries or in pores.

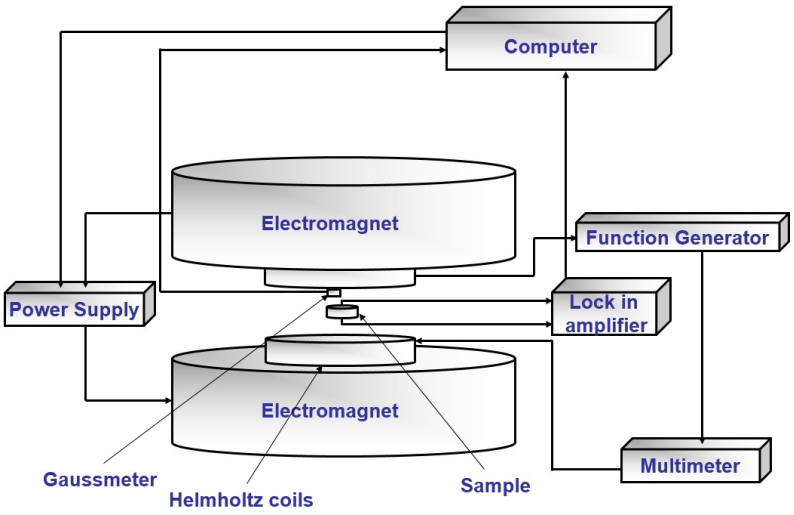

Fig. 2.9: Dynamic lock-in technique setup to measure the direct magnetoelectric effect.

2.10.3 Dynamic lock-in technique

The idea of this method is to prevent charge accumulation during the measurement. This can be prevented using an ac magnetic field generated by Helmholtz coils that also prevent the charges to move towards the electrodes.

The set-up for measuring the ME effect is shown in **Figure (2.9)** [125]. The dc magnetic field is produced by an electromagnet. The variable value for the dc magnetic field is controlled by the power supply. The ac magnetic field is generated by the Helmholtz coils. The value of the ac magnetic field can be controlled by the ac current inside the coils. The intensity of the magnetic field is measured using a gauss meter. In case of ac field, the field was calculated according to the current inside Helmholtz coils, which is measured by a multimeter and verified by a Teslameter. The sample is located in the middle of the electromagnet so that the surface of the sample is parallel to the surface of the electromagnet and perpendicular to H_{ac} and H_{dc} according to the mode of measurement, which can be longitudinal or transverse [126]. For longitudinal measurement, the surface of the sample is perpendicular to the applied magnetic field and for traverse it is parallel. In this method, the used of suitable frequency and the ac magnetic field will prevent or decrease

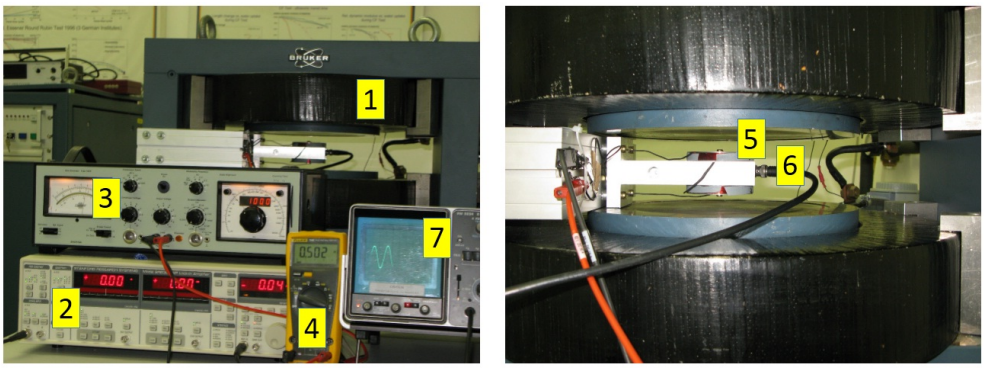

Fig. 2.10: Main parts of the direct ME setup (1) electromagnet for dc magnetic field, (2) lock-in amplifier, (3) function generator, (4) amperemeter, (5) Helmholtz coils for ac magnetic field, (6) coaxial cable connecting to the sample holder, and (7) oscilloscope.

the number of charges that move toward the electrodes [125].

This method measures the oscillation of ME signal due to small ac field. The signal which is collected by lock-in is very small in some cases, lock-in amplifier can provide the option to reduce the noise. The voltage magnetoelectric coefficient is given by the following formula:

$$\alpha_E = \frac{\partial V}{t \cdot \partial H} \tag{2.10}$$

where:

V= voltage measured by the lock-in amplitude

t= thickness of the sample

H= magnitude of ac magnetic field.

Because of the advantages of this method as described before, I have designed a setup to measure the direct ME effect using the lock-in technique. The main parts are shown in **Figure (2.10)**. The setup consists of an electromagnet that produces a dc magnetic field, in our case (0-4000)Oe. Helmholtz coils produce the ac magnetic field. A lock-in amplifier (Standford Research systems SR 830) is used to determine signal amplitude.

In order to obtain ac magnetic fields between (0-40Oe), Helmholtz coils

were designed with 160 windings in each coil. The generated magnetic field is calculated according to the following equation:

$$B = (\frac{4}{5})^{1.5} \cdot (\frac{\mu_o nI}{R}) \tag{2.11}$$

where μ_o is the permeability of free space, n is the number of windings in each coil, I is the current through the windings and R is the coils radius. The current inside the Helmholtz coils was driven by a functional generator. The ac magnetic field produced by the Helmholtz coils was measured and the values were recorded for different currents and frequencies and found to be (0-45)Oe which is compatible with the calculated values from **Equation (2.11)**. The direct ME effect was measured simultaneously by applying a dc magnetic field and an ac magnetic field. The voltage generated by the sample was measured using lock-in amplifier and the ME coefficient was calculated using the **Equation (2.10)**. The measurements were done using a frequency of 3Hz and at room temperature.

2.10.4 Pulsed dynamic method

In this technique, a sample is placed between two electromagnets that produce a bias magnetic field, then a pulsed magnetic field parallel to the filed produced by the magnets is applied by passing a current inside a coil surrounding the sample **Figure (2.11)** . The pulses applied to the coil are produced by a pulse generator. The input pulse for the coil and the output voltage across the sample are measured using a digital oscilloscope [127].

2.10.5 Measurements via SQUID ac-susceptometer

SQUID magnetometry has been adapted to measure the magentoelectric coefficient [128]. It is used to measure the electrically induced magnetization when applying an ac electric field to the sample [129]. In other words, it is used to measure the converse magnetoelectric effect as explained in **Figure**

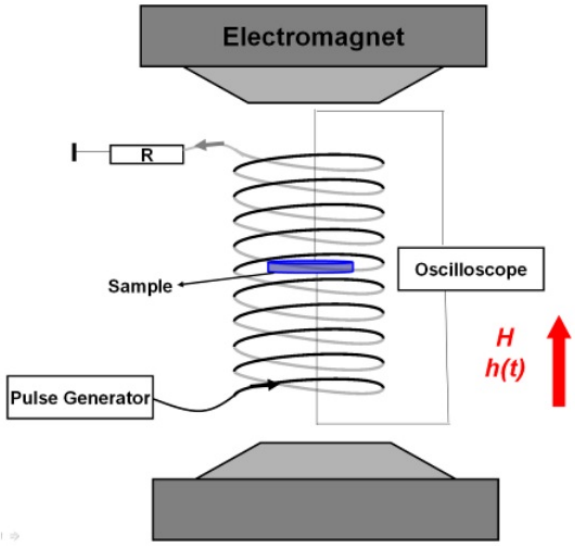

Fig. 2.11: Schematic illustration of the pulsed dynamic method.

(2.12). The power supply shown in the figure delivers an ac voltage with the value V=$V_o$cosωt. The magnetoelectric coefficient is evaluated according to the following equation:

$$\alpha_c = \mu_o \partial M_{ME} / \partial E_{ac} \tag{2.12}$$

where

α_c = the converse magnetoelectric coefficient

μ_o = the permeability of free space and is equal to $4\pi \cdot 10^{-7}$ V·s/A·m

M_{ME} = first harmonic component of the electrically induced magnetization

E_{ac} = ac electric field

In this thesis, I have chosen two different ME measurement techniques to measure the magnetoelectric effect. The first one is the converse technique using SQUID magnetometery due to the higher sensitivity measurement offered by SQUID comparing to other devices. These measurements were done with cooperation of M.Sc. Soma Salamon. The second one is the lock-in technique for the direct ME measurements which was already designed and constructed

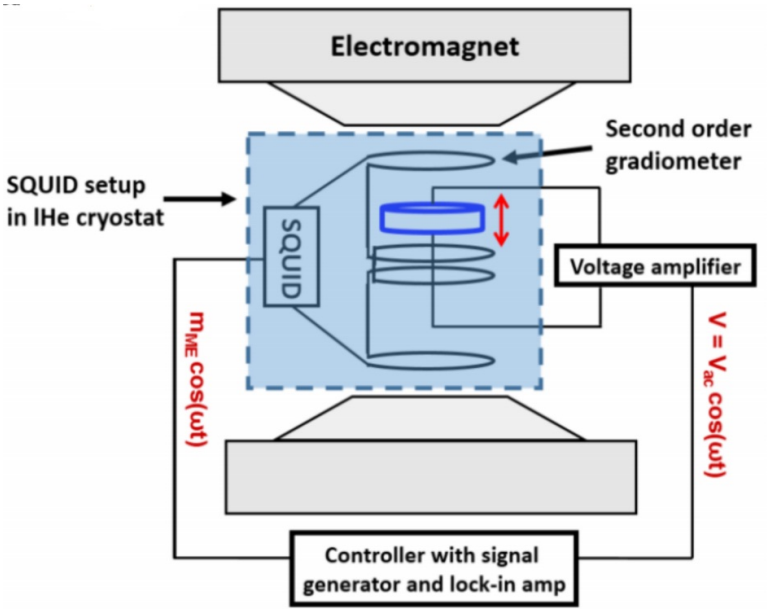

Fig. 2.12: Schematic diagram of using SQUID to measure the converse ME effect [55].

by me in our group. Comparison of the results obtained by the two methods will be described throughout the thesis.

2.11 Synchrotron radiation

In order to measure the magnetic field-dependance of electric polarisation at the surface, the synchrotron radiation was used on my samples by Dr. Carolin Schmitz-Antoniak. The beamline UE46-PGMI, at HZB-BESSYII was used in order to utilize the soft X-rays regime. Electrons are accelerated to a certain speed in a circular path which by transverse acceleration emits electromagnetic radiation. This radiation has specific polarization and frequency. **Figure (2.13)** shows a schematic drawing of the main parts of the BessyII synchrotron. The electrons are generated using an electron gun, then pre-accelerated in the microtron, and then injected to the synchrotron. The electrons are kept at constant energy in the (storage ring). The synchrotron radiation is produced at the bending magnets (dipole magnets) or in the (undulators) (see **Figure (2.13)**).

The undulator consist of several magnetic dipoles with orthogonal orien-

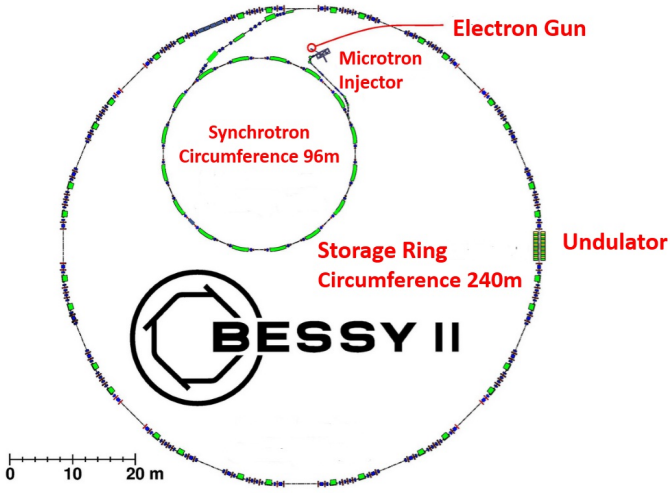

Fig. 2.13: Schematic drawing of the facility BESSYII [130].

tations. The electrons are passing through the magnetic field in the gap of the undulator (see **Figure (2.14)**) and hence emit radiation. **Figure (2.14)** shows the operational modes of the undulator (UE46) in the beam line PGM-1, the magnets are arranged in two planes. Each plane contains two magnets, the gap distance between them is important, because it determines the amount of the emitted radiation energy and the phase shift for polarization. If the two rows coincide, this is called linear horizontal polarization **Figure (2.14.a)**. If one row is shifted causing a phase shift of $\lambda/2$, the electrons move in the horizontal (vertical) plane emitting horizontal (vertical) linear polarized radiation **Figure (2.14.b)**, respectively. The generation of the circularly polarized X-rays can be obtained when the shift is equal to $\lambda/4$. The beam lines are also equipped with focusing optics and a monochromator which consist of dispersive elements that are used to grate the soft X-rays for further investigations.

X-ray absorption spectroscopy in the soft X-ray regime was performed at the high field end state at the helical undulator beamline UE46-PGM1. The drain current was measured for the samples at a temperature of T=290K. Magnetic fields up to 1.5T were applied parallel or perpendicular to the $\vec{k}$ vector of the incoming X-rays. The X-ray linear dichroism (XLD) was measured at the Ti $L_{3,2}$ absorption edges. For that, the photon energy between

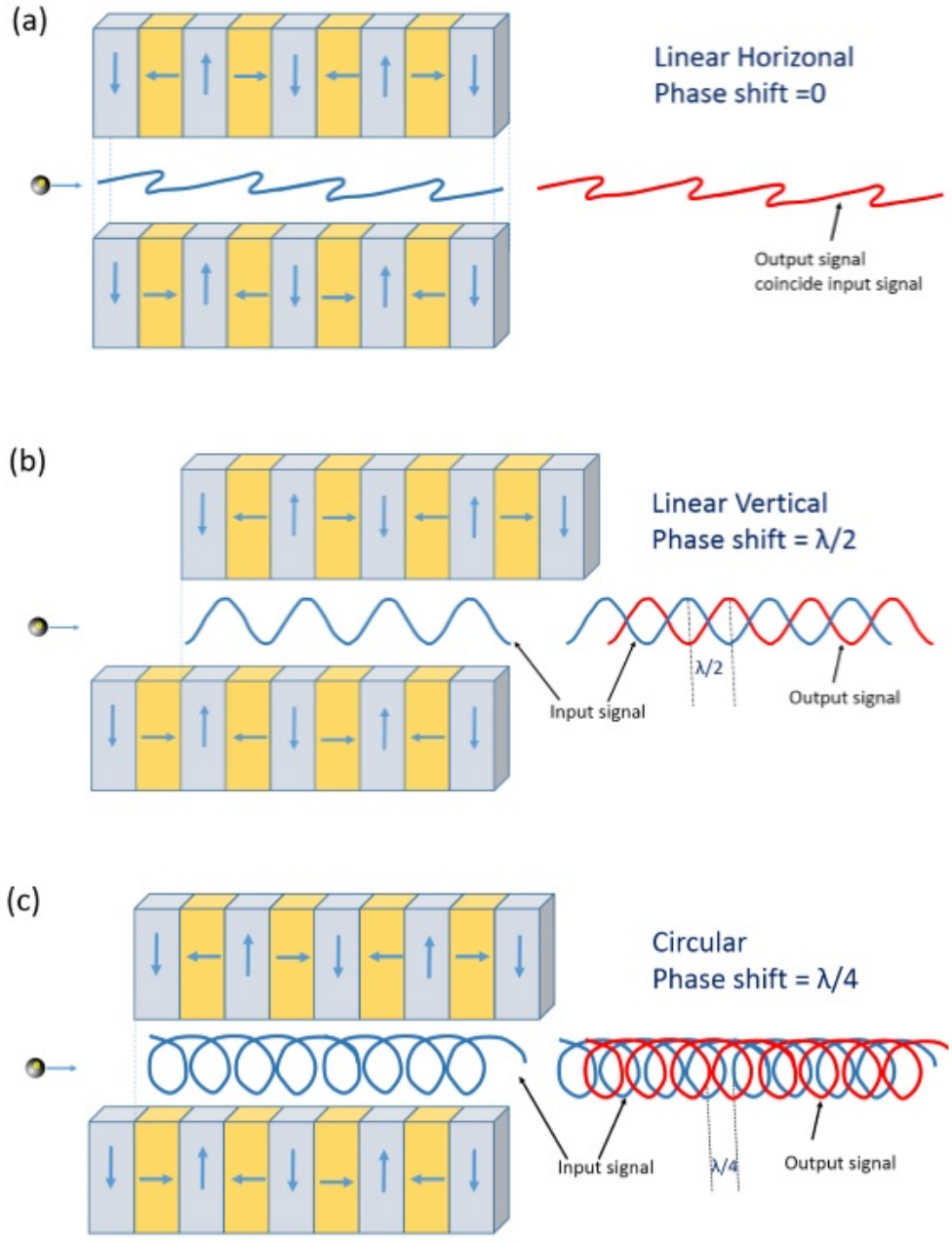

Fig. 2.14: Operational modes of the undulator UE46 [130]

440 eV and 500 eV with scan speed of 0.35 eV/s for either horizontally or vertically polarized X-ray was utilized. A small charging effect was observed by monitoring the sample drain current. The measurements were started after 10 minutes when the signal was stable. Measurements were performed in grazing incidence (θ_k=60^o) with the main component of the magnetic field vector applied perpendicular to the sample surface (θ_H=-30^o). The electric field vector for the horizontally polarized X-rays is parallel to the magnetic field vector, where the electric field vector for vertically polarized X-rays is in the sample plane, the detailed procedures can be found in [131]. Magnetic field-dependent element-specific magnetization curves were measured by detecting the sample drain current for left or right circularly polarized X-rays at the photon energy of maximum X-ray magnetic circular dichroism (XMCD) at the Fe L_3 absorption edge for different values of external magnetic field.

3. PREPARATION AND MAGNETIC PROPERTIES OF $CoFe_2O_4$ NANOPARTICLES

In this chapter, I describe the preparation method for synthesizing cobalt ferrite nanoparticles and their structural, thermal and magnetic properties. Cobalt ferrite ceramic samples with their structural and magnetic properties will be also discussed. All the powder in this chaper was synthesied by myself in our group in the chemistry laboratory. The morphology for different powders was scanned with cooperation of M.Sc. Yanling Gao. Mössbauer and magnetic properties were measured with cooperation of M.Sc. Soma Salamon and Dipl.-Phys. Joachim Landers in the faculty of physics on the Duisburg campus.

3.1 Background

$CoFe_2O_4$ is one of the most widely used ferrimagnetic materials in ME composites due to its large magnetostriction [70]. Measurements on cobalt ferrite showed a large variety of magnetic properties depending on grain size. Grain size can be controlled by the annealing temperature. When increasing the annealing temperature the particle size becomes bigger and, therefore, the saturation magnetization and the coercive field usually increase [132]. Synthesis of $CoFe_2O_4$ with controlled grain size is necessary in order to determine the final product function. Going to the nano-scale particles of cobalt ferrite is of high interest whether the magnetic properties and functionality can be enhanced. In this chapter, the synthesis of $CoFe_2O_4$ nanoparticles using the co-precipitation method is shown. The correlation between particle size

and the magnetic properties is discussed. $CoFe_2O_4$ ceramic samples have also been synthesized in order to investigate the effect of grain size on the magnetic properties.

3.2 Synthesizing $CoFe_2O_4$ using the co-precipitation method

Several methods have been used to synthesize $CoFe_2O_4$ nanoparticles. These methods include co-precipitation [132–135], sol-gel auto combustion [95], and forced hydrolysis [136]. **Table (3.1)** summarizes some of these methods with the resulting magnetic properties and particle sizes. Agglomeration of particles is the most important difficulty, where special techniques should be provided to the powder in order to separate the particles. In this chapter we report on synthesis of less-agglomerated $CoFe_2O_4$ nanoparticles based on the co-precipitation method utilized by Zhang [133]. The method is relatively simple, has low production cost, and provides small particle sizes. For co-precipitation, the particle sizes produced are distributed from 7 to 30 nm (**Table(3.1)**). The saturation magnetization, coercive field, and remnant magnetization depend on particle size.

Tab. 3.1: Different synthesis methods of $CoFe_2O_4$ nanopowder and their room temperature magnetic properties

Method	D nm	M_s Am^2/kg	H_c kA/m	M_r Am^2/kg	Ref.
Co-Precipitation	7.4	5.54	27.51	0.68	[132]
Co-Precipitation	11.5	36.24	53.58	10.14	[133]
Organic acid	-	67.74	73.08	32.38	[93]
Co-Precipitation	20-30	61.77	41.32	14.39	[134]
Co-Precipitation	24	68	95.93	31.7	[135]
Polyol synthesis	21.5	86	-	59.34	[94]
Sol-Gel	10	-	-	-	[137]
Forced Hydrolysis	4-8	55	0	0	[136]
Auto combustion	15	53	96.69	27	[95]
Hydrothermal	17	63	66.15	23	[138]

In order to control particle size, the co-precipitation method was applied here. Iron nitrate nonahydtrate and cobalt nitrate hexadydtrate were the pre-

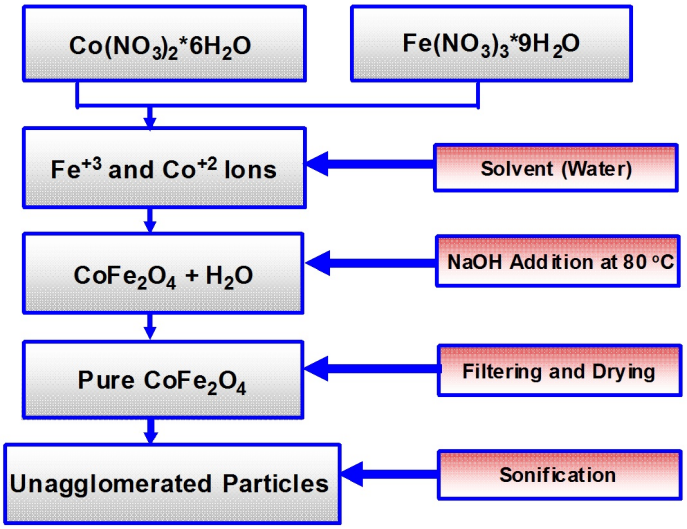

Fig. 3.1: Synthesis of $CoFe_2O_4$ nanoparticles by the co-precipitation method.

cursors and sodium hydroxide was the precipitating agent. Particle sizes in the precipitated material strongly depend on the pH value of the precipitation agent. The chemical procedures are summarized by **Figure (3.1)**. 0.02 mol of $Fe(NO_3)_3{\cdot}9H_2O$ were dissolved with 0.01 mol of $Co(NO_3)_2{\cdot}6H_2O$ in 200 ml water (solvent) at room temperature in ambient atmosphere. After about 1 hour of magnetic stirring to dissolve the two ingredients in water, the temperature was increased to about 90^oC. The color changed to dark orange, which is an indication of complete dissolution of Fe^{+3} and Co^{+2} ions in the solution. The precipitation agent (NaOH) was added to the solution drop by drop in amounts of 0.1, 0.25, 0.625, 1.25 and 2.5mol separately which are equal to the concentration values (1, 2.5, 6.25, 12.5, 25) mol/L respectively. The color of the solution changed to black which is an indication of $CoFe_2O_4$ particle formation. The reaction equation is as follows:

$$2Fe(NO_3)_3 + Co(NO_2)_3 + 8NaOH = CoFe_2O_4 + 8NaNO_3 + 4H_2O \quad (3.1)$$

For homogenizing, the temperature was kept at 90°C for 2 hours, then the solution was cooled down to ambient temperature. The solution was sonificated 2 times in an ultrasonic bath for about 20 minutes. Proper sonification,

drying and several washings of the powder separate the particles well, and may decrease the agglomeration degree where the agglomeration is the result of the magnetic dipole interactions as well as the attractive van der Waals forces between the magnetic particles. After several times of ionized water, ethanol and acetone washing in order to remove the rest of sodium hydroxide, the powder was dried at 100°C in a chamber furnace and grounded gently afterward.

3.3 Phases, morphology, and structural analysis of the $CoFe_2O_4$ nanopowders

X-ray diffraction was used to analyze the phases and the unit cell parameters for the obtained nanopowder. The result of XRD is shown in **Figure (3.2)**. The pattern was compared to the known data bank file (pdf 22-1086) [139]. The data show single phase $CoFe_2O_4$ without impurities or other interference phases. It reflects the spinel structure. The software (Jade) was used here in order to determine the unit cell parameter, which was about a = 8.38 Å. This is very close to the value found for bulk $CoFe_2O_4$ a = 8.384 Å[140]. The crystallite size (D) was calculated from the Scherrer **Equation (2.4)** and found to be 20nm as estimated from the strongest diffraction peak corresponding to the [311] plane and taking into consideration the shape factor value of 0.9.

For better understanding the physical and chemical properties of the nanopowders, TGA and DTA analysis were done (**Figure (3.3)**). The results correspond to the sample synthesized using 6.25 mol/L NaOH. The weight starts to decrease at about 50^{o}C reaching 700^{o}C with a total weight loss of about 7.7 percent.

Using the DTA analysis two endothermic and exothermic peaks are notified. The first one is the valley in temperature range 25-130^{o}C which is an indication of endothermic process attributed to the dehydration or the loss of water in the sample. The weight loss in this valley is about 2 percentage only. The

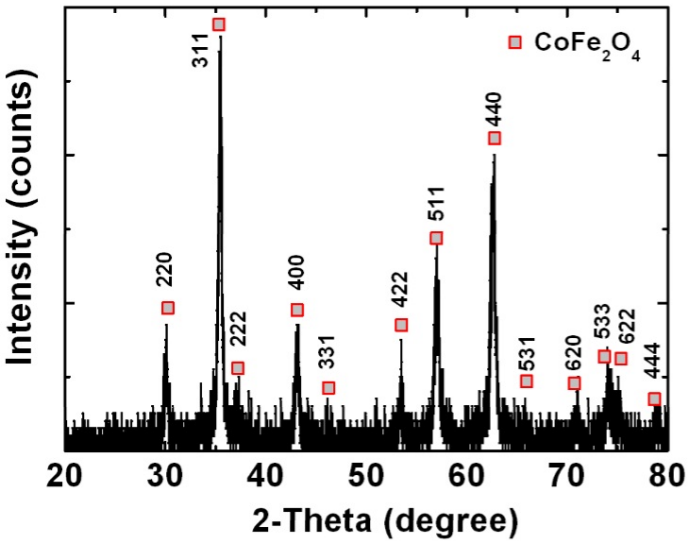

Fig. 3.2: XRD for $CoFe_2O_4$ nanoparticles synthesized with 1 mol/L NaOH [141].

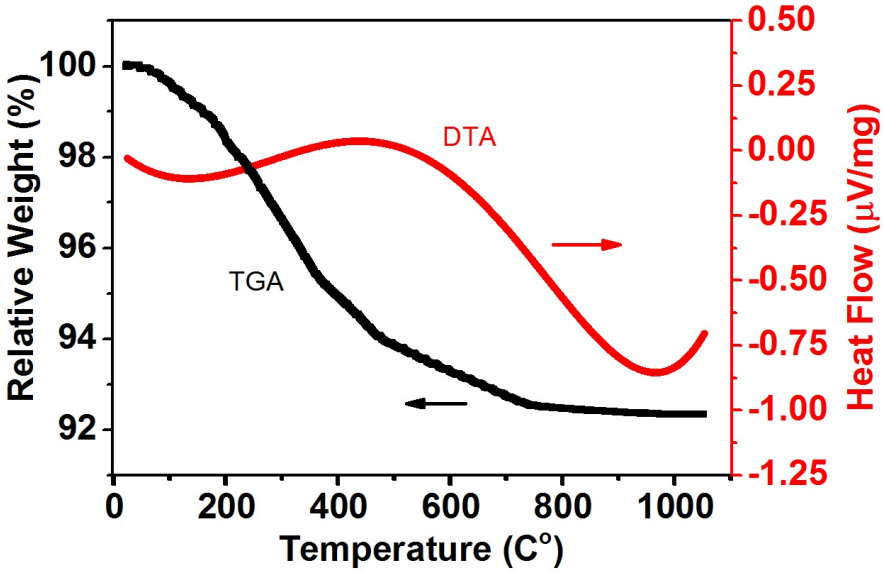

Fig. 3.3: Differential thermal analysis (DTA) and thermogravimetric analysis (TGA) for the as prepared $CoFe_2O_4$ nanoparticles[NaOH, 6.25 mol/L] [141].

exothermic peak from temperature about 200°C to about 500°C is due to crystallization of $CoFe_2O_4$. The weight loss in this stage is in the range of 5.5 percentage as indicated by the TGA curve. For temperature more than 700°C, no considerable loss in the weight was notified.

The morphology of the $CoFe_2O_4$ powders is illustrated in **Figure (3.4)**. The figures show different particle sizes with respect to the amount of NaOH used in the co-precipitation method. A software program (analySIS) (Soft Imaging System) was used to determine the particle sizes (D). The particle sizes were distributed as (24±4), (27±3), (29±4), (38±6) nm for 25, 12.5, 2.5, and 1 mol/L NaOH, respectively. The agglomeration is an essential issue that affects the specification of the final product so that controlling particle sizes with less agglomeration is the most important step in order to synthesize nanocomposites.

The SEM data illustrate that the increasing amount of NaOH decreases the particle sizes, but the degree of agglomeration increases. **Figures (3.4.a)** and **(3.4.b)** show less degree of agglomeration while the **Figure (3.4.d)** shows the highest. **Figure (3.5)** shows transmission electron microscopy data for $CoFe_2O_4$ nanoparticles synthesized using 1 mol/L NaOH. Most of the particles shown in the figure are spherical in shape. The average crystallite size is in the range of 30-40 nm which is compatible with SEM data, but larger than the one estimated from XRD data. Using XRD to calculate the particle size distribution is an issue, because the strain over the particle surfaces may cause broadening of the Braggs reflections, which can be interpreted as a reduction in particle size [132].

Figure (3.5.b) shows a single particle of $CoFe_2O_4$ measured by high resolution transmission electron microscopy. The dark area represents one single particle. The cubic spinel structure of $CoFe_2O_4$ is also confirmed by **Figures (3.5.c)** and **(3.5.d)**. The beam was in the direction of [011] and the interplanar distance for the planes (220), (311), (400), (331), (422), (511) and (440)

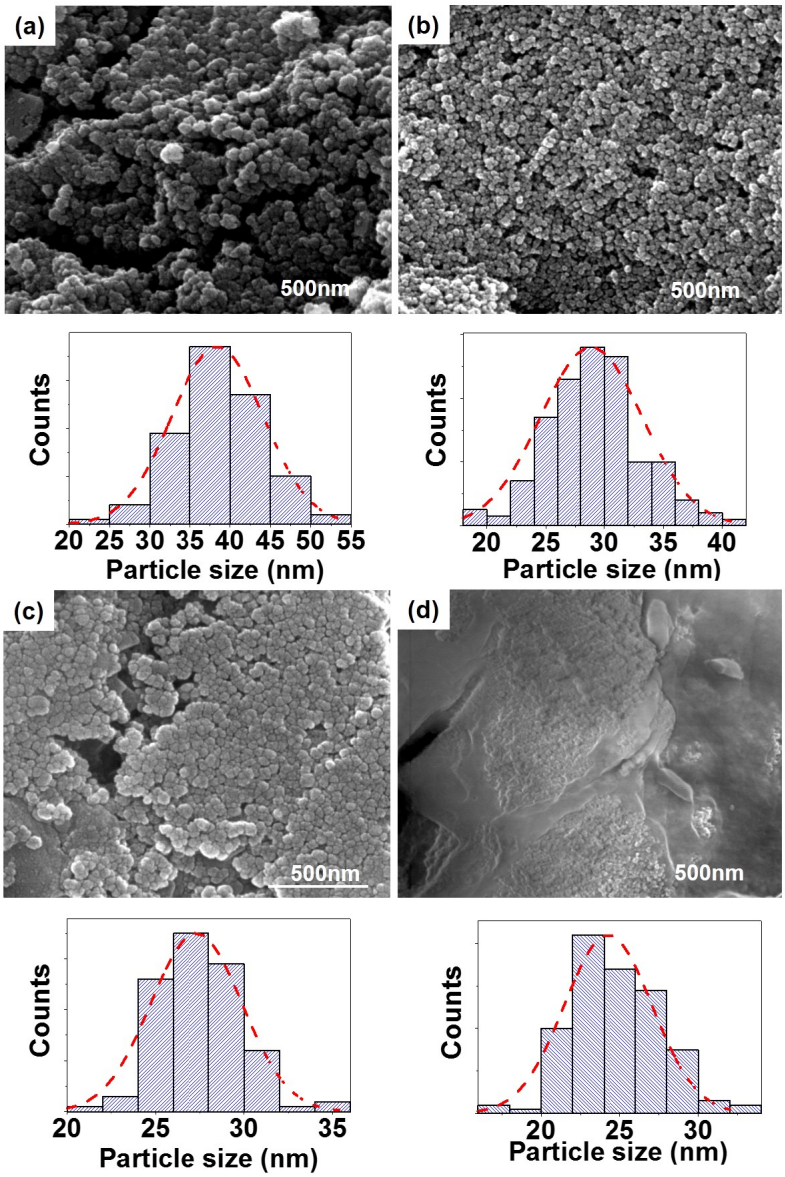

Fig. 3.4: Scanning electron microscopy images of $CoFe_2O_4$ as prepared powder with NaOH added amounts (a) 1 (b) 2.5 (c) 12.5 and (d) 25 mol/L and the corresponding particle sizes fitted with a normal distribution [141].

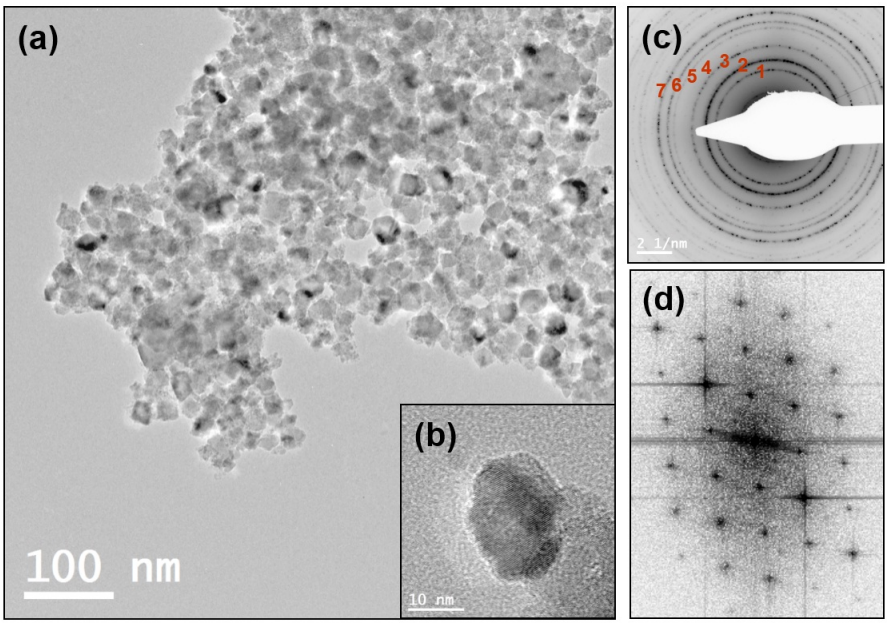

Fig. 3.5: Transmission electron microscopy photographs for $CoFe_2O_4$ showing (a) nanoparticles (b) HTEM for single particle (c) (SAED) selected area electron diffraction for the single particle of $CoFe_2O_4$ (d) Fast Fourier Transformation FFT pattern (Beam direction [011]) [141].

are measured using **Figure (3.5.d)** and illustrated in **Table (3.2)**. The interplanar spacing measured by TEM and measured by XRD are compatible to each other and compatible with the data file (pdf (22-1086)) for cubic spinel structure of $CoFe_2O_4$. The average unit cell parameter was measured to be a = 8.373±0.01 Å which is consistent with the bulk value a = 8.378±0.006 Å previously reported [142].

Tab. 3.2: Different interplanar d-spacing measured by XRD, TEM and compared to pdf (22-1086)

Ring #	Plane	Measured d-spacing TEM (nm)	d-spacing XRD (nm)	d-spacing ref [139]
1	220	0.300±0.005	0.296	0.297
2	311	0.253±0.005	0.253	0.253
3	400	0.210±0.005	0.209	0.210
4	331	0.189±0.005	0.190	0.192
5	422	0.172±0.005	0.171	0.171
6	511	0.163±0.005	0.161	0.162
7	440	0.150±0.005	0.148	0.148

The effect of calcination temperature on the particle sizes was studied. The

powder prepared by 2.5 mol/L of NaOH was chosen and calcined at different temperatures. The corresponding SEM photo is shown in **Figure (3.6)**, the particle size for the starting powder used was about 31 nm. The size increased slightly and reached to 39 nm after calcinatation at a temperature of 900°C for 15 minutes. The increase of the particle sizes is related to the grain growth. However, no significant increase in the particles sizes was seen even at calcination temperature of 900°C. At 900°C the particles are getting closer to each other which explains the increased agglomeration at increasing temperature. However, more time and higher temperature are usually needed for increasing particle sizes.

For further investigation about grain growth of $CoFe_2O_4$ nanoparticles for longer times and more temperatures, the sample of 39 nm from **Figure (3.6)** was treated thermally at 3 different temperatures 800°C, 900°C and 1000°C during 1.5 hours each. The grain growth was calculated by dividing the change in particles diameter by the period of annealing. **Figure (3.7)** illustrates the increased of particles size with temperature and the grain growth rate. The rate of growth reached to 1.4 nm/min at 1000°C while it was 0.4 nm/min at about 800°C. A big jump in grain growth was notified at 1000°C. A particle size of about 165 nm was measured at 1000°C.

3.4 Magnetic properties of $CoFe_2O_4$ nanoparticles

For the magnetic properties, room temperature M(B) hysteresis loops were measured using SQUID magnetometry for samples with different particle sizes. The maximum applied H field was 1T. **Table (3.3)** summarizes the magnetic properties of the as prepared $CoFe_2O_4$ nanoparticles extracted from **Figure(3.8)**.

The shapes of the curves are an indication of superparamagnetism as shown in **Figure (3.8)** which was also previously reported in literature for such magnetic nanoparticles. This behavior is commonly seen for particles less

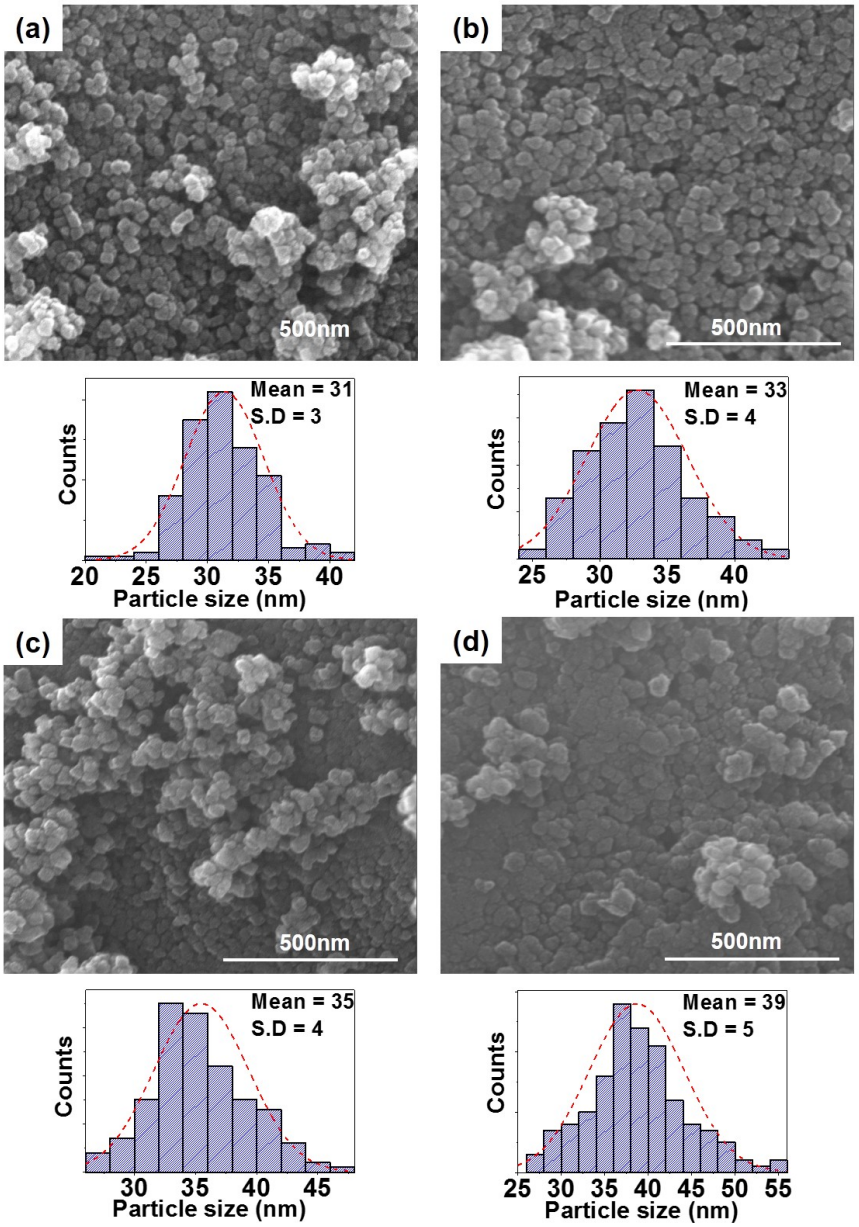

Fig. 3.6: SEM micrograph for $CoFe_2O_4$ nanoparticles synthesized by 2.5 mol/L NaOH (a) as prepared powder (b) calcinated at 550°C for 15 minutes (c) calcinated at 750°C for 15 minutes (d) calcinated at 900°C for 15 minutes.

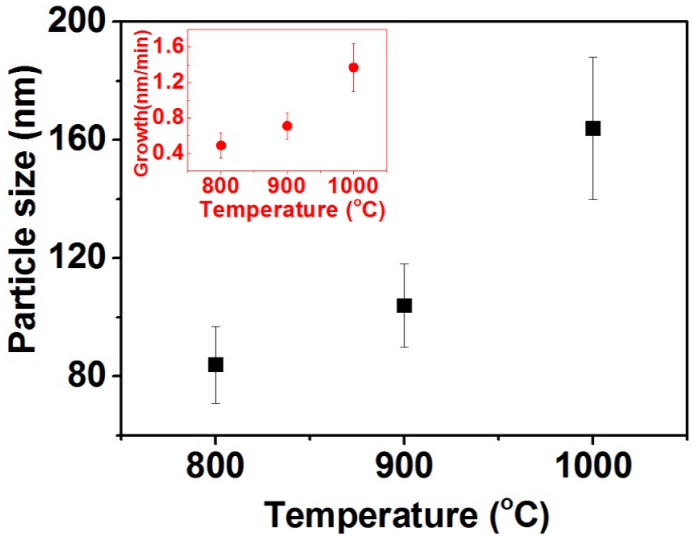

Fig. 3.7: Particle size vs. temperature for $CoFe_2O_4$ nanopowder treated at 800°C, 900°C, 1000°C for 1.5 hours each (the inset shows the grain growth per minute for different temperatures).

Tab. 3.3: Room temperature magnetic properties of $CoFe_2O_4$ nanoparticles

Sample	D (SEM) (nm)	M_s (Am^2/kg)	M_r (Am^2/kg)	H_c (kA/m)	M_r/M_s
Bulk ref[142]	200-2000	85	25	48	0.29
1 mol/L	38±6	60	3	3	0.05
2.5 mol/L	29±4	50	23	10	0.46
12.5/L mol	27±3	35	19	12	0.54
25 mol/L	24±4	45	4.5	4	0.1

than 40nm. The maximum saturation magnetization is found for the sample synthesized by 1 mol/L NaOH with the largest particle size. It is clear from the data and **Figure (3.8)** that the increasing of particle size increases the saturation magnetization. The same behavior of increasing the saturation magnetization with respect to particle size increase was reported by Maaz et al. for particle size range of 15-50 nm [135]. They attributed the decrease in saturation magnetization of small particle sizes to the effect of relatively inert surface layer which has low magnetization. In fact, the increase of saturation magnetization with respect to particle size increase can be attributed to the increase of collinear magnetic structure which causes the magnetic moment to align with the direction of magnetic field [143]. The maximum saturation

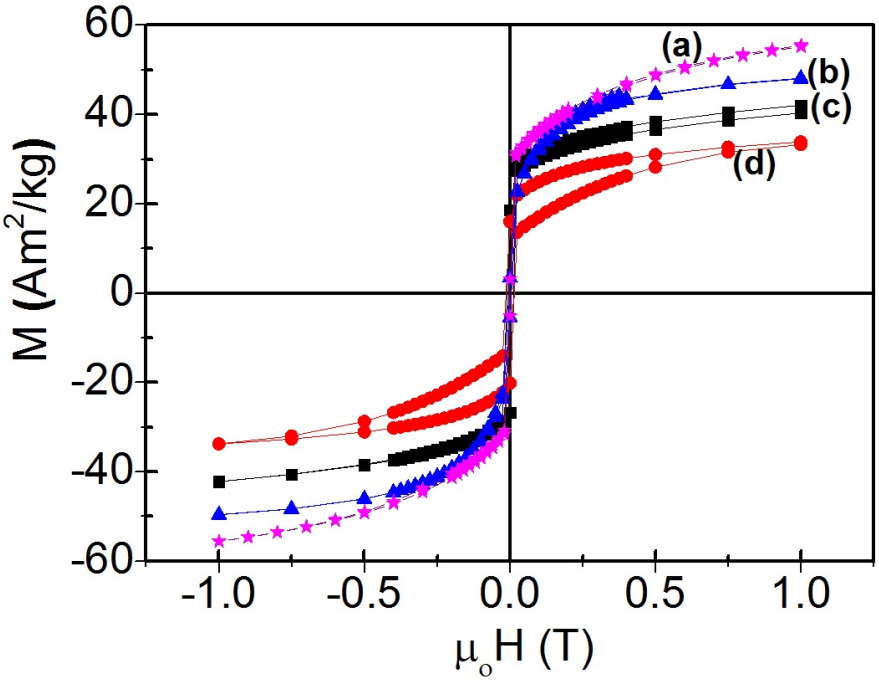

Fig. 3.8: B-M hystersis loop for $CoFe_2O_4$ particle sizes synthesized by (a) 1 mol/L (b) 25 mol/L (c) 2.5 mol/L (d) 12.5 mol/L NaOH [141].

magnetization of 60 Am^2/kg is still lower than the bulk value 85 Am^2/kg shown in **Table (3.3)** [142].

For coercivity it was found that all the samples have a coercive field lower than the bulk value [142]. An increase of coercivity was found for the particle sizes 27 and 29 nm with values 12 and 10 kA/m, respectively, compared to other samples. However, the lowest coercive field was measured for cobalt ferrite with particle size 38nm. This trend appeared in the report of El-Okr et al. [132], they attributed the increase in coercivity to the combination of the anisotropy of the surface and thermal energies. In case of remnant magnetization values, low remnant values were recorded for particle sizes 38 and 24nm which were 3 and 4.5 Am^2/kg, respectively. The values of squareness for these samples are lower than 0.5, while the squareness was recorded to be around 0.5 for samples with particle sizes 27 and 29nm. However, the value of squareness around 0.5 is an indication of uniaxial magnetic anisotropy system [144].

For the sample prepared by using 6.25 mol/L of NaOH , the Mössbauer spectra were investigated. **Figure (3.9)** shows the spectrum without an external magnetic field taken at temperature 80K. The green line represents the fitted spectrum with a broadened sextet [the line width Γ as shown in **Table (3.4)**] for the Fe^{3+} in A-sites. The blue line represents the distribution of the hyperfine fields for Fe^{3+} in the B-sites. It is well known that a fraction of Co^{2+} ions located on the tetragonal sublattice leads to a non unique nearest-neighbor A-site configuration. Therefore the distribution represents the various contributions with six, five and four Fe^{3+} ions on the A-sites which decrease hyperfine fields due to the reduced supertransferred hyperfine fields. All of the Mössbauer parameters are shown in **Table (3.4)** which is compatible with literature values of bulk cobalt iron oxide [145]. By comparison between areas of the A and B lines in **Table (3.4)**, the inversion parameter s can be calculated by the following equation:

$$s = \frac{2 \cdot R_{AB}}{1 + R_{AB}} \tag{3.2}$$

Where the value of R_{AB} is equal to the area of spectrum A divided by the area of spectrum B, $R_{AB} = A_A/A_B$. For pure cobalt ferrite, the value of the inversion parameter is an indication of the inverseability of the spinel structure as described in **Section (1.9)**. The calculation of the s value using spectral areas in Mössbaue data revealed that s=0.9. This value corresponds to the following stoichiometry $[Co^{+2}{}_{0.1}Fe^{+3}{}_{0.9}]_A[Co^{+2}{}_{0.9}Fe^{+3}{}_{1.1}]_BO_4$ and compatible with pure cobalt ferrite previously reported [88].

3.5 Structural and magnetic properties of $CoFe_2O_4$ ceramic

For ceramic $CoFe_2O_4$, the traditional way of sintering in normal oven was used as well as the technique of SPS (spark plasma sintering). For ceramic samples, it is important to analyze the grain sizes and the surfaces. For morphology investigation, the samples were polished and thermally etched

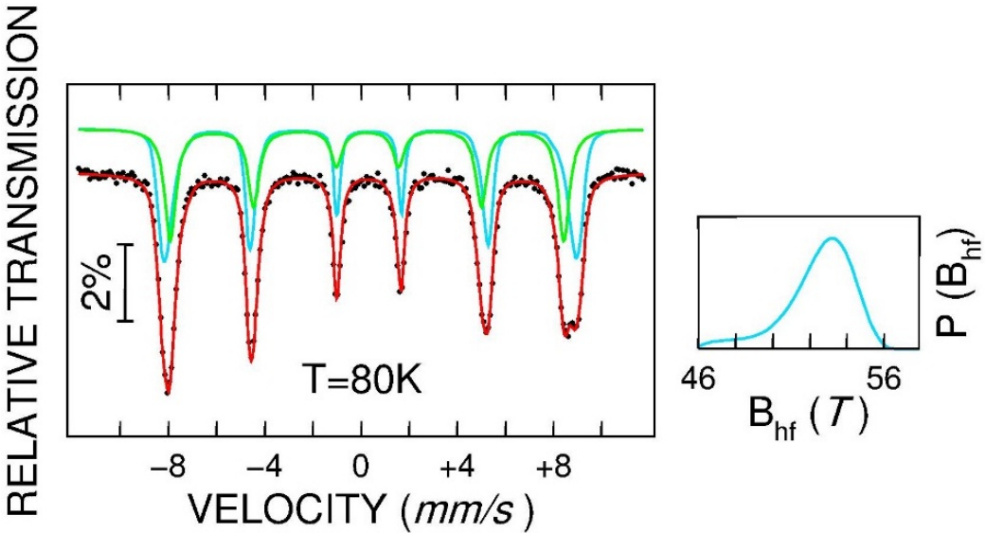

Fig. 3.9: Mössbauer spectrum of a cobalt ferrite nanopowder synthesized by 6.25 mol/L NaOH and measured at T=80K at zero external magnetic field [141].

Tab. 3.4: Spectral Mössbauer parameters of the Co-ferrite powder at T = 80 K in zero external field, B_{hf}=magnetic hyperfine field, Δ=quadrupole splitting, δ= isomer shift, Area = relative spectral area, Γ=full line width at half maximum. Values for the distribution are average values. The isomer shifts δ are given relative to α-Fe at room temperature [141].

	B_{hf} (T)	Δ (mm/s)	δ (mm/s)	Area (%)	Γ (mm/s)
A-site, (sextet)	50.68(4)	-0.02(1)	0.38(1)	45	0.56(2)
B-site, (B_{hf} distribution)	52.49(7)	0.05(1)	0.48(1)	55	0.28

at temperature 100^oC below the sintering temperature. Thermal etching is the best etching method for ceramic oxides. To improve the reflectivity of the surface in SEM scans, the surface was coated by a layer of gold using sputter coating. The morphology of the cobalt ferrite sample sintered by SPS is shown in **Figure(3.10)**. The surface is flat and the grain boundaries are not clear due to proper polishing of the surface see **Figure(3.10.a)**. **Figure(3.10.b)** shows the etched surface with clear grain boundaries and grain size distribution of 144±20 nm.

For comparison, a sample of $CoFe_2O_4$ was normally sintered in the normal oven at 1200°C for 2 hours and shown in **Figure(3.11)**. The $CoFe_2O_4$ ceramic is very dense and the grain boundaries are clear and grain sizes in the range

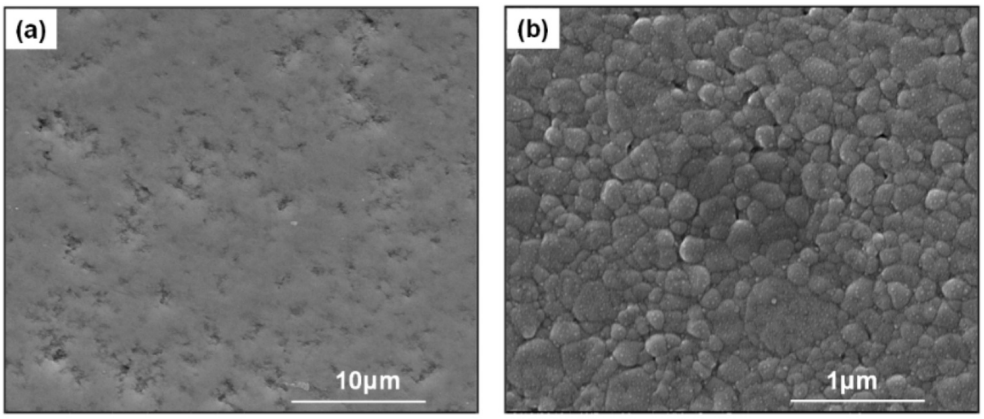

Fig. 3.10: $CoFe_2O_4$ ceramic sample sintered by SPS at 900°C for 5 minutes and polished (a) without etching (b) thermal etching at 800°C for 30 minutes.

of 2μm. The difference between the two methods is the resultant grain sizes of cobalt ferrite. It is clear that the sample which was sintered using spark plasma produces smaller grains comparing with the normal sintering one.

For the magnetic properties for both ceramic samples, the sample which was sintered by normal sintering method exhibits more saturation magnetization which is exactly the same as the bulk value reported by [142] but with very low coercive field. All of the parameters M_s, M_r and H_c for both ceramic samples are larger than the nanopowder parameters shown in **Figure (3.12)** and **Table (3.5)**.

Tab. 3.5: Properties of $CoFe_2O_4$ samples (1) nanopowder (2) ceramic sample sintering by spark plasma at 900°C (3) Ceramic sample sintering by normal oven at 1200°C.

Sample	D (SEM) (nm)	M_s (Am^2/kg)	M_r (Am^2/kg)	H_c (kA/m)	M_r/M_s
1	40	60	2	2	0.033
2	144	80	24	27	0.30
3	2000	85	18	21.5	0.21

For comparison, magnetization M-H loops were measured and shown for cobalt ferrite nanopowder sample with 40nm grain size, normally sintered sample and the SPS sample, see **Figure (3.12)**. The differences in magnetic properties are clear and the three samples start to saturate at magnetic field

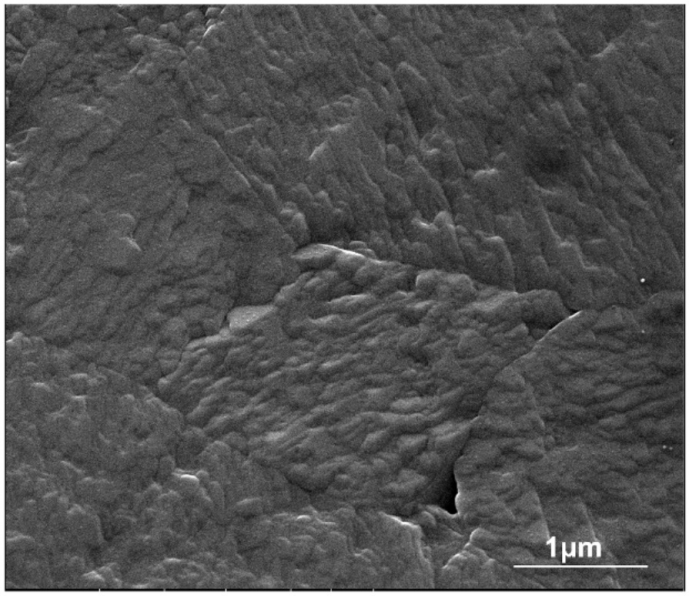

Fig. 3.11: $CoFe_2O_4$ ceramic sample sintered by normal oven at 1200°C for 2 hours.

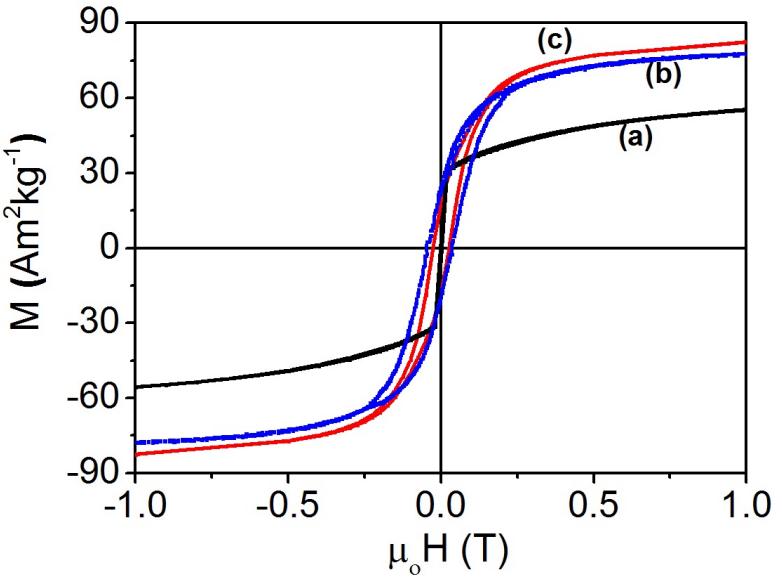

Fig. 3.12: Room temperature B-M loop (a) 40nm $CoFe_2O_4$ powder (b) $CoFe_2O_4$ ceramic sample sintered by SPS at 900°C for 5 minutes (c) $CoFe_2O_4$ ceramic sample sintered by normal sintering at 1200°C for 2 hours.

1T. The saturation magnetization increased by increasing the particle size as shown in **Table (3.5)**. For the mico-range grains, the saturation magnetization reached to 85 Am^2/kg and decreased for the 40nm particles to about 60 Am^2/kg. Larger remnant magnetization and coercive field were found for the sample sintered by spark plasma sintering. It is known that the coercivity depends mainly on the particles size, the density of the sample and the domain mobility. However the squareness is the remaining magnetism left in the particles when subjected to a magnetic field. The squareness 0.3 (M_r/M_s) value was calculated to the spark plasma sample and very low value for the 40nm superparamagnetic $CoFe_2O_4$ particles with a squareness 0.033.

4. SYNTHESIS AND CHARACTERIZATION OF $CoFe_2O_4$-$BaTiO_3$ NANOPOWDER

In the previous chapter I discussed the synthesis and the magnetic properties of pure coabalt ferrite. In the following chapter I discuss the synthesis of core shell cobalt ferrite-barium titanate magnetoelectric nanoparticles as well as their structural and magnetic properties. In this chapter the method of synthesis (organosol) will be discribed in detail. All the powder in this chaper was synthesized by myself in our group in Essen campus. The morphology for different powders was scanned with cooperation of M.Sc. Yanling Gao. Mössbauer and magnetic properties were measured with cooperation of M.Sc. Soma Salamon and Dipl.-Phys. Joachim Landers in the faculty of physics in Duisburg campus.

4.1 Introduction

Nanoparticles and nanocomposites are promising nowadays in many fields related to new technological instruments such as magnetoelectric sensors, magnetoelectric random access memory (MERAM), energy harvesters, and even in medicine for brain stimulation [146, 147]. In order to fabricate reliable nano-particles and nano-composites, precise synthesis methods are needed. Different techniques have been already used for synthesizing these nanoparticles and nanocomposites. The majority of these methods use the technique of *bottom-up* synthesis. This method consists of obtaining final structured materials by starting to arrange atoms, molecules, or even clusters. This approach includes aerosol (for the gas phase), sol-gel precipitation, and hydrothermal

(for the liquid phase) methods. On the other hand, the *top-down* approach starts from a bulk material and uses milling, cutting, etching or grinding to crush the structure until reaching the micro-nano level or to the desired size. The bottom-up approach is known to have more precise results specially in controlling the final particle sizes and the quality of the particles. In this dissertation, the synthesis procedures utilized the bottom-up approach. Nanoparticles with a core shell structure cannot be synthesized by top-down methods. Different bottom-up methods have been used to fabricate the core shell structure including wet chemical methods [101], sol gel [104, 108] and hydrothermal methods with an annealing process [148]. In this chapter, I report on precise procedures for synthesizing $CoFe_2O_4$-$BaTiO_3$ core shell structures, utilizing the bottom-up approach based on the organsol technique. This method was developed by Yanling Gao during barium titanate synthesis. Advantages of this method include ability to control the constituents weight percentages, and microstructure, ability to produce pure materials and control the reaction kinetics because of the relatively low synthesizing temperatures.

4.2 Synthesizing $CoFe_2O_4$-$BaTiO_3$ core shell structure nanoparticles

The synthesis procedure of nanoparticles with core shell structure is shown in **Figure (4.1)**. I used a combination of the precipitation method with the organosol route. The first synthesis step is the fabrication of $CoFe_2O_4$ nanoparticles which was described in detail in **Section (3.2)**. As I illustrated there, the synthesized powder was gently ground and weighed in order to be used in the next step of composite nanopowder synthesis.

To achieve the core shell structure, two main processes were used. The first process was preparation of stable $CoFe_2O_4$ nanoparticles in toluene (ferrofluid). This was done using oleic acid and oleyamine, which are widely used as dispersing nonpolar agents. The second step was to add this ferrofluid into

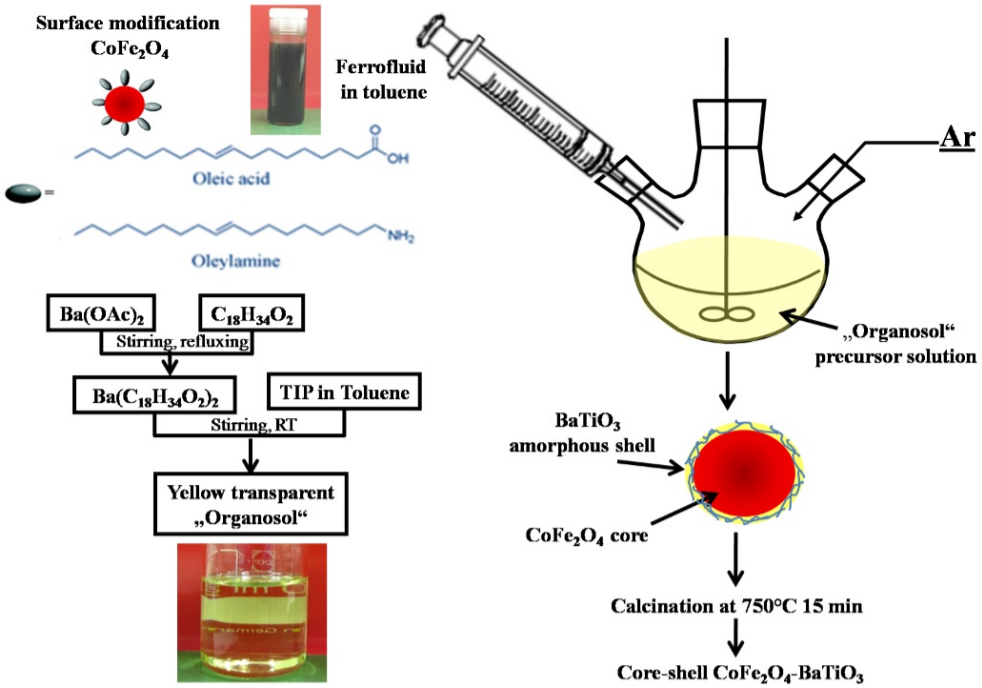

Fig. 4.1: Organosol synthesizing route for fabricating $CoFe_2O_4/BaTiO_3$ core/shell structure [149].

a barium titante organsol solution [150] in order to form a bi-phasic precursor containing crystalline $CoFe_2O_4$ nanoparticles dispersed in amouphous $BaTiO_3$ solution. In more details, the $CoFe_2O_4$ nanoparticles which was previously produced are added at room temperature to toluene (Sigma Aldrich, Andydrous 99.8%). The suspension of $CoFe_2O_4$ in toluene was heated to 80°C under magnetic stirring. After that, oleyamine $C_{18}H_{37}N$ (Sigma-Aldrich, 70% technical grade) and oleic acid $C_{18}H_{34}O_{24}$ (Sigma-Aldrich, 90% technical grade) were added to the suspension in a 30% weight amount for both in comparison to the amount of toluene. The suspension then was magnetically stirred for 30 minutes and then milled using milling balls with different diameters for 12 hours. This process was done by a rotation machine which can make the particles finer, and can reduce the agglomeration of the particles. The suspension was introduced to the centrifugation process (r=10cm) with a speed of 7000 rpm in order to separate the ferrofluid and remove the excess of toluene, oleyamine, and oleic acid. The non modified particles were finally removed by

washing the final suspension several times with water, ethanol, and toluene, and then suspended again in toluene forming a stable ferrofluid as shown in **Figure (4.1)**. The modification of the $CoFe_2O_4$ surface is the main step in forming the core shell structure. Hydrophobic $CoFe_2O_4$ is achieved via fatty acid adsorption.

To prepare barium titanate organosol solution, barium acetate $Ba(C_2H_3O_2)_2$ (Sigma Aldrich) was mixed with titanium(IV)n-isopropoxide $Ti(C_{12}H_{28}O_4)$ (Sigma Aldrich, reagent grade 97%) in oleic acid $C_{18}H_{34}O_2$ (Sigma-Aldrich, 90% technical grade) under argon atmosphere. A yellow precursor solution, the "Organosol" was formed. Preheating of barium acetate in oleic acid was done in order to completely dissolve the amount of barium acetate. The ferrofluid -which was synthesized previously- was added to the precursor at room temperature. The weight percent of the ferrofluid was controlled by weighing the amount of $CoFe_2O_4$ before forming the ferrofluid, which was calculated with respect to the amount of $BaTiO_3$ formed by the organosol method. At temperature of 90°C, an adequate amount of tetramethylammonium hydroxide TMAH ($C_4H_{13}NO$) (Sigma Aldrich, 25%wt in methanol) was added in four batches in order to form the gel slowly. The black gel was removed and dried in a normal oven at 80°C for a half day. To obtain the core shell powders, the dried gel was directly calcined at 750°C for only 15 minutes then cooled down to room temperature and then gently ground by a hand grinding tool. Some amount of barium carbonate appearing in the structure was removed by washing the powders by 0.2 mol of acetic acid which can easily dissolve the impurities. Samples of pure $BaTiO_3$ powder were synthesized just by forming the gel without adding $CoFe_2O_4$ ferrofluid. To perform dielectric measurments, some samples were prepared by pressing the obtained powder into discs, painted by two silver electrodes and then covered by epoxy in order to stabilize the sample.

4.3 Structural characterization of $CoFe_2O_4/BaTiO_3$ core shell structure

Figure (4.2) shows x-ray diffraction patterns at room temperature for the samples containing different weight percents of $BaTiO_3$. Comparing to the standard data files [139] for both cobalt ferrite and barium titanate, all of the phases existed without any undesirable phases. The width of the peaks shown in **Figure (4.2)** is evidence of the nanosize of all of the powder. The peak intensities of barium titanate increase by increasing the weight percent of barium titanate, the maximum intensities were observed for the compositions, x=1 and x=0.8. A few intensities of $CoFe_2O_4$ planes are observed comparing to the $BaTiO_3$ intensities especially in the composite with higher amount of barium titanate, as expected. The x-ray measurements were used in order to estimate the lattice parameter for each composition as shown in **Table (4.1)**. However, the absence of peak splitting e.g in the planes [002][200] or [103][301] is an indication of the cubic structure of barium titanate for different compositions [151]. The lattice parameters were in the range of 3.97-4.027Å, which are typical values of bulk barium titanate [35].

Tab. 4.1: Unit cell parameter of $BaTiO_3$ for different compositions of (1-x)$CoFe_2O_4$-x$BaTiO_3$ nanopowder

Sample	a(Å)
x=1	4.011±0.011
x=0.8	3.991±0.021
x=0.7	4.005±0.015
x=0.6	4.013±0.014
x=0.5	3.997±0.018

Figure (4.3) shows the analysis of the sample morphology using scanning electron microscopy. The calcinated powder of cobalt iron oxide particles is shown in **Figure (4.3.a)**. The spherical shaped particles are slightly separated with a low degree of agglomeration. This enhances the formation of the core shell structure and prevents merging of particles to form bigger cores. $CoFe_2O_4$

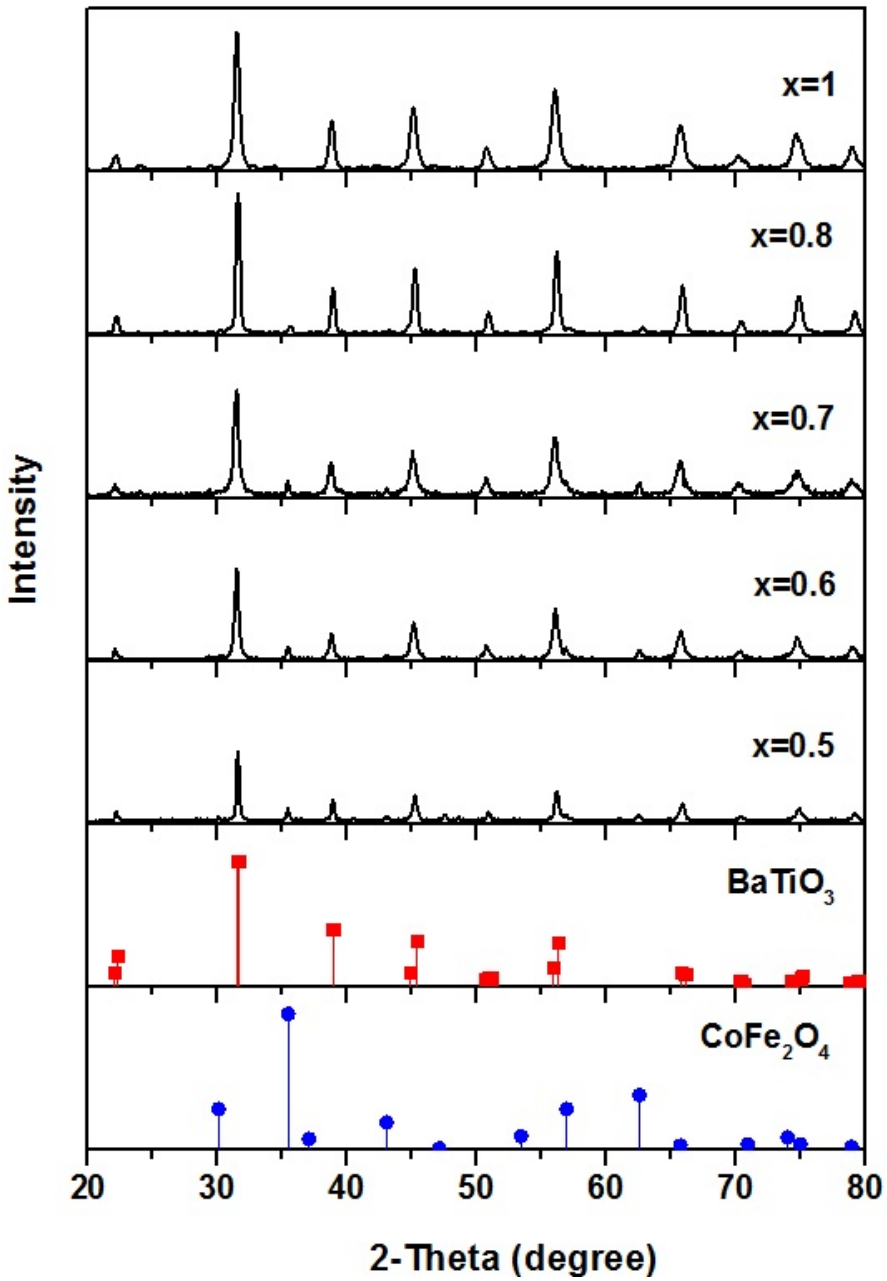

Fig. 4.2: Room temperature x-ray diffractions for the composite nanopowders for different compositions (1-x)$CoFe_2O_4$-x$BaTiO_3$ [x=0.5, 0.6, 0.7, 0.8, 1], all of the powders were calcined at 750°C for 15 minutes and the standard perovskite $BaTiO_3$ and inverse spinel $CoFe_2O_4$ reference peaks were taken from Ref. [139].

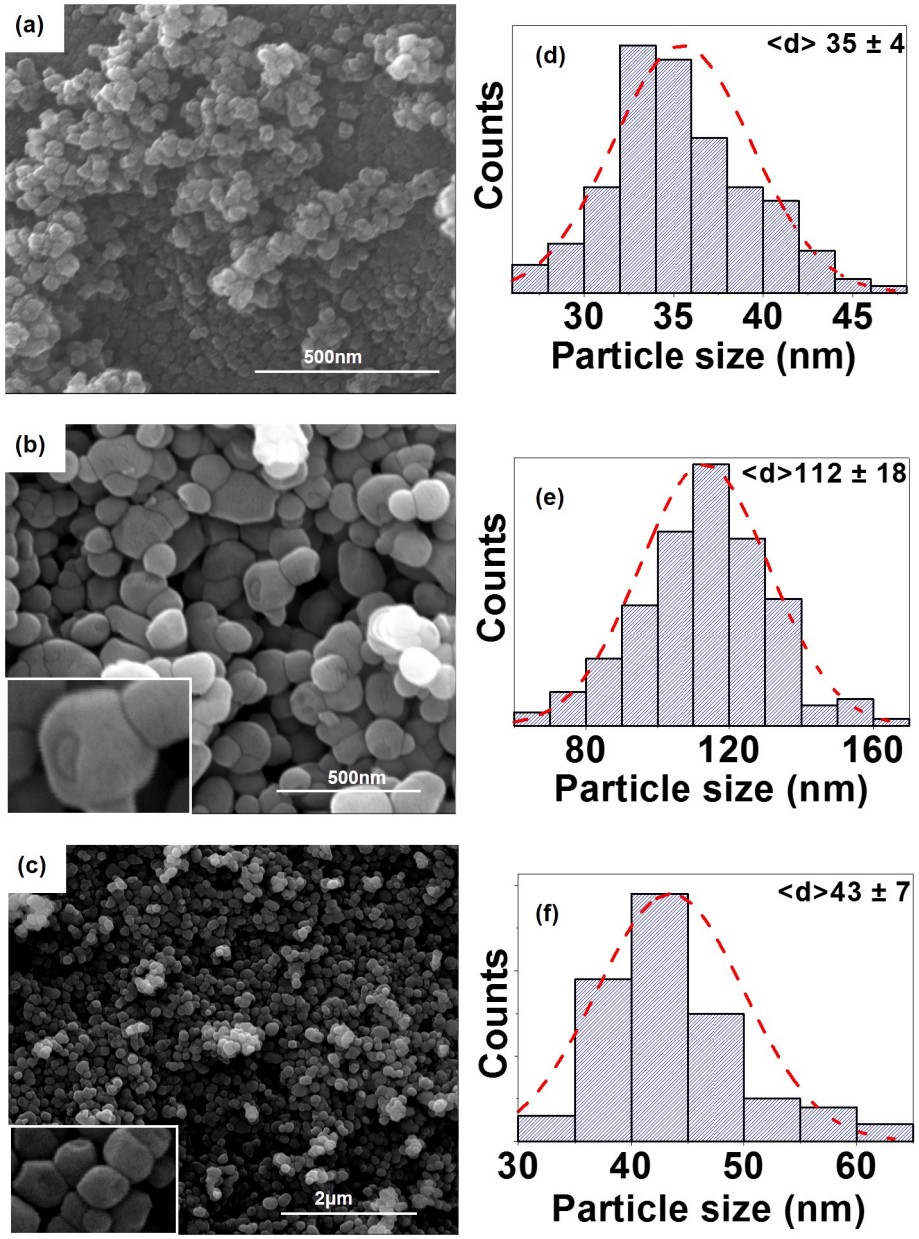

Fig. 4.3: SEM micrographs for (a) $CoFe_2O_4$ nanopowder calcined at 750°C for 15 minutes (b) (1-x)$CoFe_2O_4$-(x)$BaTiO_3$ [x=0.5] core shell nanopowder calcined at 750°C for 15 minutes [the inset shows one core shell particle] (c) (1-x)$CoFe_2O_4$-(x)$BaTiO_3$ [x=0.8] core shell nano-powder calcined at 750°C for 15 minutes [the inset shows one core shell particle] (d) particle size distribution of $CoFe_2O_4$ nano-particles (e) particle size distribution for the core shell nano-particles (f) particles size distribution of the $CoFe_2O_4$ cores [149, 152]

.

nanoparticles are monodispersly distributed in the range of 35±4 nm as shown in the Gaussian distribution in **Figure (4.3.d)**. The analysis of the composite powder **(Figure 4.3.b)** showed very fine particles. The particles are larger, spherical in shape and have a narrow size distribution **Figure (4.3.e)**. The mean size was 112 nm. The inset in the figure shows a magnification of one particle with $BaTiO_3$ shell partially surrounding the $CoFe_2O_4$ core. However, a certain degree of agglomeration could not be avoided. The similar core shell structure was observed for the sample containing 80% $BaTiO_3$ and 20% $CoFe_2O_4$ **(Figure 4.3.c)**. In this sample a lot of $CoFe_2O_4$ core particles were observed which were not completely covered by $BaTiO_3$ shells, so that one can easily estimate the core particle size distribution (**Figure 4.3.f**). The cores distributed around 43 nm which is very close to the starting $CoFe_2O_4$ powder size used in the ferrofluid.

The structure of the composite was also analyzed by TEM. The difference in transmission intensities between $CoFe_2O_4$ and $BaTiO_3$ was clearly seen in **Figures (4.4.b,c,e)**. The interface between the two phases is also clear in the high angular annular dark image field **Figure (4.4.c,e)** for the compositions [x=0.5] and [x=0.8]. For the cores, space in between [200] and [111] planes was measured to be d = 0.430±0.005 nm and 0.481±0.005 nm, respectively. For the shell the spacing between [001] and [011] planes was d = 0.401±0.005 nm and 0.286±0.005 nm, respectively. These values were in good agreement with the spacing that is estimated from the x-ray diffraction data when the core is assigned to $CoFe_2O_4$ and the shell to $BaTiO_3$. For the compositions [x=0.5] and [x=0.8], **Figure (4.4.d)** and **Figure (4.4.e)**, respectively, the EDS analysis revealed that the concentration of the elements Co and Fe had a maximum in the middle of the particle and decreased towards the edges, while Ba and Ti showed the opposite trend. The average shell thickness can be estimated as $\simeq$ 40-50 nm.

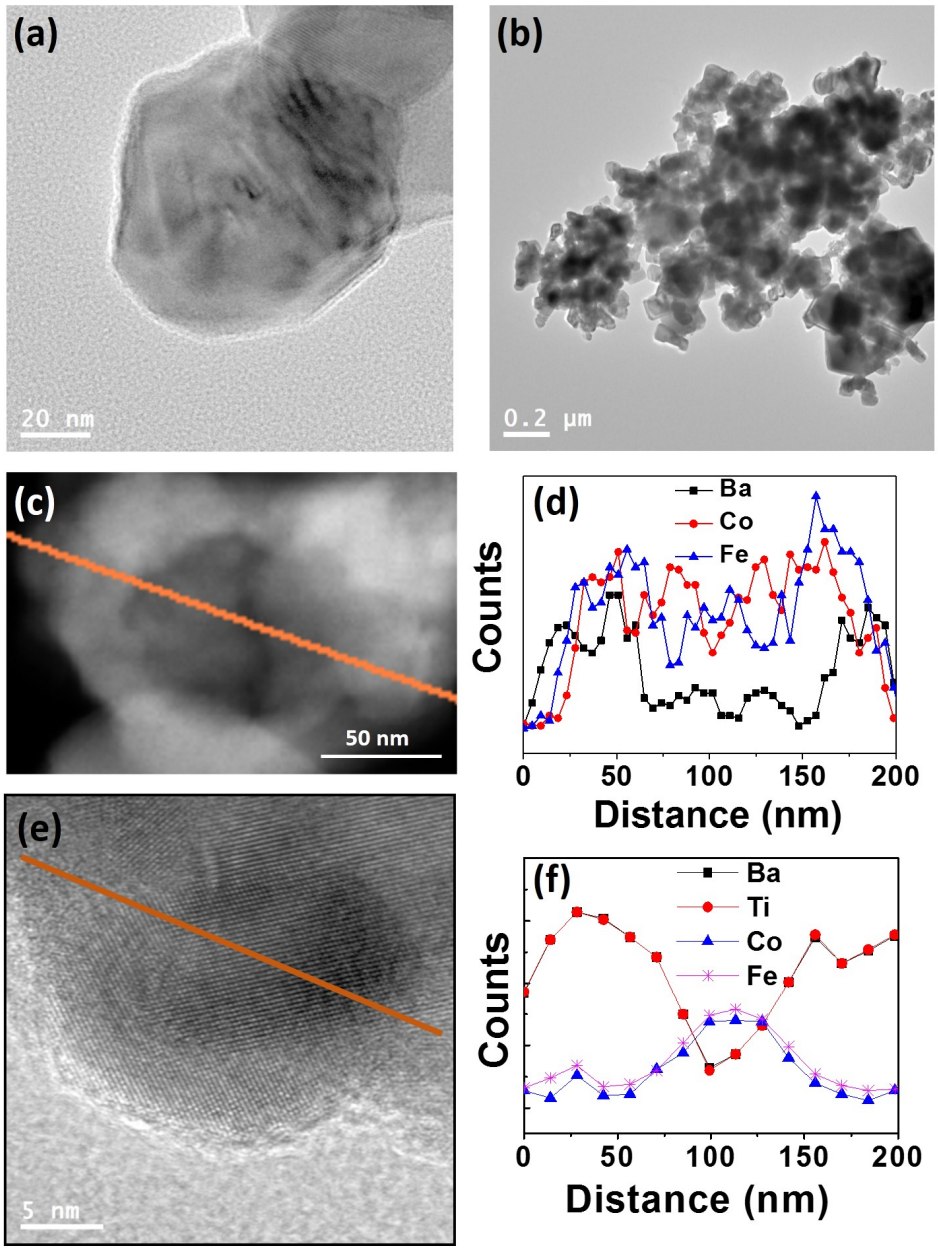

Fig. 4.4: TEM images of (a) single particle of cobalt iron oxide synthesized by the co-precipitation method (b) (1-x)$CoFe_2O_4$-(x)$BaTiO_3$ [x=0.5] core shell structure nanoparticles (c) HAADF-STEM image of a single particle a core shell (1-x)$CoFe_2O_4$-(x)$BaTiO_3$ [x=0.5] composite powder, the line shows the scanned EDS path done (d) distribution of the elements Ba, Co, Fe across the (1-x)$CoFe_2O_4$-(x)$BaTiO_3$ [x=0.5] single core shell particle based on the EDS line scan (e) HAADF-STEM image of a single particle a core shell (1-x)$CoFe_2O_4$-(x)$BaTiO_3$ [x=0.8] (f) distribution of the elements Ba, Co, Fe across the (1-x)$CoFe_2O_4$-x$BaTiO_3$ [x=0.8] single core shell particle based on the EDS line scan [image by Anna Elsukova] [149].

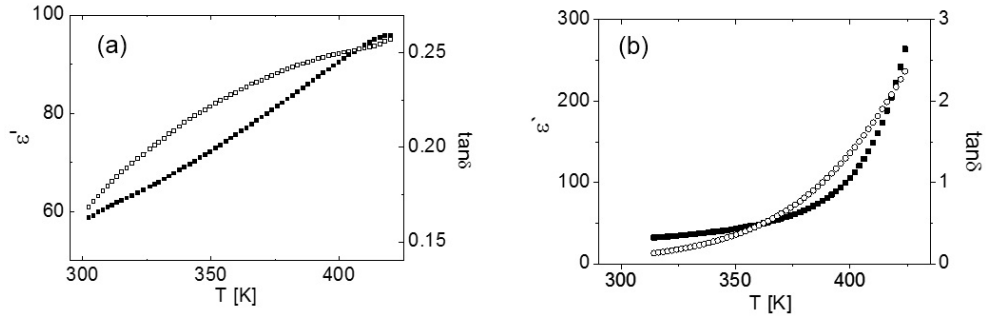

Fig. 4.5: Dielectric permittivity (solid symbols) versus temperature for barium titanate cobalt ferrite core shell structure and loss tangent (open symbols) measured at f=10kHz for compositions (a) x=0.5 (b) x=0.8.

4.4 Dielectric properties of $CoFe_2O_4/BaTiO_3$ core shell structure nanoparticles

The measurement of dielectric permittivity done for the nanopowders is shown in **Figure (4.5)**. For both composition (x=0.5 and x=0.8), the permittivity and the dielectric loss increase by increasing the temperature in the temperature range interval (300-450K). This is related to contribution of the charges accumulated at the cobalt ferrite barium titanate interface which is related to the Maxwell-Wagner relaxation type (**see Section (2.7)**). This charge acculation affects the real values of permittivity. More core shell particles increase the charge accumulation at the interface and hence enhance the permittivity values. Surprisingly, the sample with less cobalt ferrite (**Figure (4.5.b)**) showed higher loss values which may attributed to the porosity. It should be mentioned here that the nanopowders were pressed and molded in epoxy. This non-sintered pressed powder has low density values due to the voids between the particles and hence higher porosity which reduces the permittivity values and increases the losses which are obvious in **Figure (4.5)**.

Barium titanate has the ferroelectric phase transition at temperature 393K [33]. However, the permittivity of the nanopowder did not show any anomaly at this temperature. This can be due to the fact that the barium titanate is in the paraelectric rather than in the ferroelectric state. This is compatible

with the x-ray diffraction results shown previously, where the tetragonality for all samples was not detected by peak splitting as described before. It was reported before that the tetragonality of the barium titanate increased by increasing the particles sizes and decreases for small particle sizes [153].

4.5 Mössbauer spectroscopy of $CoFe_2O_4/BaTiO_3$ core shell nanoparticles.

Mössbauer spectroscopy analysis was done to the core shell nano-powder in order to study the magnetic structure and the chemical environment. The results are shown in in **Figure (4.6)**. The spectrum consists of two sub-spectra, the first is the sextet which corresponds to Fe^{+3} on tetrahedral A-sites (line A), and the second is the distribution of hyperfine fields for Fe^{+3} in octahedral sites (line B). By comparison between the areas of the A and B lines, the inversion parameter s can be calculated using **Equation (3.2)**. From our measurements the calculations yield the inversion parameter of s=0.7±0.02 . This value corresponds to the stoichiometry $[Co^{+2}{}_{0.3}Fe^{+3}{}_{0.7}]_A[Co^{+2}{}_{0.7}Fe^{+3}{}_{1.3}]_BO_4$. This stoichiometry and the inversion parameter agree with data e.g for pure cobalt iron oxide synthesized by sol-gel autocombustion [154], but are different from the pure cobalt ferrite value s=0.9 reported in **Section 3.4**. This difference may be related to the existence of barium titante in the composite powder or the difference in cobalt ferrite particle sizes. However, the annealing temperature which was 750°C may lead to misplacements of Co^{+2}, this misplacements results in a reduction of the hyperfine magnetic field due to the ensemble of B-sites with various numbers of next iron neighbours.

The angle between the applied magnetic field and the magnetic moment of the particles is defined as the spin canting angle θ . This angle was calculated from the ratio of the spectral areas of the second and the third line of both sextet subspectra. The value of θ was estimated to be 20^o for the A-site and 31^o for the B-site. Same values were obtained for pure cobalt iron oxide

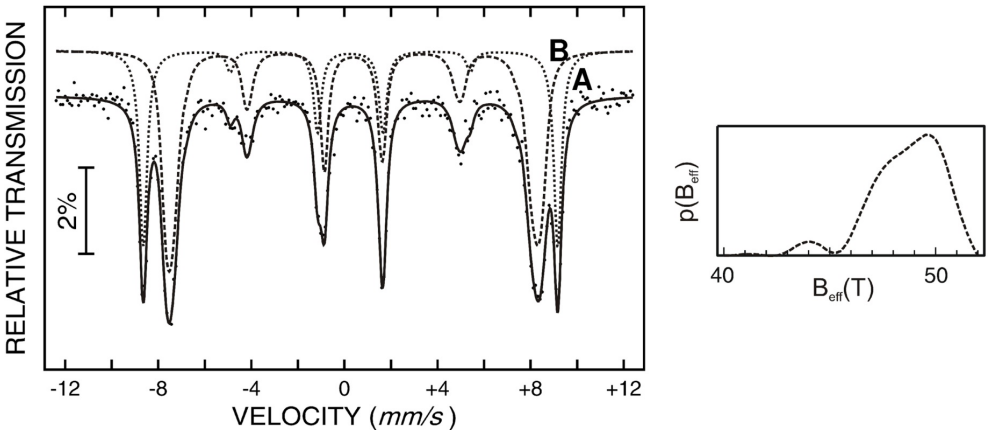

Fig. 4.6: Mössbauer spectrum for (1-x)$CoFe_2O_4$-x$BaTiO_3$ [x=0.5] core shell structure nanoparticle at 4.2 K with the applied magnetic field 5T along the transmission of γ- rays. The dotted sextet represents the subspectra for Fe^{+3} in tetrahedral and the dashed line corresponds to the octahedral surroundings [149].

nanoparticles [155]. For magnetic nanoparticles it is known that the spin canting is more pronounced on the octahedral B-Sites.

Tab. 4.2: Mössbauer parameters: isomer shift δ relative to α-Fe at room temperature, quadrupole splitting Δ, relative spectral area A, calculated hyperfine magnetic field B_{hf}, and spin canting angle θ, for the composite (1-x)$CoFe_2O_4$-(x)$BaTiO_3$ [x=0.5] nanopowder measured at 5 K with B=5 T [149].

	δ(mm/s)	Δ(mm/s)	Area (%)	B_{hf}(T)	$\theta[^o]$
A-site	0.36(1)	0.01(1)	35(1)	50.52(5)	20(1)
B-site	0.48(1)	0.00(1)	65(2)	52.94(6)	31(1)

The values of the hyperfine field were calculated from the equation:

$$B_{hf} \approx B_{eff} \pm B_{appl} \cos\theta \tag{4.1}$$

Where B_{eff} is the observed effective hyperfine field, B_{appl} is the applied field. The positive and negative sign is related to the octahedral and tetrahedral sites. All of the Mössbauer parameters are shown in **Table (4.2)**. All of the parameters are in agreement with pure cobalt iron oxide nanoparticles reported in **Chapter 3**.

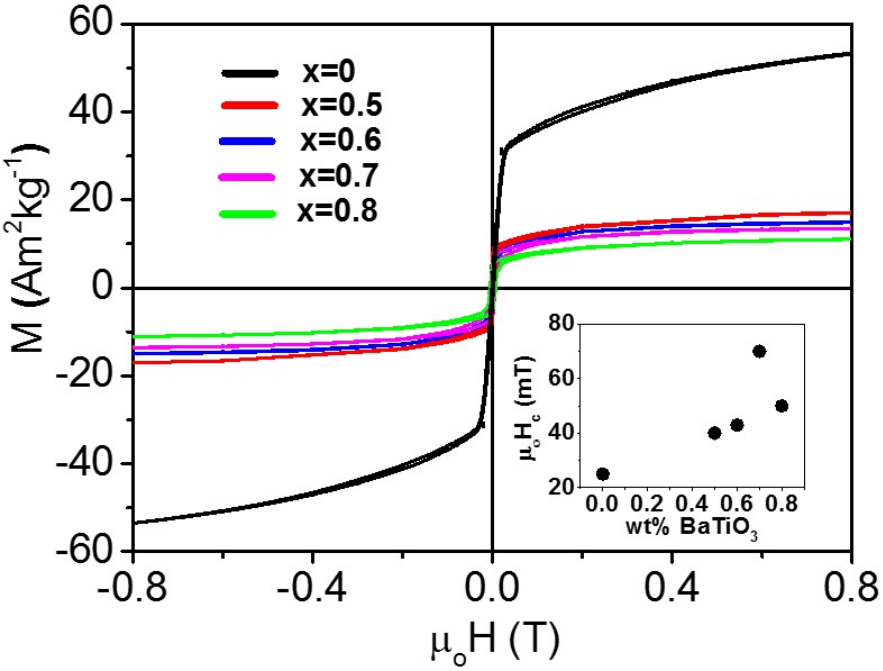

Fig. 4.7: (a) Room temperature magnetization hysteresis loops for (1-x)$CoFe_2O_4$-x$BaTiO_3$ calcined nanopowder for different compositions, the inset shows the dependence of coercive field on the barium titanate weight percent.

4.6 Magnetic properties of $CoFe_2O_4$-$BaTiO_3$ core shell structure

The magnetic properties of different compositions are shown in **Figure 4.7**. The pure cobalt ferrite nanoparticles showed larger saturation which reached about 55 Am^2/kg. The saturation magnetization for other compositions was less than 20 Am^2/kg. The decrease of saturation magnetization can be related to a lower content of cobalt ferrite in the composites, because the measured magnetic moments are divided by the mass of the total powder weight. More cobalt ferrite results in more magnetic moments and hence more magnetization.

For different compositions, the larger amount of diamagnetic $BaTiO_3$ decreases the total magnetization. It was also found that more content of barium titanate slightly increases the coercive field, see **Table (4.3)** and the inset in **Figure (4.7)**. We suggest that more content of barium titanate may impede

the movement of magnetic domains and then a larger magnetic field is needed to switch the magnetic moment. This behavior is also shown in remnant magnetization values where more barium titanate shells surrounding the cobalt ferrite cores may stabilize residual magnetization. However, all of the magnetic properties of $CoFe_2O_4$-$BaTiO_3$ nanoparticles are different from those of pure bulk $CoFe_2O_4$ or even $CoFe_2O_4$-$BaTiO_3$ ceramic samples.

Tab. 4.3: Room temperature dielectric and magnetic properties for the different calcined nanopowder samples

x	M_s (Am^2/kg)	M_r (Am^2/kg)	H_c (kA/m)	M_r/M_s
0	55	2	25	0.036
0.5	18	5.5	40	0.31
0.6	15.5	5.75	43	0.37
0.7	14	6	70	0.43
0.8	11.5	4.6	50	0.4

The increasing amount of $CoFe_2O_4$ in the nanopowder decrease the values of squareness. The smallest value of squareness 0.036 was recorded for the pure sample of $CoFe_2O_4$ nanopowder while it distributed from 0.3-0.43 for the other compositions. In the following two chapters, the composite powders with different compostions were sintered and converted into ceramic using normal sintering method and spark plasma sintering. The multiferroic properties, electrical characteristics, microstructures and magnetoelectric characteristics will be also discussed.

5. FORMATION OF (0-3) AND (3-0) $CoFe_2O_4$- $BaTiO_3$ CERAMICS

After describing the core shell nanopowder properties in **Chapter 4**, I will discuss the sintering routes in order to form barium titanate cobalt ferrite ceramic composites with (0-3) and (3-0) connectivity. In the following chapter, electrical, magnetic, and structural properties of composites for different connectivity schemes will be described here. The ceramic samples were normally sintered by myself in our group in Essen campus. The spark plasma samples were sintered by Dr. Devendraprakash Gautam from the group of professor Winter of the Department of Engineering Sciences in Duisburg campus. The morphology for different powders was scanned with cooperation of M.Sc. Yanling Gao. PFM and MFM scans were done with cooperation of M.Sc. Harsh Trivedi and the magnetic properties were measured with cooperation of M.Sc. Soma Salamon and Dipl.-Phys. Joachim Landers in the faculty of physics in Duisburg campus.

5.1 Introduction

Among different types of connectivity, the (0-3) connectivity is of high interest due to the magnificent properties resulting from combining ferroelectric and ferromagnetic, which were also described in **Section (1.12)**. The system cobalt ferrite-barium titanate ceramic has the advantage that controllable synthesis routes can produce different connectivities. The system exhibits spinodal decomposition that prevents a reaction between the perovskite ferroelectric and the spinel ferrimagnetic phases. This causes segregation of the two

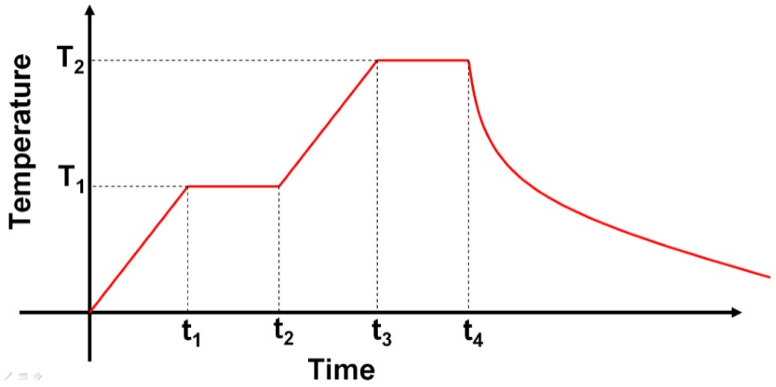

Fig. 5.1: Normal sintering process showing holding times and temperatures

phases which facilitates the processing. In this chapter the sintering routes, phases, morphology magnetic and ferroelectric properties for the (0-3) and (3-0) composites will be discussed.

5.2 Sintering routes

Sintering is a heat treatment process for a powder or a compacted powder, which is usually done below the melting point of the material, in order to increase the strength and merging or fusing the particles together. Depending on the type of ceramic produced, the way of sintering is very important where the mechanical strength, conductivity, density, and porosity can be controlled by the sintering process. The most important factors in the densification process are, pressure, temperature, time, and the atmosphere used. The easiest method for obtaining ceramics is to start from nanoparticles and sintering them to a limited grain growth. These nanopowders have large surface areas that provide a strong driving force for sintering. The sintering process (see **Figure (5.1)**) begins with heating the green bodies from room temperature to a specific temperature (T_1) in period (t_1) and then holding at this temperature for a certain time (t_2-t_1), then rising the temperature to the desired temperature (T_2) and holding the sample for another period of time (t_4-t_3) and then cooling down to room temperature.

In this work all samples were annealed first at a temperature T_1=750°C,

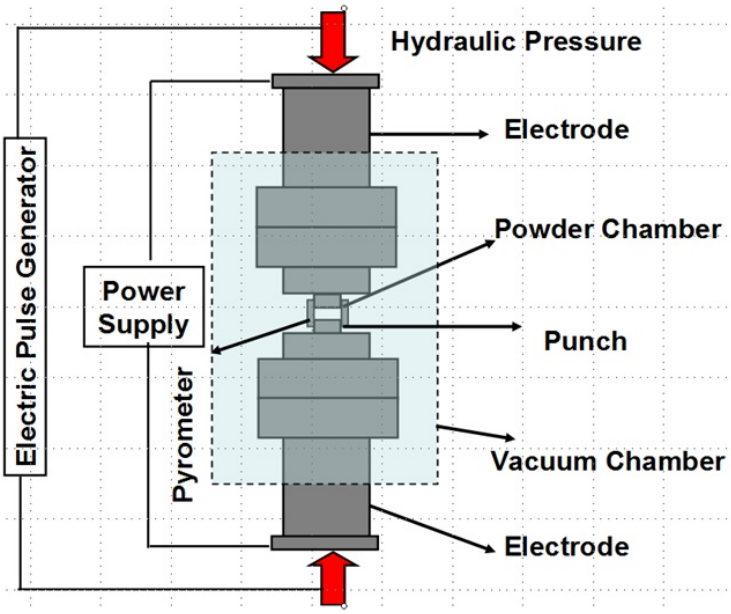

Fig. 5.2: Schematic drawing showing the SPS method.

the rate of heating 6°C/minutes up to T_1 with the holding time 2 hours. Annealing removes all undesired materials, the organic substance like oleic acid or oleyamine which may have stayed in the material. The temperature then is raised to 1200°C at a rate of 6°C/min. At 1200°C as the sintering temperature, the holding time was 2 hours. The samples were cooled down to room temperature normally at a rate of about 2.5°C/min. It is important to point out that there should not be any chemical reaction between the constituents at higher temperature so that it does not affect the structures and the piezoelectric and the piezomagnetic properties of the composite.

Another method of sintering is the spark plasma sintering (SPS) which is explained in **Figure (5.2)**. In this method a pressure and an electric current are applied to the sample simultaneously using a hydraulic press and an electric pulse generator, respectively. A very strong current results in Joule heating causing a high heating rate in a short time promoting densification. In SPS a powder is introduced into a die which is usually built up from such materials as carbon, tungsten carbide, or hard alloys. Rather than the conventional sintering method, the SPS process decreases the solidification time from hours

to minutes. This can suppress grain growth by reducing the diffusion at phase boundaries and hence provide dense nanocrystalline materials. The details about the SPS procedure used here are explained as follows: The powder was introduced into a SPS machine (FCT HP D5, FCT Systeme GmbH, Raunstein, Germany) and loaded into a graphite die with 20mm in inner diameter, 45mm in outer diameter, and 50 mm in height. To prevent the contact between the powder and the surface of the die, a boron nitride coated graphite foil was used, this also ensure that the current flows through the sample and not through the die during the sintering process. A graphit wool was used in order to cover the graphite die preventing heat losses. A pulsed electric current was used in order to heat the sample from room temperature to 1000°C with a heating rate 100°C/min and holding time 5 minutes. The sample was cooled down to 500°C with rate 100°C/min and further to room temperature by natural cooling. In this heating-cooling cycle, an uniaxial pressure of 35 MPa was applied to the sample. The temperature was controlled using an optical pyrometer focused on the surface of the upper graphite push-punch. The complete sintering process was performed in vacuum with a pressure of about 1 mbar. Polishing was performed to the samples in order to remove the graphite foil from the surface. Some samples were annealed after SPS process at 900°C for 2 hours using a normal furnace (Nabertherm).

5.3 The (0-3) connectivity type in $CoFe_2O_4$-$BaTiO_3$ ceramics

Different types of connectivity found in ceramic technology were discussed in **Chapter 1**. The type of connectivity has a great influence on general physical properties of composites and the ME effect because it decides the degree and way of contact between the two phases. The particulate composite contains one phase such as ferromagnetic materials embedded in another phase e.g. a ferroelectric matrix. It is important when checking the connectivity to look at the composite on three directions: surface and both sides, e.g. in

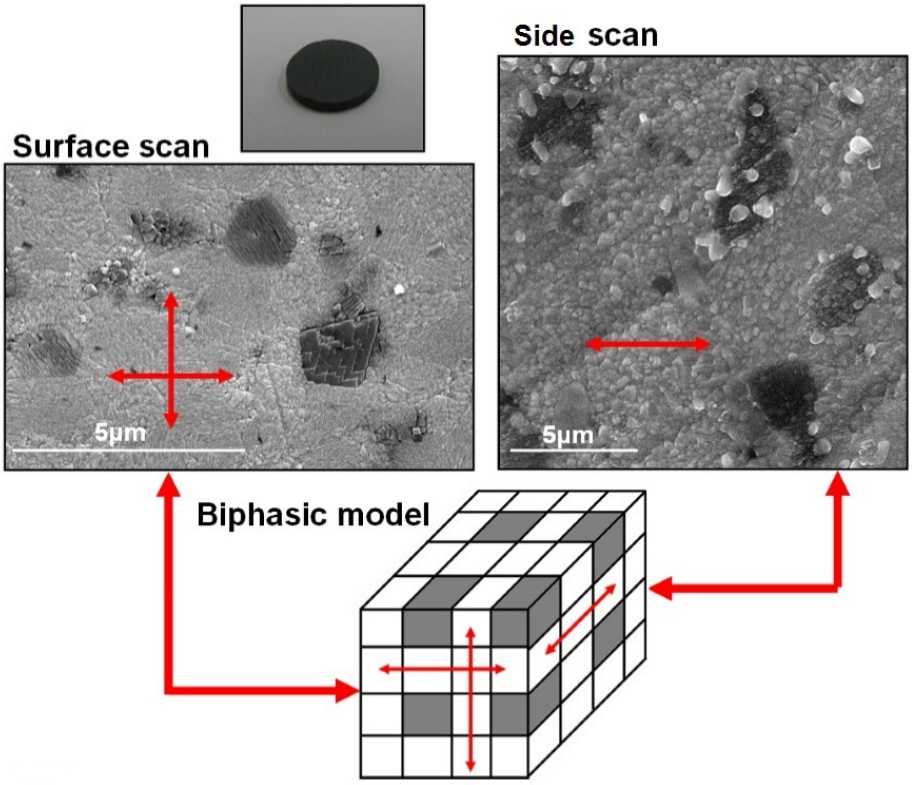

Fig. 5.3: (0-3) connectivity showing SEM photo for the (1-x)$CoFe_2O_4$-x$BaTiO_3$ [x=0.8] ceramic with side and surface scan, and the corresponding ideal biphasic model.

order to investigate how the material is structured. This can be done using scanning electron microscopy. The results of the SEM scans for the sample with composition of x=0.8 are shown in **Figure (5.3)**.

Dark cobalt ferrite regions on the surface are distributed in the matrix of barium titanate. The magnetic regions are not connected to each other and separated in vertical or horizontal way in comparison with the biphasic ideal model shown in the figure. This explains the first number of the composite connectivity definitions (0) which is usually used to represent the ferromagnetic component in the ME composites. The same distribution of magnetic regions also appeared in the SEM scan for the side of the sample. This proves the (0-3) nature of the composite where the regions of cobalt ferrite are totally separated from each other in 3 dimensions and embedded in the barium titanate matrix. The matrix means that the barium titanate regions are con-

tinuously connected together in all directions forming a 3 connectivity. The (0-3) connectivity was formed here using normal sintering and due to the spinodal decomposition of the system, which prevents mixing of the constituents at high sintering temperature.

5.4 Structural analysis of the (0-3) $CoFe_2O_4$-$BaTiO_3$ ceramics

The phase content for different compositions was characterized using XRD as shown in **Figure (5.4)**. The measurements confirmed the existence of tetragonal perovskite barium titanate and cubic spinel cobalt ferrite phases.

The diffraction patterns were compared and matched with the known data files (22-1086)(blue circle symbols) in **Figure (5.4)** for the cobalt ferrite and (05-0626)(red square symbols) for the barium titanate [139]. No other interference phases were detected after the sintering process. The peaks were not broad in comparison to there in a nanopowder, this indicates increasing crystallite size after sintering. The intensity of the barium titanate peaks increased and the highest intensity was recorded for the compositions of x=0.8 and 0.7. The intensity of the most pronounced peaks for the cobalt ferrite was weak for the composition of x=0.8, but pronounced for the compositions of x=0.5 and x=0.6. As indicated in **Figure (5.5)**, splits of the diffraction peaks are clear for the following planes which correspond to the Miller indexes *(hkl)* and the diffraction angles 2θ: (101) (110) at ($2\theta \simeq 31^\circ$), (002)(200) ($2\theta \simeq 45^\circ$), (112)(211) ($2\theta \simeq 56^\circ$), (202)(220) ($2\theta \simeq 66^\circ$), (103)(301) ($2\theta \simeq 75^\circ$). It is well known that the splitting of barium titante XRD peaks is an indication of tetragonality [151]. In order to have a magnetoelectric effect for composites at room temperature, proving the ferroelectricity of the piezoelectric phase like barium titanate is an important issue.

For the powder, from **Figure (5.5.b)**, peak splitting is absent (**Figures (5.5.c)** and **(5.5.d)**), this indicates a cubic structure of the barium titanate with 120 nm particle size, see **Chapter 4**. It was shown before that barium

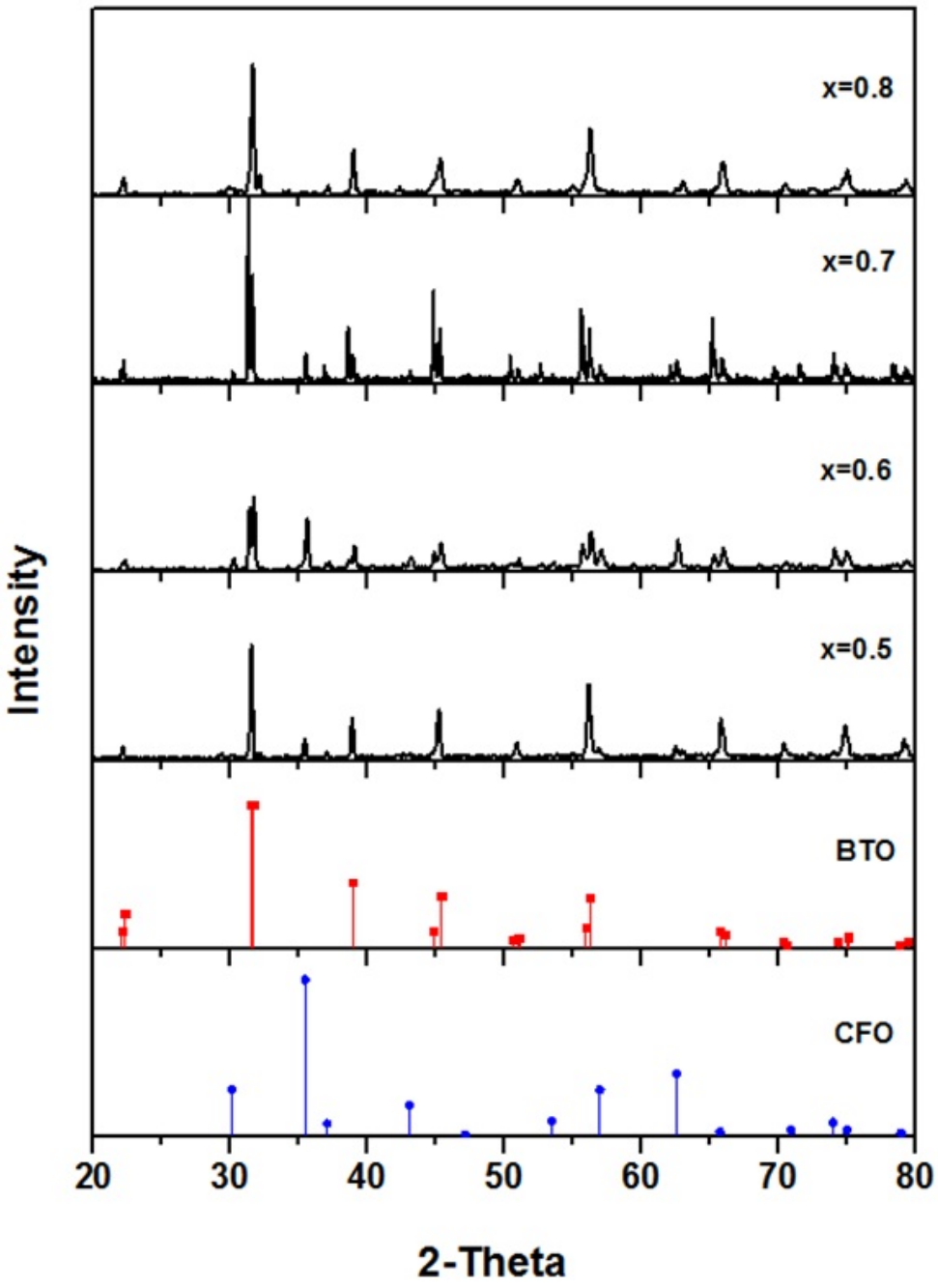

Fig. 5.4: XRD for different sintered ceramic compositions of (1-x)$CoFe_2O_4$-x$BaTiO_3$ samples.

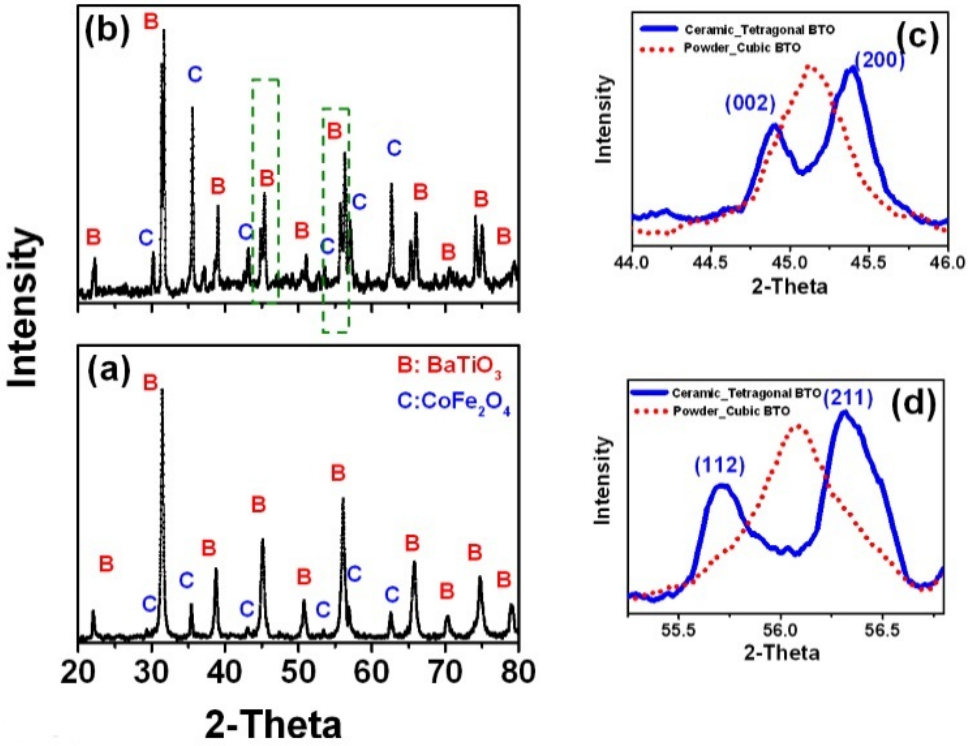

Fig. 5.5: Example of tetragonality of $BaTiO_3$, XRD for different compositions of (1-x)$CoFe_2O_4$-x$BaTiO_3$ at x=0.6 (a) powder (b) ceramic (c) splitting peaks [002] and [200] (d) splitting peaks [112] and [211].

titanate with 120nm particle size has a cubic structure or the tetragonality of the barium titanate is very low so that the peaks splitting does not appear in the XRD [156]. Thus, we have a structure change from cubic in powder $BaTiO_3$ to tetragonal in the ceramic form.

5.5 Morphology, SEM, TEM, and EDS analysis of the (0-3) composite

SEM scans were performed on the polished sample surfaces and shown in **Figure (5.6)**. Well defined magnetic and ferroelectric phases were detected. The dark contrasts represent the cobalt iron oxide regions and the bright represent the barium titanate. The difference in darkness is due to the electronic work functions of the two phases which causes different reflectivity. The regions of cobalt ferrite were observed to be separated from each other and immersed in the matrix of barium titanate. This separation represents the zero connectivity scheme. These magnetic regions distributed in the range of size of 2-4μm. The cubic nature of the spinel cobalt ferrite is also reflected in the apparent grain shapes. In case of the composite with composition x=0.5, the magnetic regions are closer to each other while in the case of x=0.8 the magnetic regions are distributed in large distances. This is related to different weight fractions for different compositions.

One $CoFe_2O_4$ region immersed in a $BaTiO_3$ matrix is shown in **Figure (5.7.a)**. A well-defined interface between the two phases is shown in **Figure (5.7.b)**. The two phases have direct contact to each other without any cracks or pores in the borders. It is well known that the well-defined interfaces between the biphasic phases is important for generating ME effect. The direct contact at the interface provides stronger interaction between the phases and hence a larger ME effect.

Energy dispersive spectroscopy confirmed the formation of $BaTiO_3$ and $CoFe_2O_4$ by elemental analysis shown in **Figures (5.7.c)** and **(5.7.d)**. Vari-

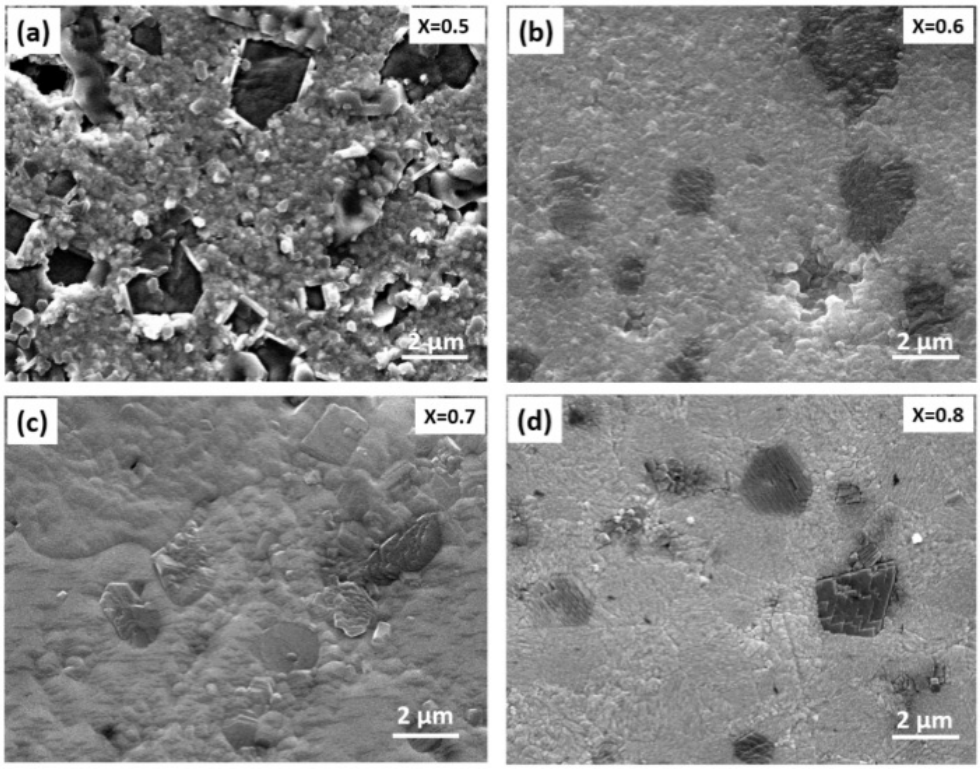

Fig. 5.6: Surface SEM scan photos for the etched and polished ceramic samples (1-x)$CoFe_2O_4$-x$BaTiO_3$ (a) x=0.5 (b) x=0.6 (c) x=0.7 (d) x=0.8.

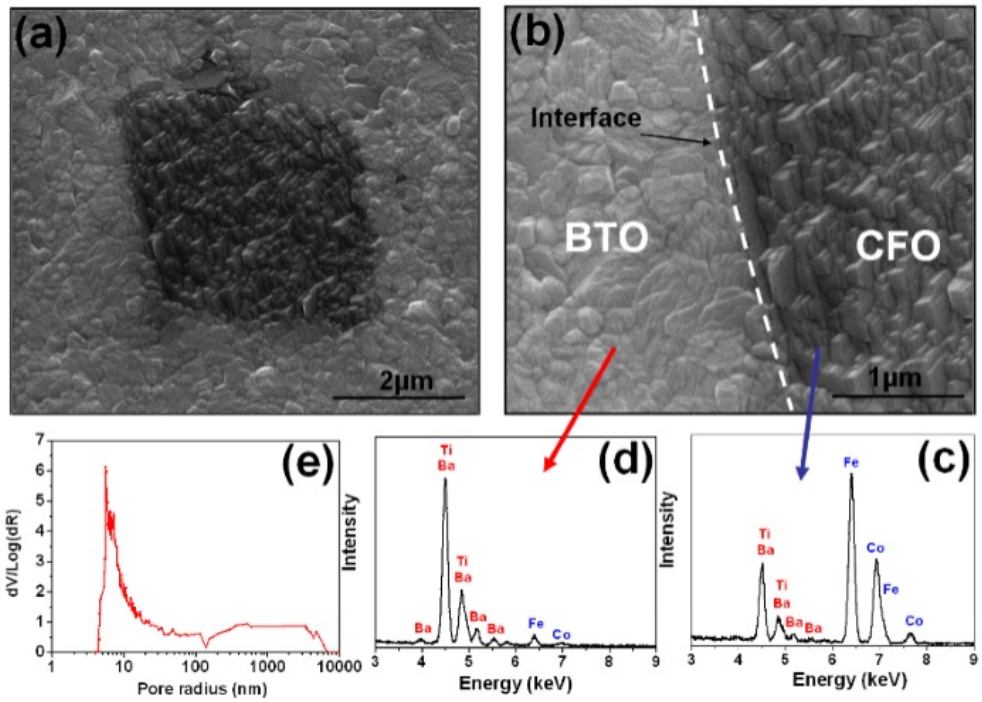

Fig. 5.7: (a) SEM photo for sintered, polished, and thermally etched surface for the sample (1-x)$CoFe_2O_4$-x$BaTiO_3$ at x=0.6 (b) SEM photo showing the interface between the two phases (c) corresponding EDS spectrum for the $CoFe_2O_4$ region (d) corresponding EDS spectrum for the $BaTiO_3$ region (e) pore size distribution as a function of differential pore volume distribution.

ation of the intensities for different elements was detected. The intensities of the elements Fe, Co were larger in the $CoFe_2O_4$ region while they were low in the $BaTiO_3$ region. In case of the elements Ba and Ti, the intensities were high in the $BaTiO_3$ region but lower in the $CoFe_2O_4$ regions. I attribute the existence of Ba, Ti intensities in $CoFe_2O_4$ regions to the area that is probed by the EDS analysis which may cover larger area than the $CoFe_2O_4$ regions and hence it scans both $BaTiO_3$ and $CoFe_2O_4$ regions with less intensity of Ba and Ti elements.

The porosity of the samples was measured by mercury porosimeter, samples have a small degree of porosity as shown in **Figure (5.7.e)**, e.g. for the sample with x=0.6, the maximum differential pore distribution is measured and the pore size distribution was 8-10 nm which is an indication of a dense ceramic.

5.6 AFM (MFM, PFM) analysis of the (0-3) composite

To check ferroelectric and ferrimagnetic properties, the techniques PFM and MFM were used. MFM shows active magnetic areas (see bright response in **Figure (5.8.a)**. These areas have a size of $\simeq 2$ μm which is compatible with the SEM data in **Figure (5.6)**. The same area was scanned using PFM. No response in the PFM images were detected for the magnetic regions as shown in **Figures (5.8.b)** and **(5.8.c)** for vertical and lateral PFM, respectively. These regions are magnetic $CoFe_2O_4$ which are surrounded by barium titanate shown in **Figures (5.8.c)** and **(5.8.d)**. The barium titanate matrix shows large PFM response, see bright and black regions in **Figures (5.8.b) and (5.8.c)**. **Figure (5.8.d)** shows higher magnification lateral PFM of image (c) in the barium titanate region.

Figure (5.9.a-5.9.c) shows topography and vertical and lateral PFM responses of the sample with x=0.6, respectively. The bright regions in **Figure (5.9.b)** and **(5.9.c)** represent the piezoresponse of barium titanate. These regions are distributed in size in the range of less than 700nm and surround the non-active $CoFe_2O_4$ regions. The active regions (bright regions) in **Figure (5.9.d)** represent the magnetic $CoFe_2O_4$ response to MFM.

5.7 Dielectric properties of the (0-3) composites

Figure (5.10) shows the temperature variation of dielectric permittivity at different frequencies. Samples with compositions x=0.8 and x=0.7 showed broad peaks at the paraelectric-ferroelectric phase transition. The phase transition temperatures are distributed in the range of (370-380)K and are smaller than the reported value of pure barium titanate 393K [33]. This shift in the phase transitions was probably caused by incorporation of Fe^{+3} ion in barium titanate lattice or by stresses resulting from the existence of cobalt iron oxide. At higher frequency the permittivity values are decreasing by decreasing the amount of barium titanate as shown in **Figure (5.11)**. The decreasing of

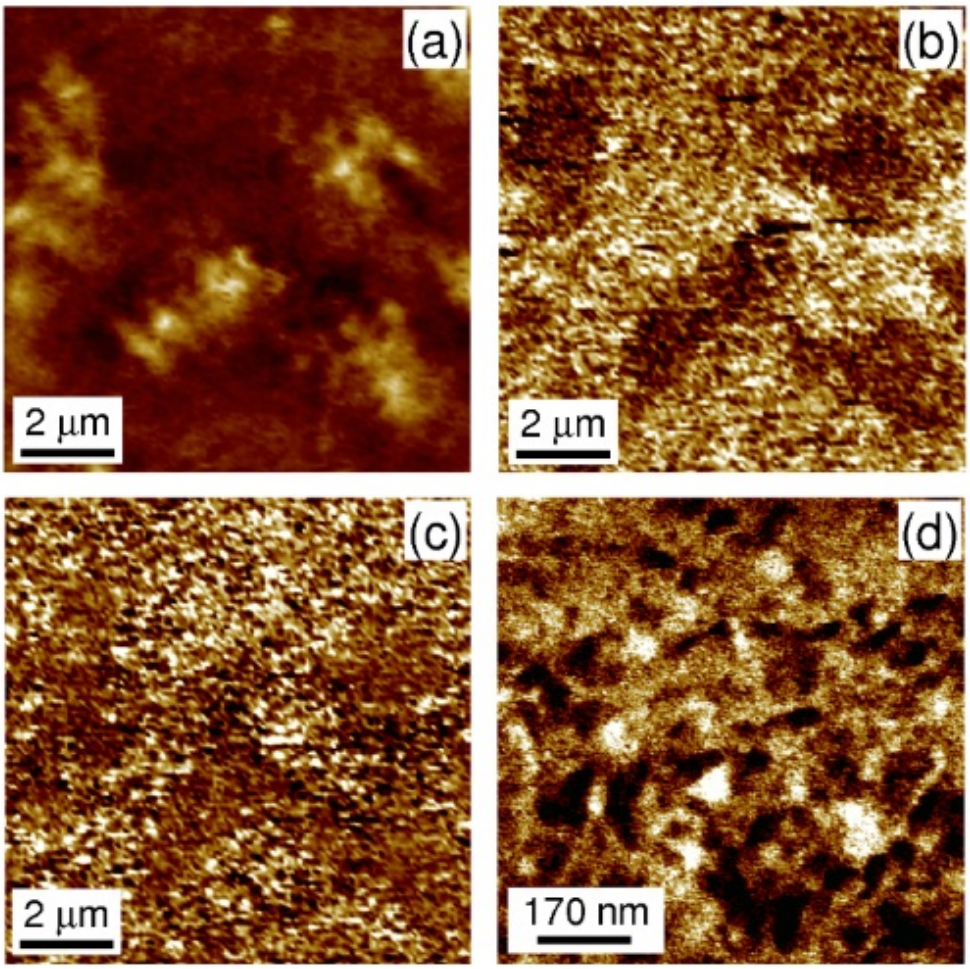

Fig. 5.8: (a) MFM image (b) vertical PFM (c) lateral PFM (d) zoom in laterial PFM response for the sample (1-x)$CoFe_2O_4$-x$BaTiO_3$ at x=0.8.

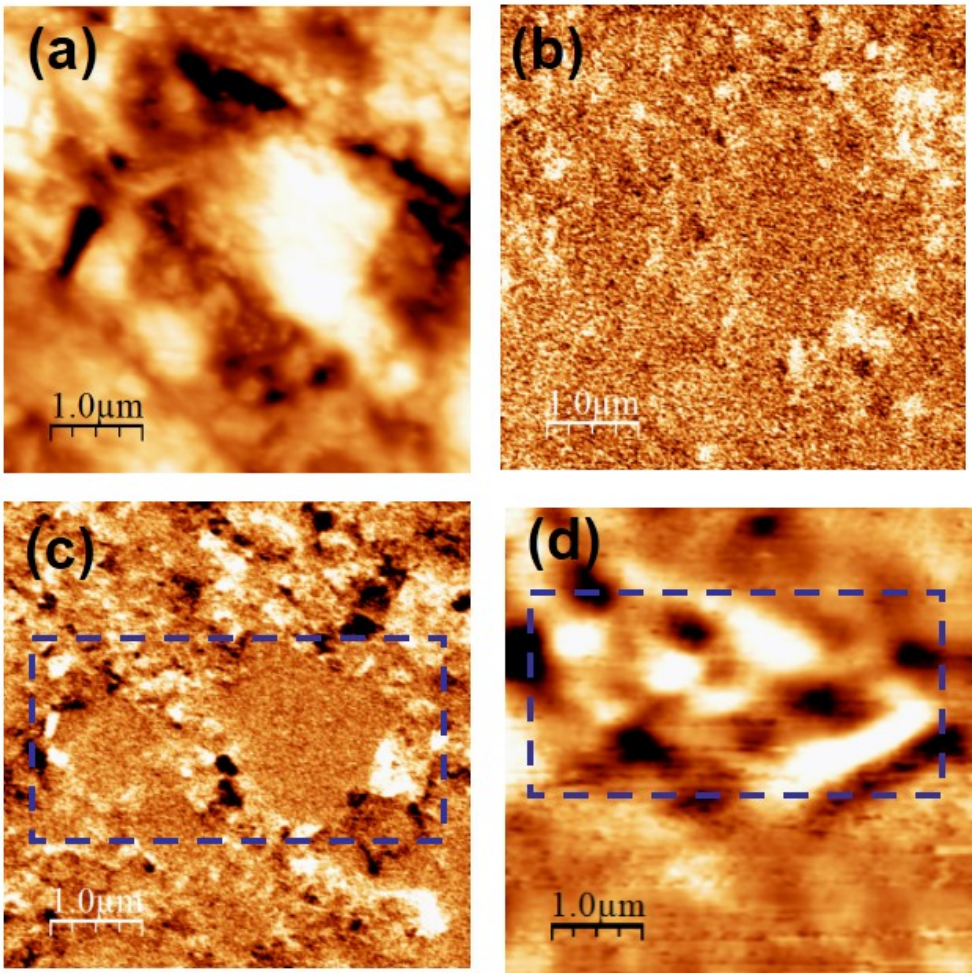

Fig. 5.9: Atomic force microscopy for the sample (1-x)$CoFe_2O_4$-x$BaTiO_3$ at x=0.6 showing (a) topography (b) vertical PFM response (c) lateral PFM response (d) MFM phase. The blue square shows the correlated region in the lateral PFM and the MFM image.

dielectric permittivity with respect to frequency is attributed to the Maxwell-Wagner type of interfacial polarization (see **Section (2.7)**). The maximum permittivity at 100kHz was measured for the composition of x=0.8 with value of 300 at phase transition, while small permittivity values $\simeq$80 were recorded for the composition x=0.5.

The energy loss (tanδ), which is expressed by the ratio of imaginary part of dielectric constant to real part for different compositions are shown in **Figure (5.10)** in the temperature range 320-430K for different frequencies. It was common for all samples that the dielectric loss decreases by increasing the frequency. For the temperature effect, the dielectric loss increases by increasing temperature for different frequencies. At low frequency, the composite of x=0.5 showed a significant higher dielectric loss than other compositions, this is related to the lower resistivity of the samples with higher amount of cobalt ferrite content (see **Figure (5.12.d)**). Samples with x$\leq$0.7 showed resistivity values around (1-20) GΩ·cm, while values between (60-100) GΩ·cm were measured for compositions with x$\geq$0.8. This can be attributed to significant diffusion and percolating conductive grains of cobalt iron oxide at higher content. However, appropriate processing procedures and conditions are also required to control the properties of such system.

5.8 Ferrimagnetic and ferroelectrics properties

For comparison of magnetic properties, measurements of the M-H loops for different compositions were done and shown in **Figure (5.12.a)**. A sample of sintered pure cobalt iron oxide was also measured for comparison. As expected, the saturation magnetization for different samples increases by increasing the content of cobalt ferrite in the composite. The pure cobalt iron oxide sample shows a saturation magnetization of 85 Am^2/kg which is the same value as for bulk $CoFe_2O_4$ [142]. All the samples showed lower remnant magnetization than the pure sample and no effect of barium titanate on the coercive field for

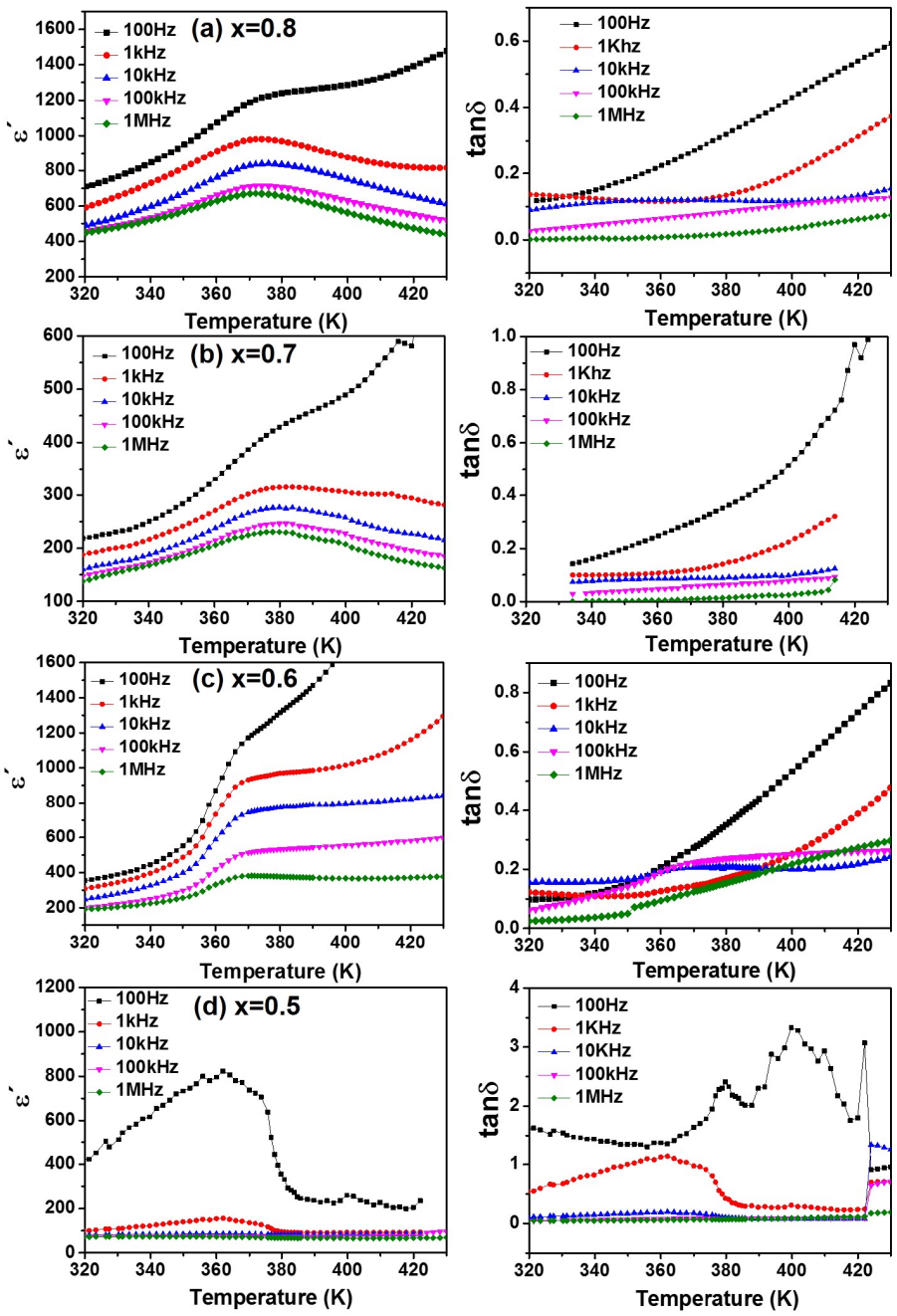

Fig. 5.10: Temperature dependence of dielectric permittivity for (1-x)$CoFe_2O_4$-x$BaTiO_3$ composites and the corresponding dielectric loss at various frequencies.

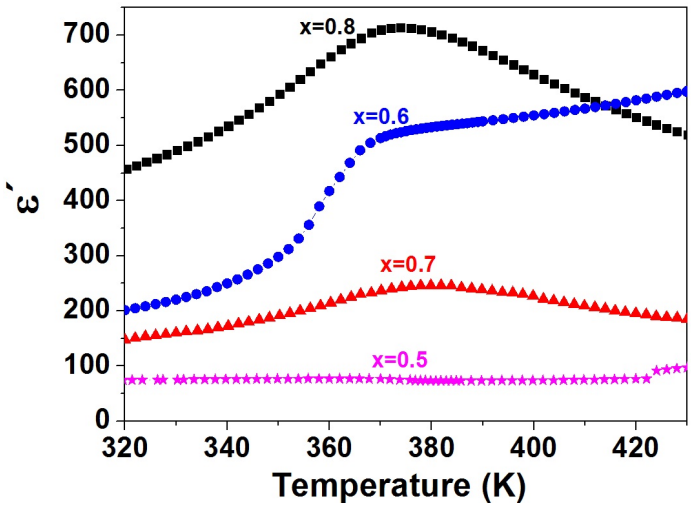

Fig. 5.11: Temperature dependence of dielectric permittivity for (1-x)$CoFe_2O_4$-x$BaTiO_3$ ceramic composites at f=100kHz.

the different composites was observed (**Figure (5.12.b)**).

P-E loops are shown in **Figure (5.12.c)** for different compositions including pure barium titanate. The extracted parameters of the loops are shown in **Figure (5.12.d)**. The saturation polarization and the resistivity of the samples increase with increasing amount of barium titanate. A resistivity of 100 GΩ·cm was measured for pure barium titanate; on the other hand, the sample containing 50 percent of cobalt ferrite has a resistivity value of 1 GΩ·cm. However, low saturation polarization values less than 8 $\mu C/cm^2$ were observed for all compositions. These values are lower than both barium titanate single crystal and high quality barium titanate ceramic with saturation values 25 $\mu C/cm^2$ and 14 $\mu C/cm^2$, respectively [35]. It was also shown that the amount of cobalt ferrite affects the electrical coercive field where a higher coercive field of 11kV/cm was measured for the 50 percent cobalt ferrite sample.

5.9 Phases, microstructure and the (3-0) connectivity of $CoFe_2O_4$-$BaTiO_3$ ceramic sintered by SPS technique

Another way of sintering was using the SPS as explained before. This method was chosen in order to keep the particles sizes as small as possible and to

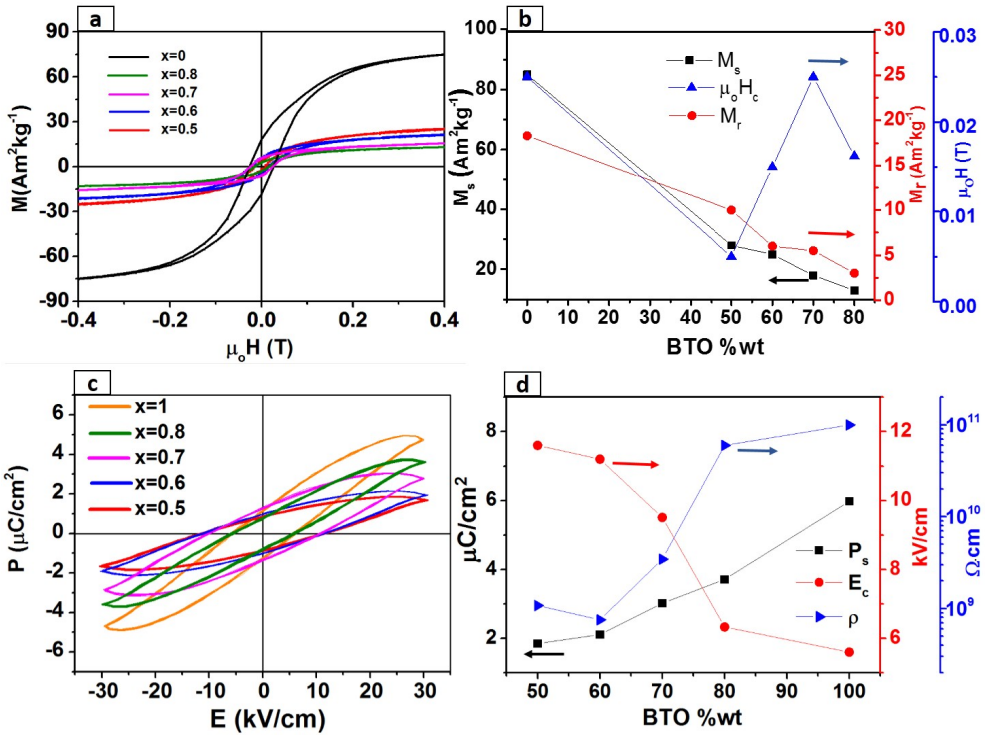

Fig. 5.12: (a) Room temperature M-H hysteresi loops for different (1-x)$CoFe_2O_4$-x$BaTiO_3$ compositions (b) dependence of M_r, M_s, H_c on compositions derived from magnetic hysteresis loops (c) P-E hysteresis loops for different compositions (d) Resistivity values for all compositions, E_c and P_s derived from the polarization hysteresis loops measured at 1kHz.

enhance the ceramic densification. A comparison between different $BaTiO_3$ and $CoFe_2O_4$ particles sizes will be discussed here. **Figure (5.13)** shows XRD results for the composite powder and ceramics sintered by the SPS method. Only $BaTiO_3$ and $CoFe_2O_4$ phases are detected without any trace of other phases or impurities. A broadening of the Bragg reflections observed for the powder sample indicates that the particle sizes are in the nanometer range. The intensities of cobalt ferrite Bragg peaks are much smaller than those of barium titanate. Both for the powder (**Figure 5.13.a)** and the ceramic sample sintered by SPS (**Figure (5.13.b)**, the structure of $BaTiO_3$ seems to be cubic, since no splitting of the Bragg reflections corresponding to crystallographic planes (200)/(002) and (112)/(211) is observed (see two bottom curves in **Figure (5.13.d)**). However, this can be also attributed to the broadening of the peaks in small particles [157]. On the other hand, for the annealed SPS sample the splitting of the peaks is clear, which indicates that $BaTiO_3$ is in a tetragonal and hence ferroelectric state [156]. Using **Equation (2.3)** the lattice parameters were calculated and the tetragonality was calculated to be 1.0112 for the annealed spark plasma sample.

Figure (5.14) compares the morphology for different samples. The as prepared powder showed a narrow size distribution around a mean diameter of 120 nm (**Figure 5.14.a**). This particle size distribution is compatible with previously reported data on cubic barium titanate with the same particle size described in **Chapter 4**. However, $CoFe_2O_4$ particles with 40nm diameter are found in the powder. The shorter time at high temperature of the SPS technique prevents grain growth as shown in **Figure (5.14.b)**. The $BaTiO_3$ grains (bright regions in the SEM image) were size distributed in the range of 160±30 nm. The $CoFe_2O_4$ grains were agglomerated and formed a matrix around the $BaTiO_3$. Close zoom for $CoFe_2O_4$ regions indicates the increase of $CoFe_2O_4$ grain size to about 70 nm. Annealing of the sample at 900°C for 2 hours resulted in further growth of $BaTiO_3$ grains up to 0.6-0.7 μm in diameter

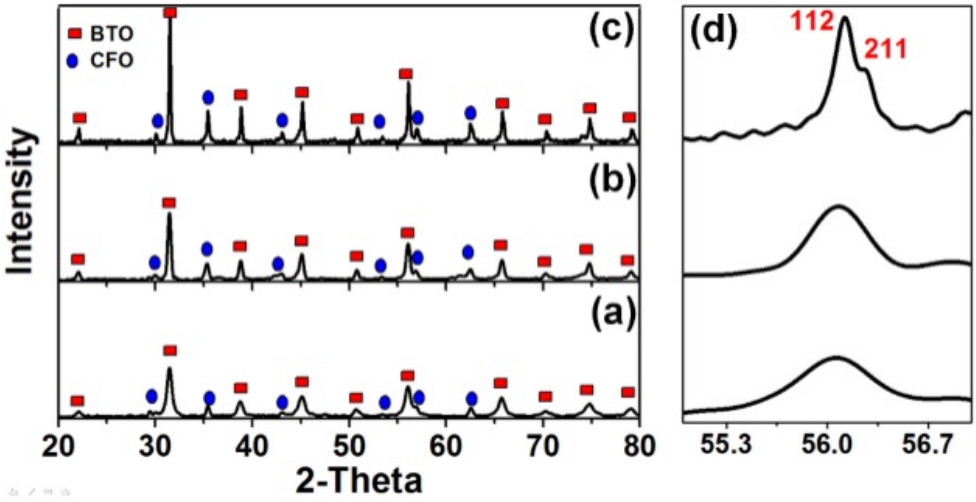

Fig. 5.13: XRD spectra of (1-x)$CoFe_2O_4$-x$BaTiO_3$ [x=0.5] composite for the samples (a) nanopowder calcined at 750°C for 15 minutes, (b) ceramic sintered by SPS at 1000°C for 5 minutes and (c) ceramic SPS sample annealed at 900°C for 2 hours. Diffraction peaks corresponding to the $BaTiO_3$ and $CoFe_2O_4$ phases are marked by squares and circles, correspondingly. Panel (d) shows an enlarged view of the diffraction peaks corresponding to the crystallographic (112) and (211) planes of $BaTiO_3$.

as shown in **Figure (5.14.c)**. Detailed inspection of the $CoFe_2O_4$ matrix revealed that the $CoFe_2O_4$ grains also grew to about 210 nm. Nevertheless the grain sizes remained much smaller in comparison to the sample sintered conventionally as shown in **Section (5.3)** where both $CoFe_2O_4$ and $BaTiO_3$ have grains in the micron range. The morphology and the structures for the samples are summarized in **Table (5.1)** comparing to the normally sintered one.

Tab. 5.1: Description of samples, powder, the SPS ceramic, the annealed SPS ceramic sample and the conventionally sintered one

	Powder	SPS ceramic	Annealed SPS ceramic	Normally sintered
connectivity	-	3-0	3-0	0-3
$BaTiO_3$ structure	cubic	cubic	tetragonal	tetragonal
D (nm) $BaTiO_3$	120	160±30	650±50	1000-2500
D (nm) $CoFe_2O_4$	40nm	70±10	210±25	1000-1500

Figure (5.15) shows PFM images for polished surfaces of ceramic samples. For the sample sintered by SPS (**Figure (5.15.b)**), no PFM active regions

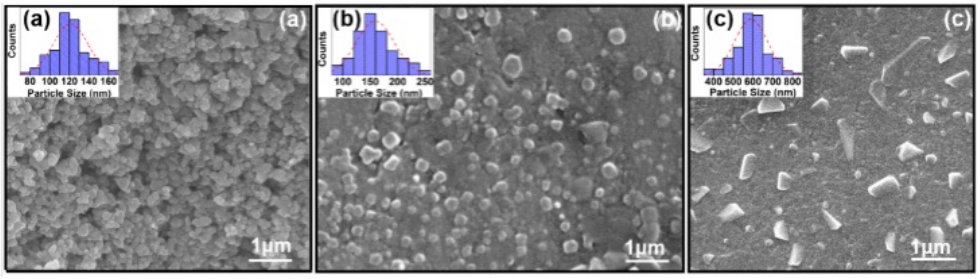

Fig. 5.14: SEM images obtained using backscattered electron mode of samples (a) nanopowder (b) SPS sample and (c) annealed SPS sample. The insets show the barium titanate particle size distribution of for each sample

were detected, which correlates with the cubic paraelectric structure of $BaTiO_3$ in this case. On the contrary, both the SPS annealed sample and the normal sintered sample have regions with distinct PFM response showing bright and dark contrasts in **Figures (5.15.d)** and **(5.15.f)**. These regions correspond to the ferroelectric $BaTiO_3$ grains. For the SPS sintered and annealed sample, these grains are distributed in the $CoFe_2O_4$ matrix approaching (3-0) connectivity (or potentially (3-3)). The average size of the $BaTiO_3$ regions is 700 nm which is compatible with the SEM data. The normally sintered sample shows a completely different morphology: piezoelectrically non-active $CoFe_2O_4$ regions are isolated and distributed in the $BaTiO_3$ matrix. Thus in this case, the connectivity (0-3) has been formed.

To prove the ferroelectric character of the $BaTiO_3$ phase, local PFM hysteresis loops were measured for the annealed SPS sample. A typical hysteresis loop is shown in **Figure (5.16)**. The change of the phase of the PFM signal by 180 degrees confirms polarization switching at approximately 10 V (**Figure (5.16.b)**). The maximal piezoelectric displacement reaches about 0.4 nm at the maximal applied dc bias (30V). Taking into account the amplitude of the probing ac voltage (8V), the value of the local longitudinal piezoelectric coefficient can be estimated as $d_{33} \simeq 50$ pm/V.

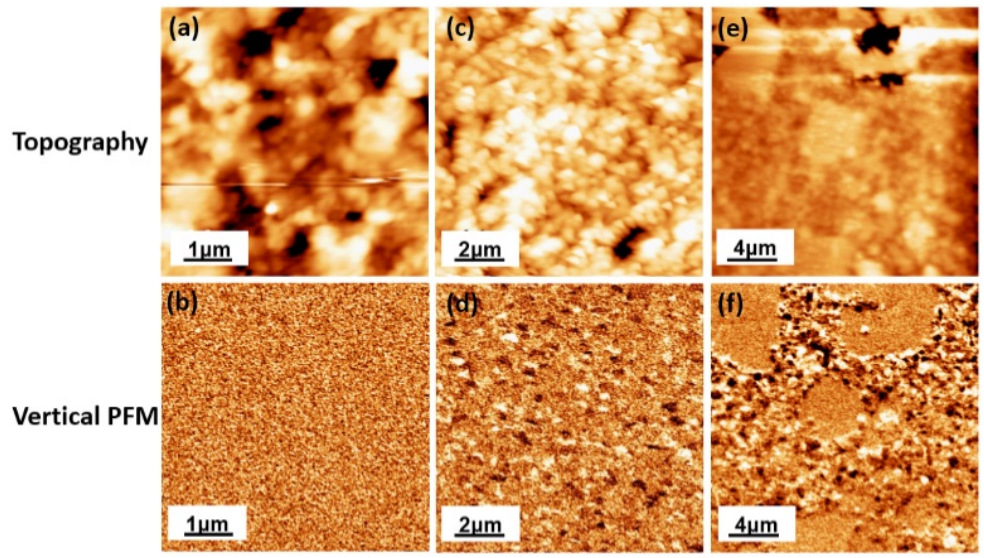

Fig. 5.15: PFM images of the $CoFe_2O_4$-$BaTiO_3$ composites: (a) topography and (b) vertical PFM response of sample sintered by SPS; (c) topography and (d) vertical PFM response of annealed SPS sample; (e) topography and (f) vertical PFM response of normally sintered sample [image by Harsh Trivedi].

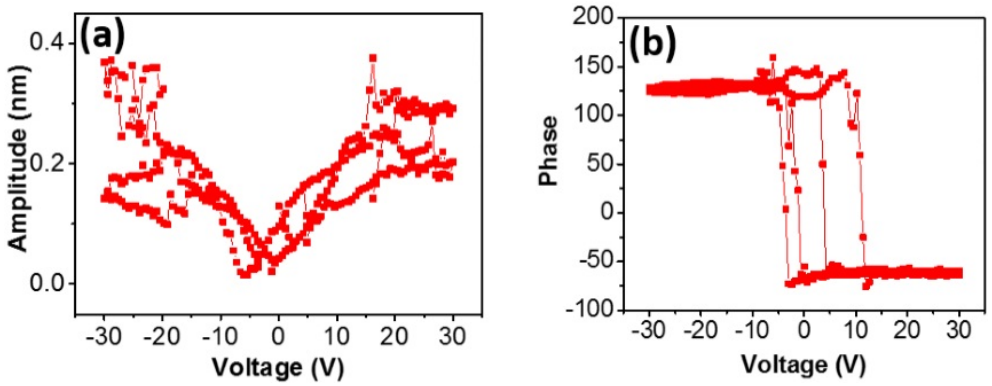

Fig. 5.16: Local piezoresponse hysteresis loops: (a) amplitude and (b) phase, in a $BaTiO_3$ grain for the annealed SPS sample [courtesy by Harsh Trivedi].

5.10 Ferroelectric, ferrimagnetic, and dielectric properties for the (3-0) $CoFe_2O_4$-$BaTiO_3$ ceramic composite

Typically, ferroelectric properties of the materials are studied by the observation of polarization switching using the Sawyer-Tower method. However, in conductive samples the leakage current can strongly affect the measurements resulting e.g. in overestimated polarization or coercive field values. Indeed, the total charge in the sample, Q_{total}, measured by the Sawyer-Tower method can be expressed by the following equation:

$$Q_{total}(t) = P(E(t)) \cdot A + \int_0^t I(E(t)) \cdot dt \tag{5.1}$$

where P is the polarization, E is the electric field, A is the sample electrode area, I is the leakage current, and t is time. The time dependence of the current I can be estimated from leakage current measurements as I(t)=V(t)/R, where V(t) and R are the applied voltage and leakage resistivity, respectively. Leakage is assumed to be ohmic. **Figure (5.17)** shows the polarization dependence of electric field for the annealed SPS sample (**Figure (5.17.a)**) and the normally sintered one (**Figure (5.17.b)**). Both the directly measured hysteresis loops and the corrected curve after subtracting the leakage contribution are shown. One can see that the P(E) dependences retain the hysteretic behaviour indicating the ferroelectric character of the $BaTiO_3$ phase. The leakage is very clear for the annealed SPS sample and does not seem to be fully removable assuming a static resistor correction. Thus, AC leakage of Maxwell-Wagner type could be partly present (see **Section (2.7)**) [158]. The normally sintered sample shows very low leakage contribution due to the highly resistive nature of the (0-3) composite, so that the measured curve exactly coincides with the non-corrected curve as shown in **Figure (5.17.b)**. The sample which is directly sintered by SPS was very leaky so one could not apply large enough voltage to observe polarization switching.

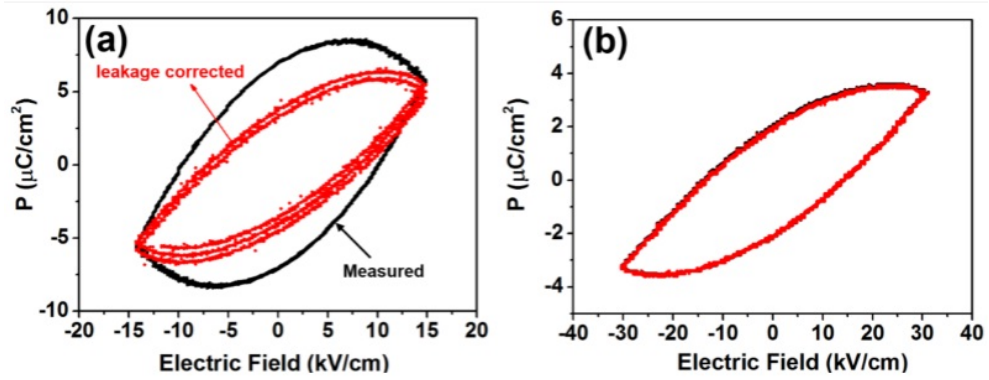

Fig. 5.17: Room temperature polarization-electric field hysteresis loops measured at 100 Hz showing the new curve after subtracting the (static) leakage contribution for (a) annealed SPS sample and (b) normally sintered sample.

The dielectric characteristics of different samples are compared in **Table (5.2)**. The two SPS samples show larger permittivity values but larger dielectric losses in comparison to the conventionally sintered sample. The high losses are a consequence of large amounts of conductive $CoFe_2O_4$ forming the matrix.

Tab. 5.2: Room temperature dielectric and magnetic properties for different samples [S1: sintered by SPS, S2: annealed SPS sample, S3: normally sintered]

Sample	ϵ at 100kHz	tanδ at 100kHz	M_s Am^2/kg	M_r Am^2/kg	M_r/M_s	$\mu_o H_c$ mT
S1	175	0.25	32.5	15.5	0.48	47
S2	208	0.47	32	15	0.47	45
S3	73	0.033	27	10	0.37	45

Figure (5.18) shows the magnetic field dependences of the mass magnetization measured at room temperature. The extracted magnetic parameteres are listed in **Table (5.1)**. For $CoFe_2O_4$ -$BaTiO_3$ composite nanoparticles with a $CoFe_2O_4$ core diameter of about 40 nm, the sample shows low remanent magnetization (M_r) and a very small coercitive field (H_c) value, probably caused by superparamagnetic effects as shown in chapter 3. For the sample sintered at 1000^{o}C by SPS, both the coercive field and the remanent magnetization increase substantially. This could be attributed to increasing $CoFe_2O_4$ particle sizes (70±10 nm) (**Table 5.1**) resulting in a cross-over from superparamag-

netic to ferrimagnetic behavior. Concurrently, the saturation magnetization (M_s) increases only slightly. The annealing did not affect the magnetic properties (S2) as shown in **Figure (5.18)**. Suprisingly, the SPS prepared samples (S1 and S2) in **Table (5.2)** showed larger magnetization in comparision to the coventionally sintered ceramic (S3) in spite of much larger $CoFe_2O_4$ grains about 1-1.5μm. For the sample which was normally annealed, the saturation and remnant magnetization were only 27 Am^2/kg and 10 Am^2/kg, respectively. The increased magnetization in SPS sintered ceramics might be due to the higher density of the sample as well as due to the (3-0) connectivity. The conventionally sintered ceramics S4 has (0-3) connectivity with separates $CoFe_2O_4$ grains. In general, the magnetic anisotropy, saturation magnetization, and its temperature dependence is related to the grain size [132, 141] and cation distribution [88]. The value of hysteresis squareness, M_r/M_s, is important because it provides information about magnetocrystalline anisotropy and exchange interaction for magnetic samples [159]. The SPS samples display squareness values close to 0.5, which indicates that the $CoFe_2O_4$ particles are single-domain and have uniaxial anisotropy [160].

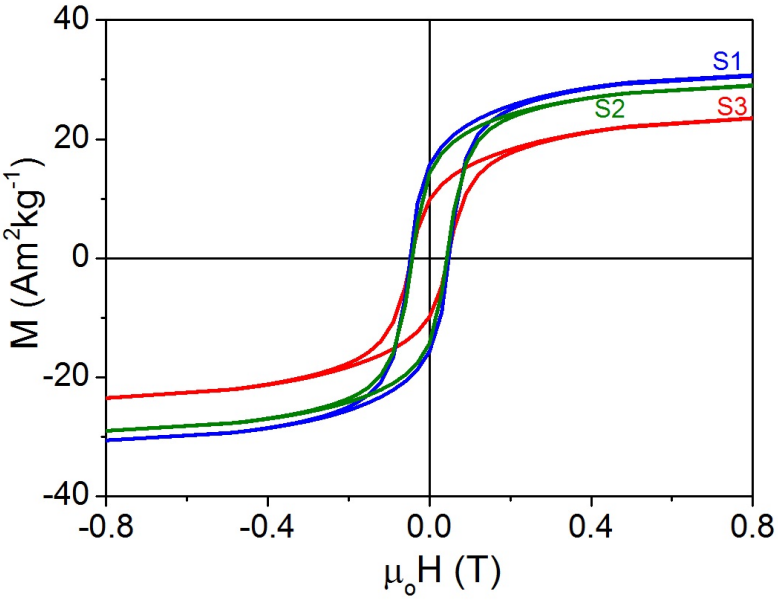

Fig. 5.18: Room temperature magnetization hysteresis loops for the different $CoFe_2O_4$-$BaTiO_3$ samples [S1: sintered by SPS, S2: annealed SPS sample, S3: normally sintered].

6. MAGNETOELECTRIC EFFECT IN $CoFe_2O_4$-$BaTiO_3$ COMPOSITES

After investigating morphologies for different compositions, which were shown in the previous chapter, and the ferroelectric and ferromagnetic properties, measuring the ME effect is very important as the final investigation. It was carried out using different methods. In the upcoming sections, I will describe different results measured by different techniques in order to prove and measure the ME effect. First, the effect of magnetic field on the ferroelectric domains using an AFM set-up with variable magnetic field unit was detected with cooperation with M.Sc. Harsh Trivedi. In this method, the PFM analysis was done for different samples before and after application of magnetic fields, then the effect of magnetic field on the ferroelectric piezoresponse can be detected. In the second method, the converse ME effect was measured using a SQUID magnetometer with cooperation of M.Sc. Soma Salamon and Dipl.-Phys. Joachim Landers in the faculty of physics in Duisburg campus. This was done at different temperatures and different dc magnetic fields. In the third method, the direct magnetoelectric effect was analyzed and measured using the dynamic lock-in technique. This method was constructed and developed by myself in our group in Essen campus. X-ray absorption spectroscopy including linear and circular dichroisms was used in order to measure the electric polarization under different magnetic fields at the surface. These measurements were done at HZB-BESSY(II) by Dr. Carolin Schmitz-Antoniak from Peter Grünberg Institute Forschungszentrum Jülich. The results of all measurements are explained in the following sections.

6.1 Observation of the ME effect by AFM

The first indication of the ME effect was obtained using PFM with and without an in-plane magnetic field on the ceramic sample containing 40wt.% of $CoFe_2O_4$. **Figure(6.1.a)** shows PFM images corresponding to piezoactive $BaTiO_3$ grains (bright regions). Size of these regions is less than 700nm. They are surrounded by piezoelectrically non-active $CoFe_2O_4$ regions (brownish regions). This image confirms the (0-3) nature of the composite by the dispersion of the $CoFe_2O_4$ regions within the $BaTiO_3$ matrix. The marked region was chosen in order to see the effect of a magnetic field on the PFM response (see **Figure 6.1.b**). The root mean square (RMS) of PFM amplitude in this regions was increased from 96pm to about 240pm when applying μ_oH=0.1T magnetic field parallel to the sample surface. This increase of the PFM response indicates that strain comes from the deformation of the $CoFe_2O_4$ regions due to the magnetostriction transferred to the $BaTiO_3$ regions because of the strain-mediated ME effect. A local polarization loop (**Figure 6.1.c**) was measured with coercive voltage 5 V in the positive voltage and -10 V in the negative one. The applied voltage of 20V was enough to switch the polarization of the marked domain. This domain also has large remnant polarization as indicated in the figure. The strain voltage loops were also measured for the sample region as shown in **Figure (6.1.d**). The local strain hysteresis loop is similar to the barium titanate bulk strain hysteresis loop. An amplitude of about 1.2 nm was detected when applying 30 V.

The selected PFM spot shown previously was scanned for PFM again at contact resonance under variable magnetic field μ_oH= 0, 0.05, 0.1, -0.05 and -0.1T. Piezoresponse and the local pizeoresponse hysteresis loops data were collected, and the obtained image matrix was normalized and analyzed [161]. **Figures (6.2.a-e)** show the PFM scans at different magnetic fields and the corresponding images with the minimum color map scale value increased to a fixed value in order to see the peak value map. The peak values are clearly changed

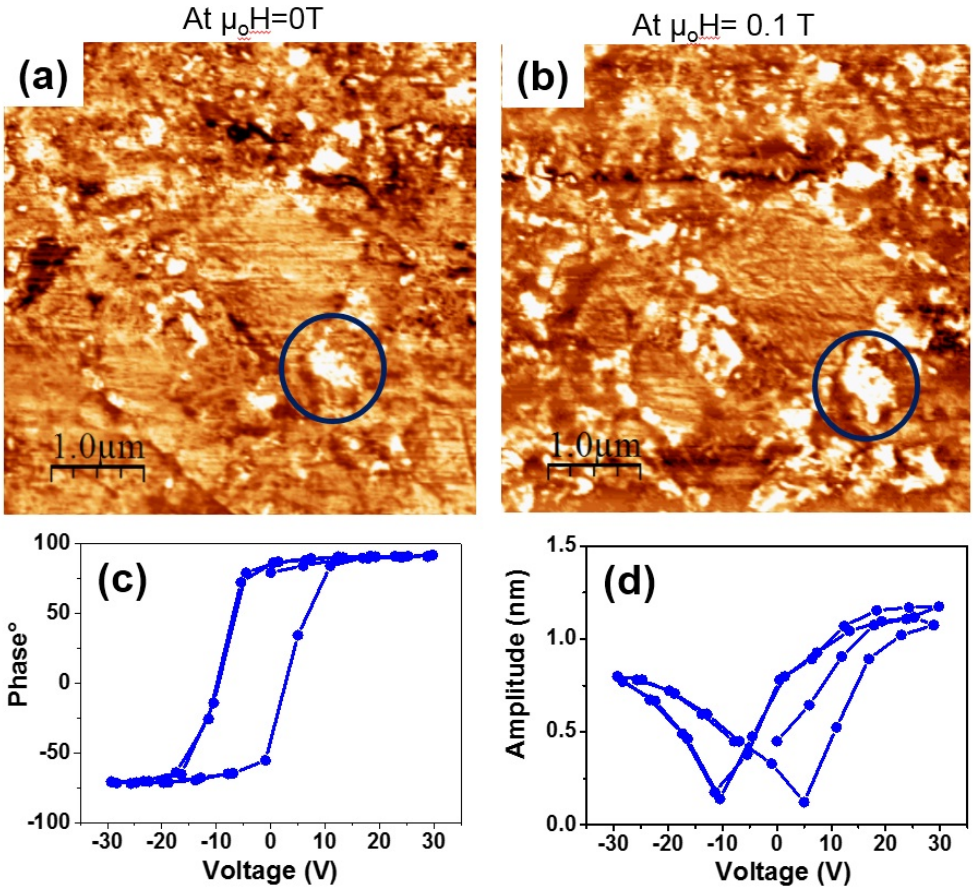

Fig. 6.1: PFM photo at 0 T magnetic field (b) PFM scan at μ_oH=0.1T (c) phase voltage hysteresis loop measured for the marked domain (d) voltage strain loop at the same marked region for the normally sintered sample (1-x)$CoFe_2O_4$-x$BaTiO_3$ at x= 0.6 [Image by Harsh Trivedi].

according to different magnetic fields. A symmetrical behavior was notified when applying positive and negative magnetic fields see **Figure (6.2.a) and Figure (6.2.e)** for μ_oH=0.1T and μ_oH=-0.1T, respectively. The symmetry of the response came from the symmetrical behavior of the cobalt ferrite magnetostriction response to dc magnetic fields. This magnetostriction effect transfers to the barium titanate phase and causes direct piezoelectricity.

6.2 Converse magnetoelectric effect measured by SQUID susceptometer

In this section, the measurement of the converse magnetoelectric effect using a modified SQUID susceptometer is presented. The setup is able to measure the change in magnetization (δM) with respect to an ac electric field (δE). Different sample compositions were tested. The procedures of testing were described previously in **Chapter (2)**. The ME samples were inserted into the SQUID so that the sample surface is perpendicular or parallel to the applied magnetic field. The samples were electrically poled so that the direction of the polarization is perpendicular to the sample surface. Tests were performed for temperature dependence of the ME effect and the effect of H_{dc} magnetic field on the induced magnetization. The effects of poling and permittivity will be also discussed.

6.2.1 The effect of poling on the converse ME effect

Figure (6.3) shows the effect of poling on the ME effect. In spite of the importance of the poling process, the effect of poling on ME coefficient is rarely reported. The depoled sample curve (1) in **Figure (6.3)** showed a non-linear ME effect (circles) with very weak induced magnetization value of M_{ind}=0.4 A/m at electric field 3.3 kV/cm. It exhibits a small induced magnetization due to the small finite slope of the strain electric field curve (see **Figure (1.16)**). In opposite, the poled sample curve (2) in **Figure (6.3)**

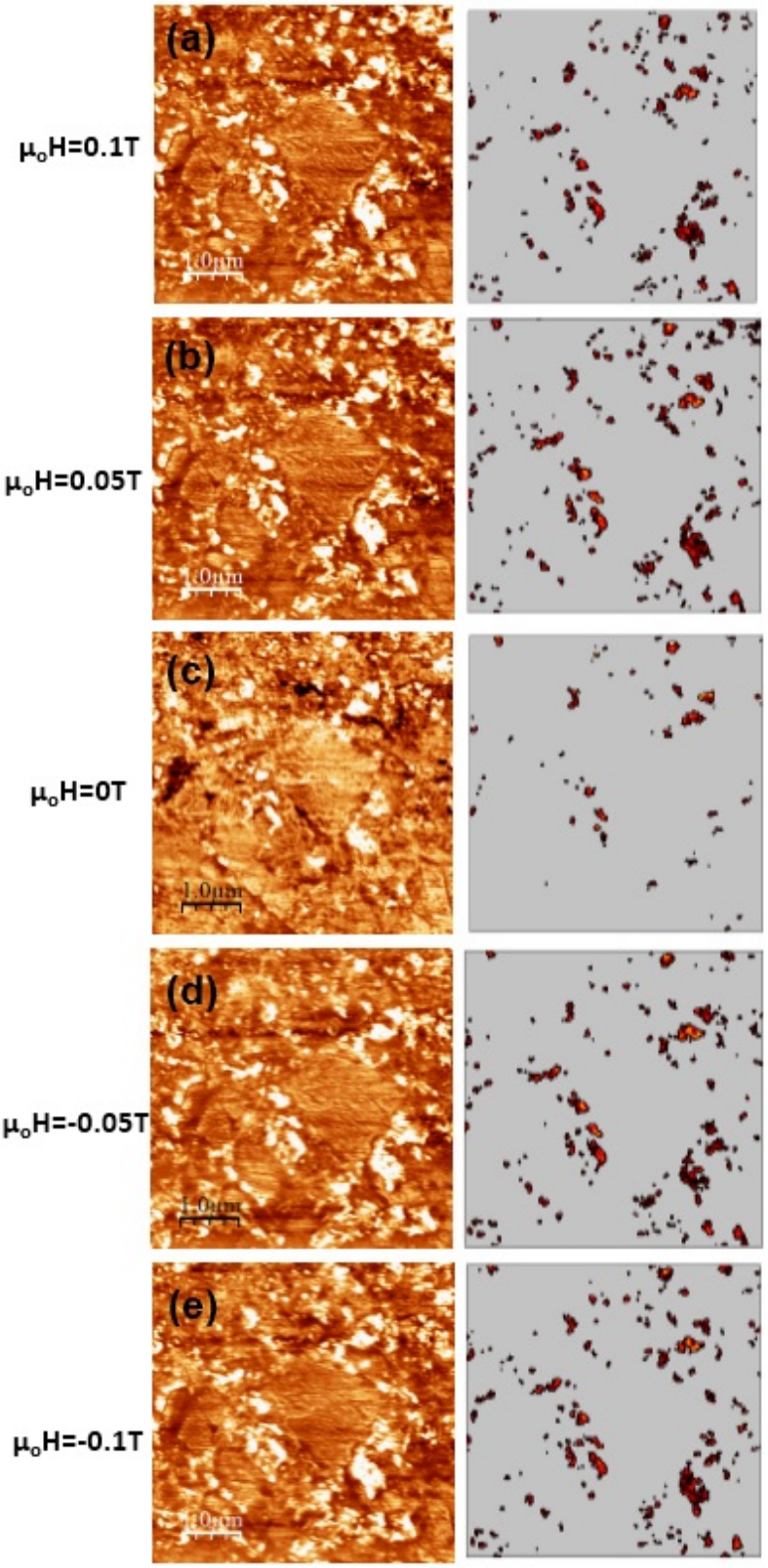

Fig. 6.2: PFM images at contact resonance and the corresponding threshold offset images at different magnetic field at (a) μ_oH=0.1T (b) μ_oH=0.05T(c) μ_oH=0T (d) μ_oH=-0.05T (e) μ_oH=-0.1T, for the sample (1-x)$CoFe_2O_4$-x$BaTiO_3$ at x=0.6 [image by Harsh Trivedi].

showed perfect linear ME effect and the value of the induced magnetization reached about M_{ind}=7.5 A/m. This difference can be explained by enhancing the piezoelectric coefficient after poling which is very important for magneto-electricity in composites. It is well known that the ME effect is proportional to the values of piezomagnetic coefficient, q_{11}, piezoelectric coefficient, d_{33}, and the applied electric field E as illustrated in **Equation 1.24**. For barium titanate ceramic, it was shown that piezoelectric coefficients values of d_{31} and d_{33} were increased 3 times and 15 times by poling, respectively [162]. Poling piezoelectric ceramics with an electric field perpendicular to the sample surface enhances the effective polarization and the longitudinal piezoelectric coefficient as indicated by the equation [37]:

$$d_{33} = 2Q_{11}\epsilon_o\epsilon_{33}P_3 \tag{6.1}$$

where Q_{11} is the electrostrictive constant, ϵ_{33} is the relative permittivity, ϵ_o is the vacuum permittivity, and P_3 is the polarization. The increase of both values, the polarization and the permittivity can improve the poling state of the sample and consequently the resulting ME effect.

Ma et al. [163] simulated the ME effect for both (0-3) and (3-0) barium titanate cobalt ferrite particulate composites. They found that in-situ poling of the ferroelectric phase is very important in order to enhance the piezoelectricity and thus the ME effect. They simulated the change in polarization ΔP_3 after applying an electric field. The nonzero value of magnetoelectric coefficient in column (a) in **Figure (6.4)** was related to the lack of piezoelectricity. They found that the value of the ME effect is increased by about 10 times after poling as shown in **Figure (6.4)** column b. The fully polarized state yielded small but non-zero conductivity of the magnetic phase. Nevertheless, this gave the maximum piezoelectricity and hence enhanced the ME coupling by a factor of 5.5 compared to the poled sample as shown in **Figure (6.4.c)**. In general, their findings are compatible with experimental results, however

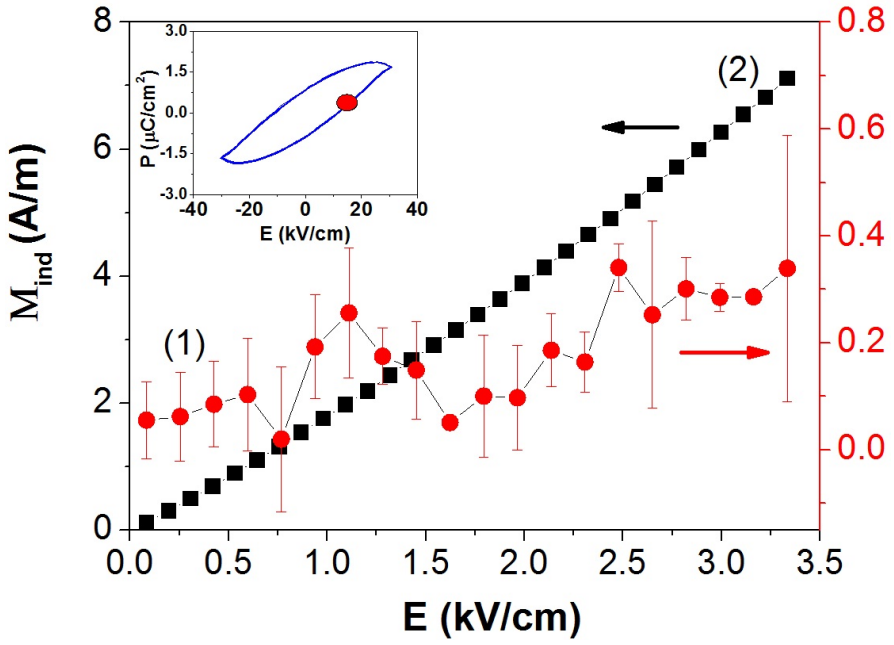

Fig. 6.3: Amplitude of the induced magnetic moments by applied voltage showing the behavior of curve (1) unpoled sample and curve (2) poled one for the composition (1-x)$CoFe_2O_4$-x$BaTiO_3$ at x=0.5 at 3Hz, 285K and 0.15T. [The inset shows the real P-E loop and the poling state position]

the modeling procedures suggested ideal (0-3) structure and completely isolated magnetic regions distributed in the ferroelectric phase, which is difficult to achieve experimentally.

6.2.2 The linearity of the converse ME effect

The induced magnetization for compositions of x=0.5, x=0.6 and x=0.8 is shown in **Figure (6.5)** in the electric field range (0-3.5 kV/cm). The sample with x=0.5 showed larger induced magnetization than the x=0.8 and x=0.6 one with almost linear relation between the induced magnetization and the applied field. This measurement was done at T=285K and H_{dc}=1500 Oe because the maximum ME effect was recorded exactly at these parameters values, which will be described more through the chapter. The converse magnetoelectric coefficient α_c can be estimated from the curves by calculating the slopes using the following equation:

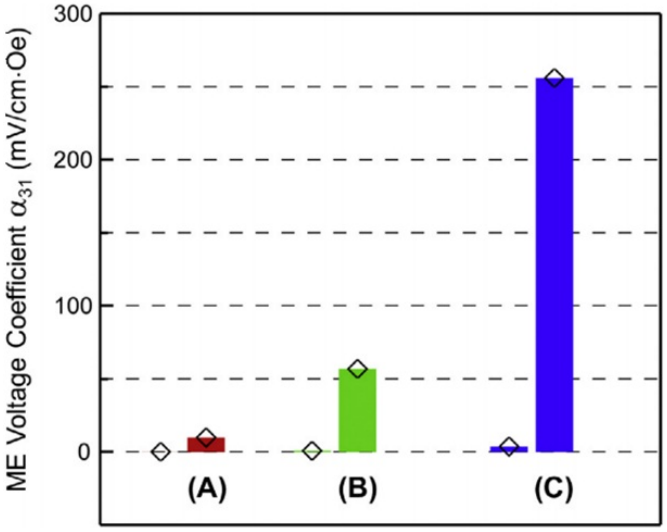

Fig. 6.4: Simulated ME effect coefficient (α_{31}) of $BaTiO_3$-$CoFe_2O_4$ particulate composite showing (a) unpoled state of the sample (b) poled state of the sample (c) poled but small conductivity of the isolated magnetic particles [the right columns are for (0-3) composite and the left one for (3-0) one[reprinted with permission from Elsevier [163]].

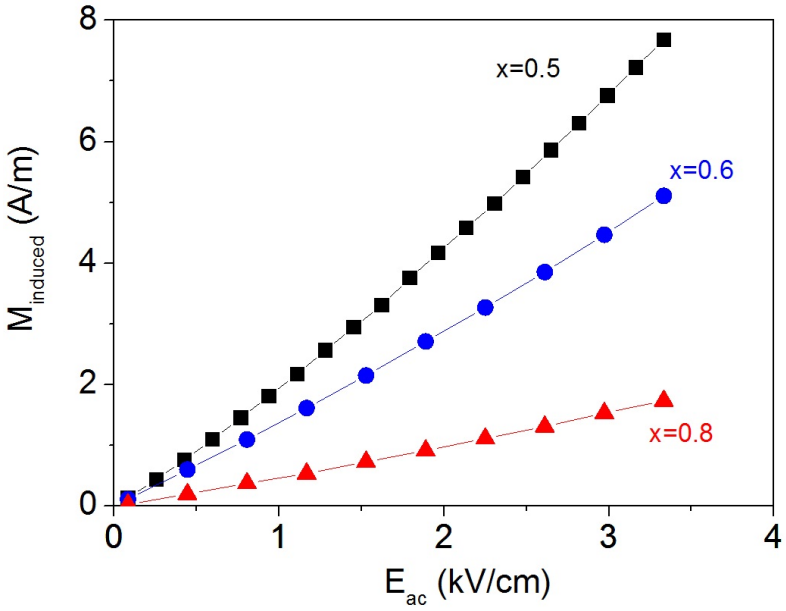

Fig. 6.5: Amplitude of the induced magnetic moments as a function of applied voltage, for composition x=0.5, x=0.6 and x=0.8 [at T=285K, f=3Hz, $\mu_o H_{dc}$=0.15T].

$$\mu_o M_{ind} = \alpha_c E_{ac} \tag{6.2}$$

6.2.3 Temperature dependence of the converse ME effect

In order to study the effect of temperature on the converse ME effect, the magnetoelectric effect M_{ind}(T) was measured in the temperature interval of 5K-330K at the superimposed magnetic field μ_oH=0.15T for the composition of x=0.6 as shown in **Figure (6.6)**. The effect seems to be constant in the temperature interval from 0-150K. A small peak appeared at temperature 130K. The effect then decreased more until reaching the temperature 175K and then increased and reached the maximum value at 270K and then decreased and reached the minimum at about 320K and then increased again. I believe that the observed behavior of the ME effect here is related to the temperature dependence of the piezoelectric response of $BaTiO_3$, because the sudden change of the magnetoelectric effect at certain points such as 175K and 263K represent the phase transitions of barium titanate from rhombohedral to orthorhombic and from orthorhombic to tetragonal phase, respectively. All of the samples show similar behavior with maximum magnetoelectric value in temperature range 270-280 K.

For more explanation about the temperature effect, the magentoelectric effect depends mainly on the piezomagnetic coefficient (q) of the cobalt ferrite and the piezoelectric coefficient (d) for barium titanate, see **Equation (1.24)**. The value of piezoelectric coefficient (d) is proportional to the value of permittivity ϵ_{33}, see **Equation (6.1)**. It is shown that the value of the permittivity ϵ_{33} mainly depends on the temperature. These permittivity values reach a maximum at the phase transitions as shown in **Figure (5.10)**. These large values of permittivity at phase transition temperatures will maximize the value of piezoelectric coefficient and hence enhanced the the ME effect. In other words, the samples are polarised at phase transitions and depolarised after that. For both sample orientations (longitudinal and transverse), the

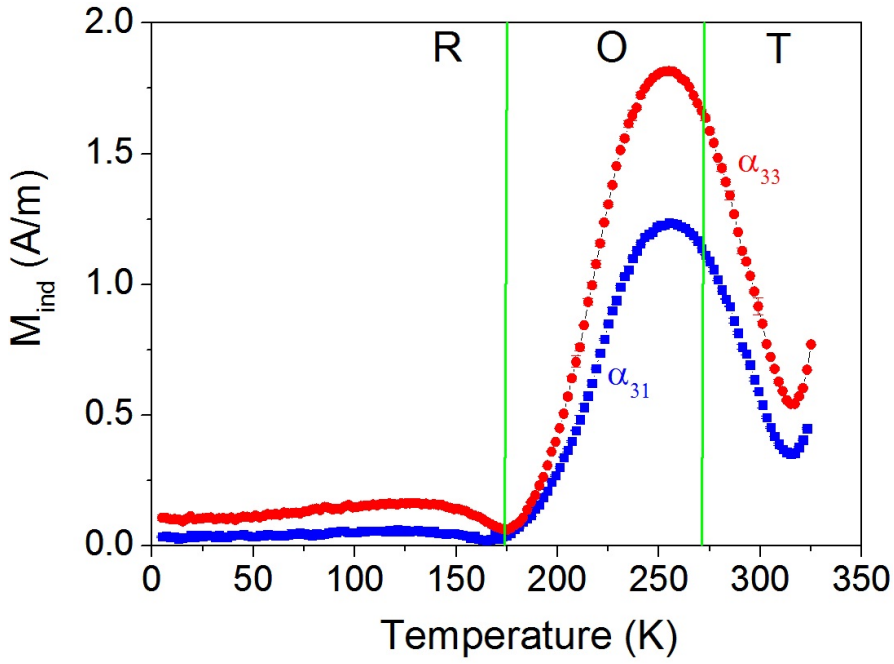

Fig. 6.6: Amplitude of the induced magnetic moments as a function of temperature, for composition x=0.6 at [E_{ac}=100V, f=3Hz, $\mu_o H_{dc}$=0.15T] the letters indicates the phase transition where T: tetragonal, O: orthorhombic R: rhombohedral. The measurements were done for both longitudinal and transverse modes.

temperature dependence of the ME effect showed similar behavior. Both values of the ME effect α_{33} and α_{31} ME coefficients match the exact temperature dependence with higher value for the longitudinal one. In fact, I excluded any effect of (q) on the temperature dependence of the converse ME effect, because for pure cobalt ferrite the derivative dλ/dH is usually increased by decreasing temperature and not vice versa [164]. Indeed, more investigations are needed in order to explain the effect of both piezomagnetic and piezoelectric coefficients simultaneously on the temperature dependence of the converse ME effect.

Another investigation of the influence of temperature on the magnetoelectric effect was done for both the normally sintered sample and the annealed SPS one which have connectivity schemes (0-3) and (3-0), respectively (see **Figure (6.7)**). Both samples contain 50 weight percent of cobalt ferrite. In **Figure (6.7.a)**, the sample shows a maximum magnetoelectric effect value at about

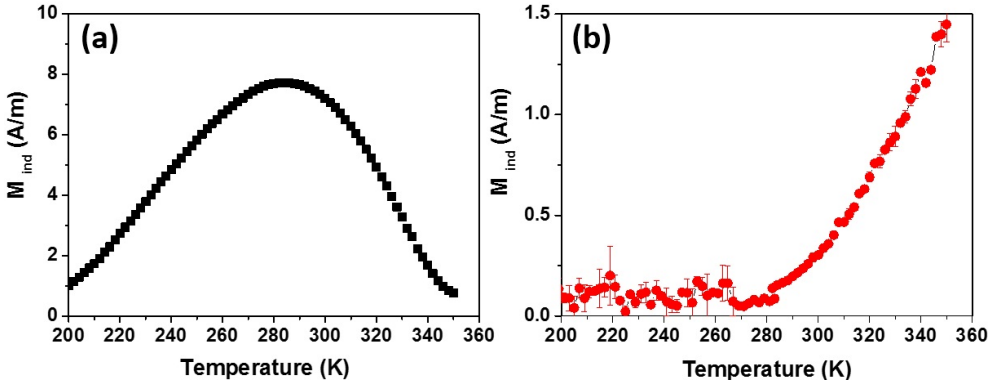

Fig. 6.7: Amplitude of the induced magnetization as a function of temperature for (a) normally sintered sample (b) annealed SPS sample with x=0.5, the measurement was done at [E_{ac}=200V, f=3Hz, $\mu_o H_{dc}$=0.15T] [55].

285K which is compatible with the maximum measured value in **Figure (6.6)** for x=0.6 and the value of x=0.8 previously reported [152]. This temperature is the orthorhombic to tetragonal phase transition of barium titanate. For the SPS annealed sample with (3-0) connectivity **Figure (6.7.b)**, the sample shows apparent magnetoelectric coupling that is entirely due to the leakage. The increasing of the measured signal above 300K is related to the increase of the number of thermally activated charge carriers and not related to the magnetoelectric effect. In this case, the leakage current through the sample can lead to a significant magnetic signal [55]. However, It was reported that conductive magnetostrictive inclusions will not yield significant magnetoelectric coupling due to the effect of leakage currents [165].

6.2.4 Dependence of the converse ME effect on the DC magnetic field

Figure (6.8.a) shows the dependence of the electrically induced magnetization on the dc magnetic field for the composition x=0.5. Symmetrical behavior was observed for positive and negative dc magnetic fields taking into consideration the amplitude value of the induced magnetic moments. The maximum value of the induced magnetization was reached at μ_oH=0.15T. The ME effect is then decreased after that and reaches the minimum value $\simeq$0 at μ_oH=0.9T. In order to explain the relation between the magnetoelectric effect

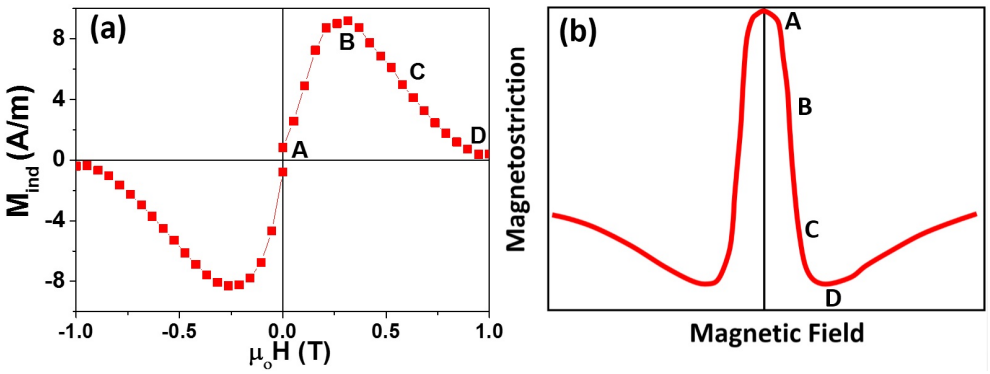

Fig. 6.8: Induced magnetization as a function of dc magnetic field for the composite (1-x)$CoFe_2O_4$-x$BaTiO_3$ at x=0.5 at T=285K, V_{ac}=200V, f=3Hz (b) schematic drawing of polycrystalline $CoFe_2O_4$ magnetostriction.

and the magnetostriction, a typical magnetostriction curve for the polycrystalline cobalt iron oxide was drawn and shown in **Figure (6.8.b)**. The ME response in **Figure (6.8.a)** tracks the H_{dc} dependence of the piezomagnetic coefficient where the ME effect is proportional to piezomagnetic coefficient q and the longitudinal piezoelectric coefficient d (see **Equation (1.24)**).

To explain the behavior, the magnetostriction values in the AB region in **Figure (6.8.b)** is increasing so that the value of the ME effect is also increasing. The slope (dλ/dH) reaches a maximum at point B in **Figure (6.8.b)** so that the value of dM/dE also reaches a maximum at the point B in **Figure (6.8.a)**. In the region of BC, the slope (dλ/dH) decreases so that the value of ME effect is also decreased in the region of BC **(Figure 6.8.b)**. The value of (dλ/dH) is decreasing until reaching the lowest change in point D. At this point, the value of the ME effect is close to zero. After the point D in **Figure (6.8.b)**, the slope is negative and the dλ/dH changes sign so that the value of dM/dE is also changed and increases after the point D as shown in **Figure (6.8.a)**. **Table (6.1)** explains the relation between the changes of the magnetostriction step by step with the magnetic field dependence of the ME effect.

To explain the shape of the $M_{ind}(H_{dc})$, **Figure (6.9)** shows the induced magnetic moment signal as a function of external dc magnetic field for the

Tab. 6.1: Relation between dλ/dH and the ME effect

Region/point	dλ/dH	ME effect
AB	Increasing	Increasing
B	Highest	Maximum
BC	Decreasing	Decreasing
D	Small	Zero
After D	Small increase	Change the sign

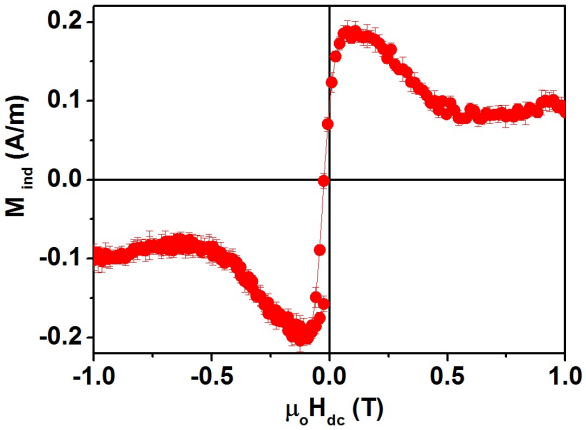

Fig. 6.9: Induced magnetization signal as a function of dc magnetic field for the composite (1-x)$CoFe_2O_4$-x$BaTiO_3$ at x=0.8, T=285K, V_{ac}=100V and f=3Hz

sample composition x=0.8. It is clear by the figure that the sign of the ME effect is positive when applying positive dc magnetic field and negative in the negative one. It is known than the value of longitudinal magnetostriction of cobalt ferrite is negative indicating compressive stress, this stress increases at low field and then decreases at higher dc field. However, the magnetoelectric signal in the longitudinal mode is positive while the strain value (λ) is negative and this can be attributed to the direction of the measured signal inside the SQUID. The same behavior of $M_{ind}(H_{dc})$ was also reported by different authors [103, 104].

6.2.5 Dependence of the converse ME effect on sample orientation

The effect of the sample orientation was also measured and shown in **Figure (6.10)** for longitudinal and transverse modes (**see Figure (2.8)**). The induced magnetization in the longitudinal orientation is larger than the trans-

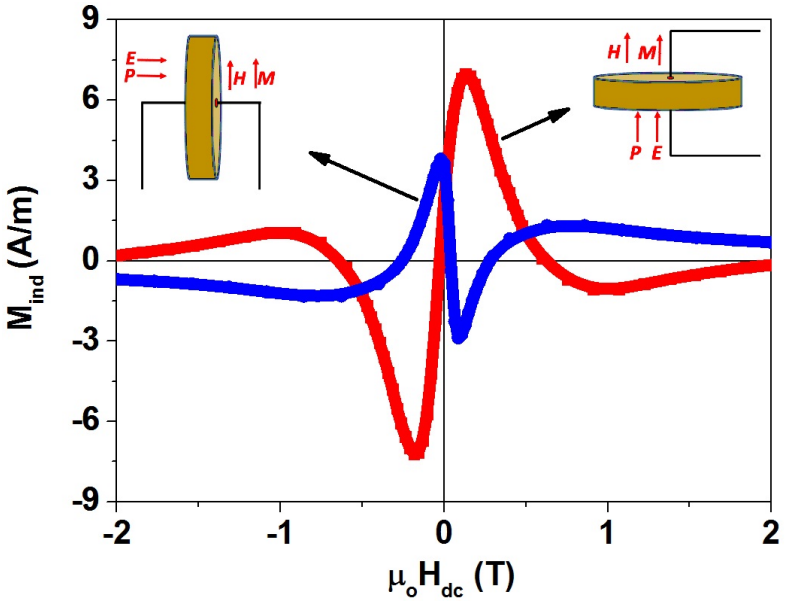

Fig. 6.10: Electrically induced magnetization signal vs H_{dc} showing longitudinal (red) and transverse (blue) response for (1-x)$CoFe_2O_4$-x$BaTiO_3$ [x=0.6] at f=3hz, V_{ac}=200V, T=285K

verse mode which may be attributed to the demagnetization field which is larger in the longitudinal mode case [124]. The maximum value of (α_{31}) is equal to half of (α_{33}).

Another explanation of the behavior for the two curves may be attributed to the magnetostriction values of cobalt ferrite as shown in **Figure (6.11)**. The strain value (λ) mainly depends on the direction of the applied magnetic field and the measuring directions. As I mentioned in **Section (6.5)**, the value of the induced magnetization depends on the piezomagnetic coefficient q_1 which is equal to the (dλ /dH) so that the ME effect tracks the derivative (dλ /dH). For polycrystalline cobalt ferrite, it was also found that the value of longitudinal piezomagnetic coefficient is larger than the transverse one [166] (see **Figure (6.12)**) and the piezomagnetic coefficient and the derivative of the strain with respect to the magnetic field is larger. This explains the shift of the field where the values of α_{33} and α_{31} are maximum .

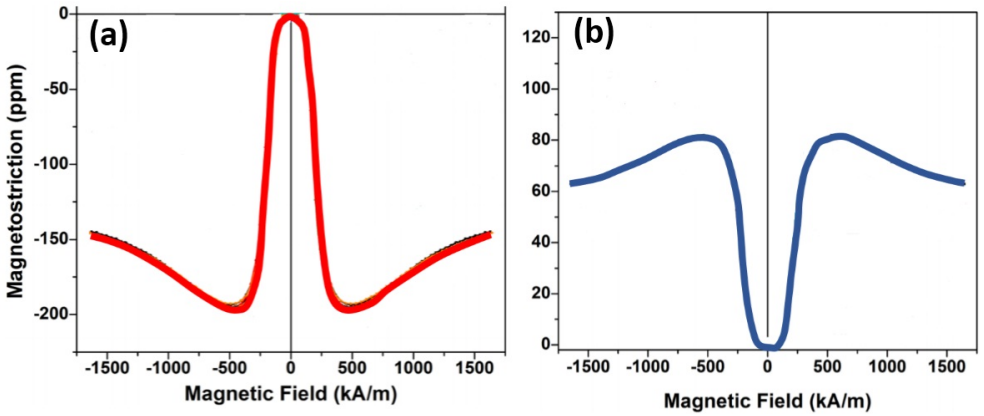

Fig. 6.11: Strain curves of cobalt ferrite showing (a) magnetostriction in longitudinal mode, the magnetic field is perpendicular to the sample surface (b) transverse mode, the magnetic field is parallel to the sample surface [Figure extracted from [166]]

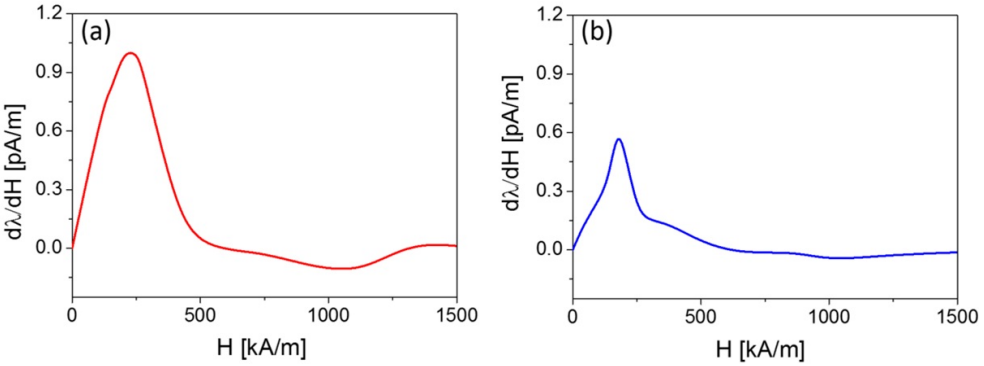

Fig. 6.12: Piezomagnetic coefficient extracted from the magnetostriction curves of (a) longitudinal (b) transverse magnetostriction of $CoFe_2O_4$ [extracted from [166]]

6.3 The effect of the demagnetization factor on the converse ME effect

Referring to **Figure (6.10)** , the shift in magnetic field in which the maximum ME effect occurs can be attributed to the demagnetization field (H_d) inside the sample which can reduce the value of the actual applied field (H). This demagnetization field is proportional to the demagnetization factor (N_d) and the magnetization (M), where

$$H_d = -N_d \cdot M \tag{6.3}$$

and the value of N_d depends on the shape of the sample [167]. For our samples, the demagnetization factor for the magnetization perpendicular and parallel to the sample surface was extracted from tables proposing pure cobalt ferrite cylindrical sample shape [168]. So the applied magnetic field (H) was corrected to the actual true magnetic field (H_T) and shown in **Figure (6.13)**. It is clear that the shift in position of the maximum ME values is due to effect of the demagnetization factor. After correction, the maximum for the two orientations are somehow close to each other. A small shift was detected for the transverse mode, if the transverse curve was shifted so that the remanence induced magnetization is zero at H_{dc}=0, then the two curves will show the maximum at the same dc magnetic field. This shift occurred because of the change of the anisotropy axis of the system (see the inset in **Figure (6.13)**). Laletin et al. observed large remanent magnetoelectric coefficient in the static H dependence of the low frequency ME effects for bilayer lead zirconate titanate (PZT) and a functional grades ferromagnetic layer of $Ni_{0.7}Zn_{0.3}Fe_2O_4$(NZFO) and pure Ni [169]. They attributed the remnant magnetoelectric voltage coefficient to a grading-related magnetization at the Ni-NZFO interface which results in ME coupling at zero dc magnetic field. However, the remnant magnetoelectric effect was reported for the transverse

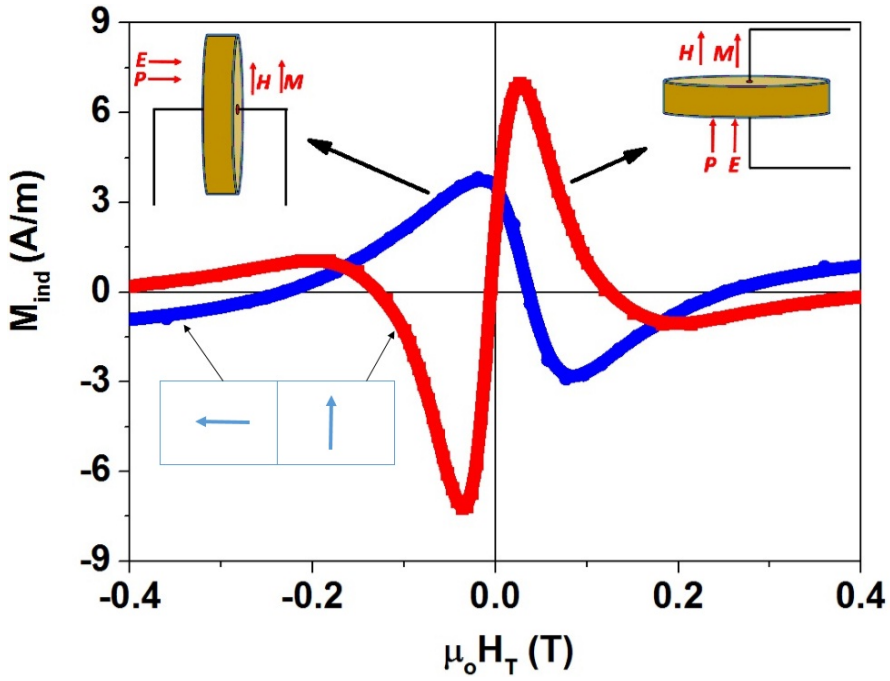

Fig. 6.13: Longitudinal and traverse induced magnetization as a function of true magnetic field after correction to the demagnetization field for (1-x)$CoFe_2O_4$-x$BaTiO_3$ at x=0.6 [at T=285K, f=3Hz, V_{ac} =200V).

mode higher than the longitudinal one and it was related to the higher effective magnetization in the traverse mode [103]. In fact, measuring the effect of demagnetization factor on the magnetoelectric effect is not a trivial issue. In our calculations we proposed that the samples are completely pure ferrimagnets sample, but in reality, the samples contain dispersion of complicated magnetic particles distributed in non-magnetic barium titanate matrix, so that the effective demagnetization factors are much more complicated [170].

6.4 Converse ME effect for (0-3) and (3-0) composites

In order to investigate the effect of the connectivity on the ME effect, two samples were chosen with different connectivities which were described in **Chapter (5)**. The first sample is the annealed SPS sample which has a connectivity of (3-0) and the second sample is the normally sintered sample with connectivity (0-3). For comparison, both samples have 50 percent weight of cobalt iron oxide . **Figure (6.14.a)** shows the amplitude of the magnetoelectrically induced

magnetic moment as function of the superimposed DC magnetic field measured for the annealed SPS ceramic sample and the normal sintered one. They have the shape typical for composite multiferroics with a pronounced peak of the ME response at a certain field. This peak corresponds to the maximal piezomagnetic coefficient, q, which in turn correlates to the maximal change of the magnetostriction with respect to the magnetic field q=dλ/dH [84]. The maximum value of the ME induced magnetization was recorded at μ_oH=0.1T and about μ_oH=0.2T for the SPS annealed sample and the normaly sintered one, respectively. The observed shift of the ME response maximum can be due to the different grain sizes of the $CoFe_2O_4$ in both samples which cause different magnetostriction values [171]. **Figure (6.14.b)** shows the ME induced magnetization as the function of the applied AC voltage. Both samples showed a linear relationship between the induced magnetic moment and the electric field. From the slope of the curves, the value of the converse magnetoelectric coefficient, α_c, can be estimated according to the relation μ_oM=$\alpha_c E_{ac}$, with E_{ac} being the amplitude of the applied AC electric field. The best fit (at $\mu_o H_{dc}$=0.15T) gives α_c = 1 ps/m and 25 ps/m for sample annealed SPS and normally sintered, respectively. We attribute this big difference to the higher resistivity of the (0-3) normally sintered sample compared to the (3-0) connectivity of the annealed SPS sample which facilitates the poling process and hence in enhancement of the piezoelectric effect. Another reason of weaker ME effect is the grain sizes of both cobalt ferrite and barium titanate in the two composites, because of the smaller barium titanate grain sizes(0.65μm) (see **Table (5.1)**) for the (3-0) composite, one can expect a reduction of the piezoelectric coefficient [172] due to the smaller grain size compared to the (0-3) resistive sample with grain size (1-2.5μm) as shown in **Table (5.1)**. Also the smaller grain size of the cobalt ferrite can be a reasons of the smaller piezomagnetic coefficient [171] which will result in a weaker ME effect.

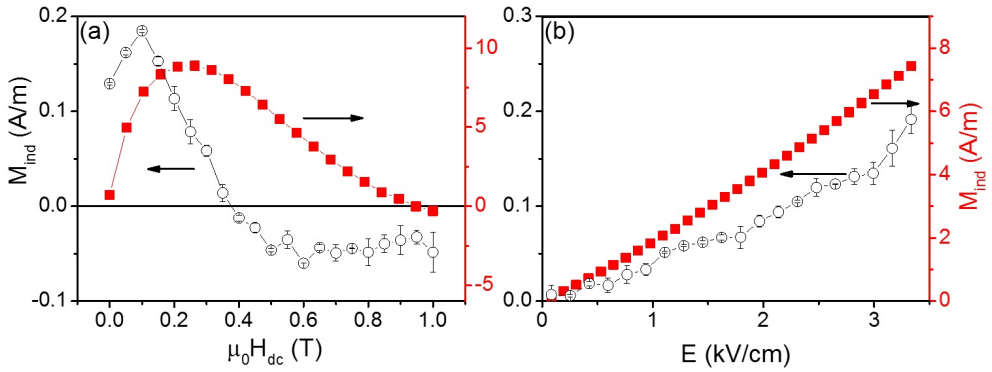

Fig. 6.14: DC magnetic field dependence of the ME induced magnetic moment at T = 285K, V_{ac} = 200 V, and f_{ac} = 3 Hz for samples annealed SPS (open symbols) and normally sintered (closed symbols) (b) AC electric field dependence of the ME induced magnetic moment at T = 285K, $\mu_o H_{dc}$=0.15T, and f_{ac}=3Hz.

6.5 Dependence of the converse ME effect on sample compositions

In order to see the effect of the compositions on the first order ME effect, linear relations between the induced magnetization and the electric field were used in order to calculate the longitudinal converse magnetoelectric coefficient α_c. The coefficients are shown in **Figure (6.15)**. It is clear that the ME effect strongly depends on the composition of the composite. The maximum ME coefficient values were for concentrations around (x=0.5), due to the optimum contact and large interface areas between piezomagnetic and piezoelectric components. It is clear that the values decreased when decreasing both the cobalt ferrite or barium titanate content. The increase of the values with respect to the ferrite contents are related to the much more induced magnetization generated from larger strain values of cobalt ferrite due to stress resulted from barium titanate. Optimum strain can result from the interface interactions between both phases in the composition of x=0.5 where optimum elastic constant for both materials can yield to largest magnetoelectric effect. The maximum measured α_c was 25 ps/m at x=0.5 and low value of about 2 ps/m was recorded for the composition of x=0.8. The low value of the composition of x=0.8 may be attributed to the

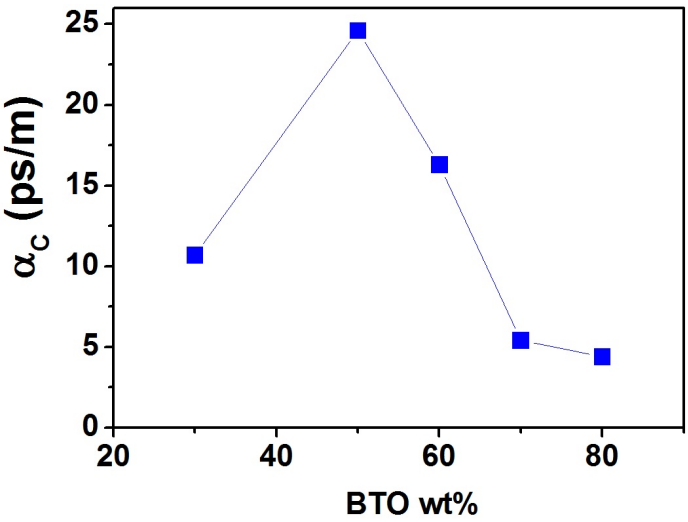

Fig. 6.15: Longitudinal converse ME effect for different compositions measured at T=285K, $\mu_o H_{dc}$=0.15T, f=3Hz

lower amount of cobalt iron oxide that connected to the barium titanate which resulted in less magnetostriction values with respect to the applied stress by the barium titanate phase.

The microstructures shown in **Figure (5.6)** were utilized by Labusch et al. in order to characterize the constitutive behavior of the system by modeling [173]. They used the real SEM micrographs for different samples as shown in **Figure (6.16.a)** and discretized them using quadratic triangular finite elements (see **Figure (6.16.b)**). The regions of cobalt iron oxide are shown in green, and the barium titanate is the yellow matrix. They calculated the ME coupling coefficients by simulating the change in magnetic flux with respect to electric field δB/δE as shown in **Figure (6.16.c)**. The calculated ME coefficients for different compositions are shown in **Figure (6.16.d)**, the values range from 2.1-2.7 ns/m which are larger than the experimental values **Figure (6.15)**. The deviation between the experimental values and the theoretical one can be related to different reasons: first, in modeling it is alway proposed ideal polarization state of the ferroelectric matrix, but in reality it is difficult to ensure full poling of the ME samples, this can reduce the values of coupling. Second, the two dimensional calculations utilized by modeling

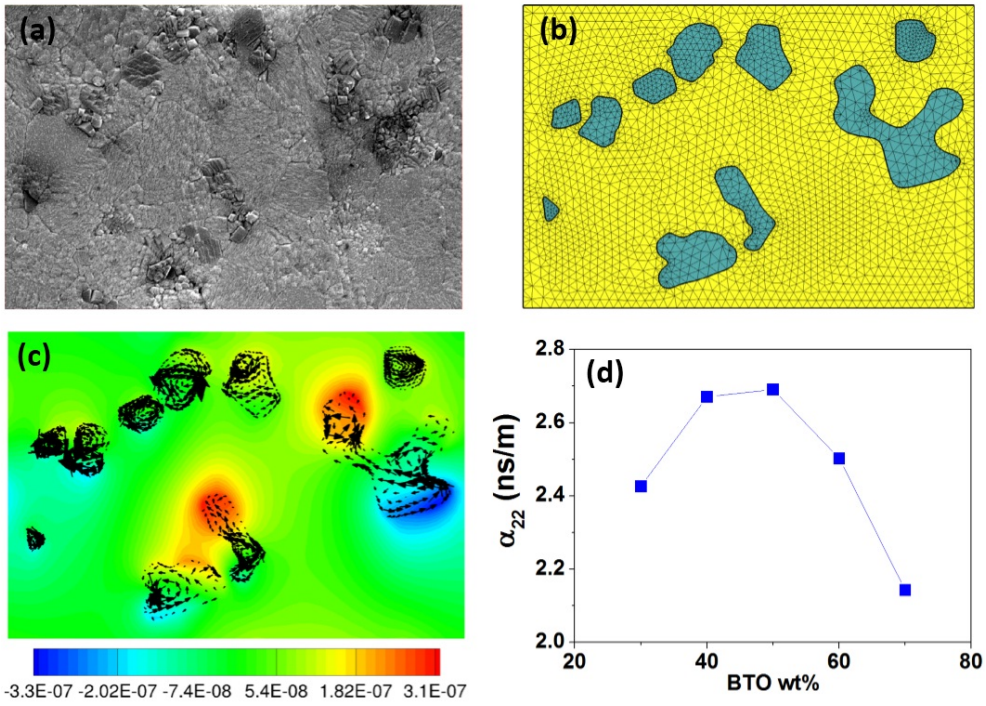

Fig. 6.16: (a) Real microstructure of the sample with x=0.8, (b) the corresponding finite element discretization (c) magnetic potential with magnetic flux density vectors B in the $CoFe_2O_4$ regions when applying electric field 10kV/cm, [simulations by Matthias Labusch], reprinted with permission from Springer [173].

are another source of deviation where it does not represent the real three dimensional structure of the material. Finally, some of the parameters that are usually used in modeling are different in values than the actual measured ones [173].

6.6 Direct ME effect using lock-in technique

Because of the wide application of the direct ME as illustrated in **Figure (1.12)**, a lock-in technique or dynamic method was also used to measure the direct magnetoelectric coupling coefficient α_D for different compositions. The experimental technique was described in detail in **Section (2.10.3)**. In this method the ac voltage generated by the sample when applying a small ac magnetic field was measured. All of the samples showed large dependence of the ME effect on the dc magnetic field as described in **Section (6.2.4)** see

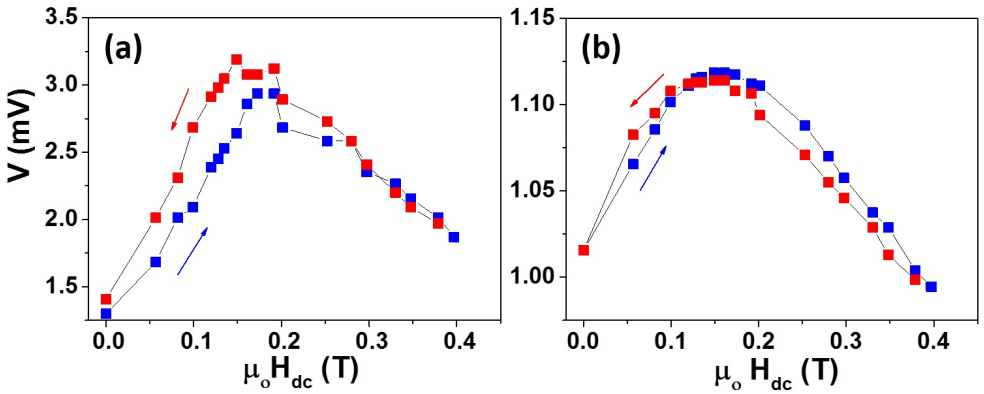

Fig. 6.17: Longitudinal direct ME effect measured by lock-in technique for compositions (a) x=0.5 (b) x=0.8 measured at different dc magnetic field at f=5Hz, T=300K, H_{ac}=18Oe

Figure (6.17). The measurements were done at room temperature with a small ac magnetic field of 18Oe applied perpendicular to the sample surface. The ME effect behavior is approximately linear between 0 and 1.5 kOe dc magnetic field. The same as the converse effect, the maximum magnetoelectric values were recorded in the dc magnetic field (about 1.5-2kOe) as illustrated in **Figure (6.17)** so that we proved here that the maximum ME effect does not occur at the coercive magnetic field for the magnetic phase, but is due to the maximum piezomagnetic coefficient, (as described in the previous sections). The effect then decreased until reaching lower values at dc magnetic field larger than 4 kOe. The peak output was measured for the composition x=0.5 which was about 3.25 mV at 18 Oe ac magnetic field and at 2kOe dc bias which is equivalent to the magnetoelectric coupling coefficient α_E=3 mV/cm·Oe. On the other hand, the composition of x=0.8 showed the lowest produced voltage and the ME coefficient was measured to be in the range of α_E=1 mV/cm·Oe.

6.7 Inequivalence between direct and converse ME values

For conversion between the direct and the converse ME effect, **Equation (1.11)** for single phase materials can be used after determining the permittivity value of the ME material. In this equation, the single domain value of the dielectric permittivity at a certain frequency is used. For my composite,

I used the same equation in order to extract direct magnetoelectric coupling coefficient from the converse one. The results are shown in **Table (6.2)**. The maximum and minimum estimated direct ME coefficients 29.9 and 1.0 mV/cm·Oe were recorded for the compositions of x=0.5 and x=0.8, respectively. The maximum value is comparable to those reported for the barium titanate cobalt ferrite system in references [104, 126, 152]. As shown in **Table (6.2)**, the values of the estimated direct magnetoelectric coefficient for all compositions are different than the measured one, e.g. in case of x=0.5, the estimated value is 10 times larger. The same ME coupling coefficient was recorded only for the composition with x=0.8. I attribute the difference in the coefficient values at higher amount of cobalt ferrite to the conductivity which is increased and affects the magnetoelectric values at low frequency. The values of permittivity may contain relaxation due to the conductivity, usually at low frequencies, the permittivity values for composites are influenced by relaxation as shown in **Figure (5.10)**. In the calculation, I assumed that the relaxation due to the conductivity is minimized at higher frequency so that the estimated values were calculated depending on the permittivity values at 1MHz and at room temperature. However, the difference between the two values may also come from the discharging process which may occur due to the conductivity of the samples. This process is more effective in the direct measurement which explains the lower values of the measured direct effect. Lou et al. measured the effective converse ($\mu_o dm/dE$) and the direct (dp/dH) magnetoelectric effects, they used the lowercase letters to denote the effective electric dipole moment p and the effective magnetic moment m. They utilized a current to voltage converter with lock-in technique and vibrating sample magnetometer to measure the effective electrical and magnetic dipole moments, respectively. The direct and the converse coefficients were found to be equal when measuring the effective polarization and the effective magnetization so that the variables should be parameterized to describe the entire

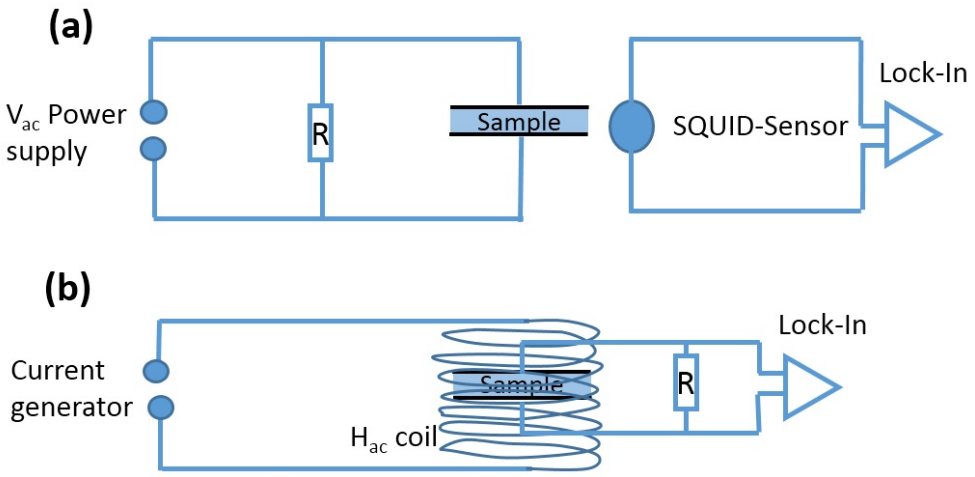

Fig. 6.18: Equivalent circuit of measuring magnetoelectric effect showing (a) converse method using SQUID (b) direct method using lock-in technique.

system [174].

In our case the measurements were done by measuring the magnetic moment in the converse effect case and the voltage in the case of direct effect one, this can also explain the difference in values. For example in case of (0-3) composites where the magnetic regions are distributed in a ferroelectric matrix, the applied magnetic field on the composite produced a strain in the magnetostrictive phase because of magnetostriction. This causes elastic interaction between the magnetostrictive and the ferroelectric phase in terms of stress. The stress and strain in the ferroelectric phase induce polarization through the piezoelectric effect and then generate a signal in terms or charges. If the magnetic inclusions are not well-distributed in the matrix, this can reduce the produced voltage. It should be mentioned here that for the converse magnetoelectric effect, the electric power supply can compensate the ohmic losses and still achieve sufficient electric fields to generate the magnetic signal, but in case of measuring the direct effect (voltage produced by magnetic field) is difficult to measure for non-resistive samples, because the leakage will reduced the effectively measured voltage and the leakage current may partly short circuit the sample (see **Figure (6.18)**). The experimental setup, electrodes, leakage currents can also affect the ME measurements [55]. Also, other

authors reported significant differences in values between both the direct and the converse magnetoelectric effect [175–177].

Tab. 6.2: Converse, direct and converted ME effect for different (1-x)$CoFe_2O_4$-x$BaTiO_3$ compositions

Sample	Measured α_c ps/m	RT ϵ at 1MHz	Convert α_c to mV/cm·Oe	Measured α_D mV/cm·Oe
x=0.3	10.7	137	7.1	1.7
x=0.5	23	70	29.9	3.2
x=0.6	16.3	190	7.8	3.1
x=0.7	5.4	130	3.8	2.3
x=0.8	4.4	410	1.0	1.0

6.8 Dichroic X-ray absorption of $CoFe_2O_4$-$BaTiO_3$ ceramic magnetoelectric composite

It was shown before, that the X-ray absorption spectroscopy and the x-ray linear dichroism (XLD) at the Ti $L_{3,2}$ absorption edges is a tool to study the magnetic field-dependent electric polarization [131]. For this purpose, two samples were chosen for the XLD investigations: the annealed SPS and the normally sintered sample. Both samples contain 50 weight percent of cobalt ferrite. The measurement procedure was explained in **Section (2.11)** and reported in detail in refs [131, 178].

The X-ray absorption near-edge structure (XANES) and XLD at the Ti $L_{3,2}$ absorption edges are shown in **Figure (6.19)** for the annealed SPS and the normally sintered samples. The measurements were done under different values of magnetic field 0.15T and 1T. Four peaks were detected in the spectrum for both samples, two at the L_3 absorption edge and two at the L_2 absorption edge. This reflects the crystal field splitting of the final 3d states. Two small peaks at photon energies 456 eV and 458 eV are related to the $2P^6 3d^0 2P5^3 d^1$ transition. XANES of the SPS annealed sample indicates the typical bulk like $BaTiO_3$ structure at a room temperature. While in the case of the normally sintered sample, it shows significant deviation probably correlated to a more

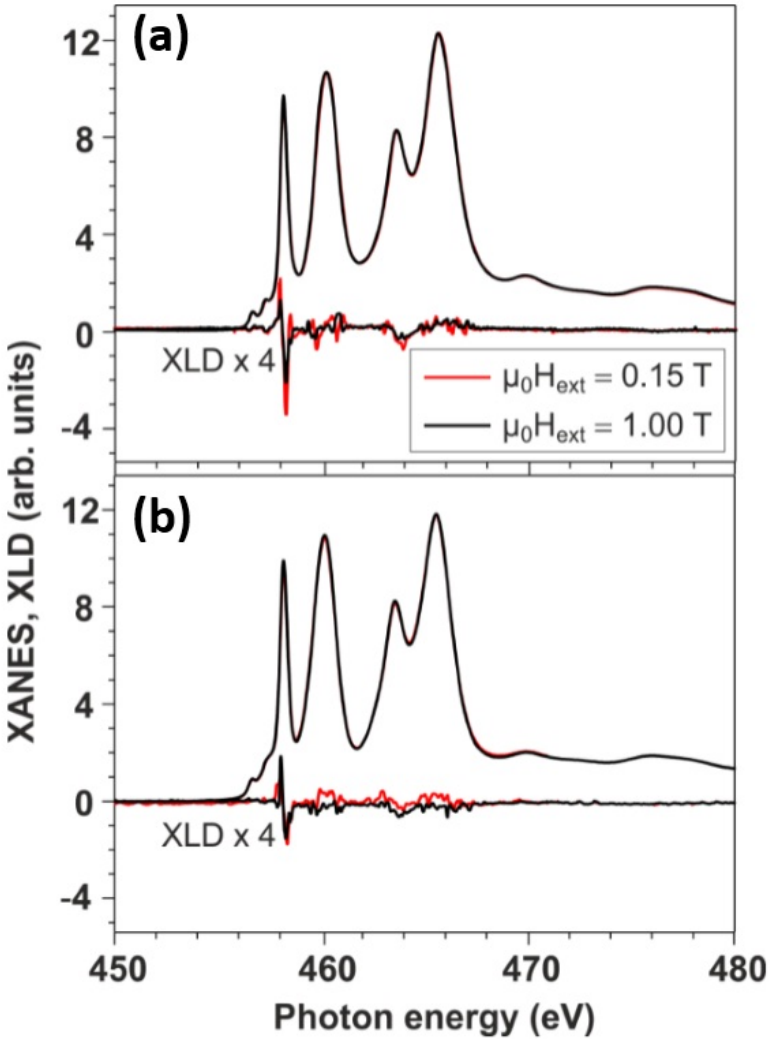

Fig. 6.19: XANES and XLD at the Ti $L_{3,2}$ absorption edges of samples (a) annealed SPS sample (b) normally sintered sample, for two different values of external magnetic field. Measurement were performed at a temperature of 290K [image by C. Schmitz-Antoniak] [178].

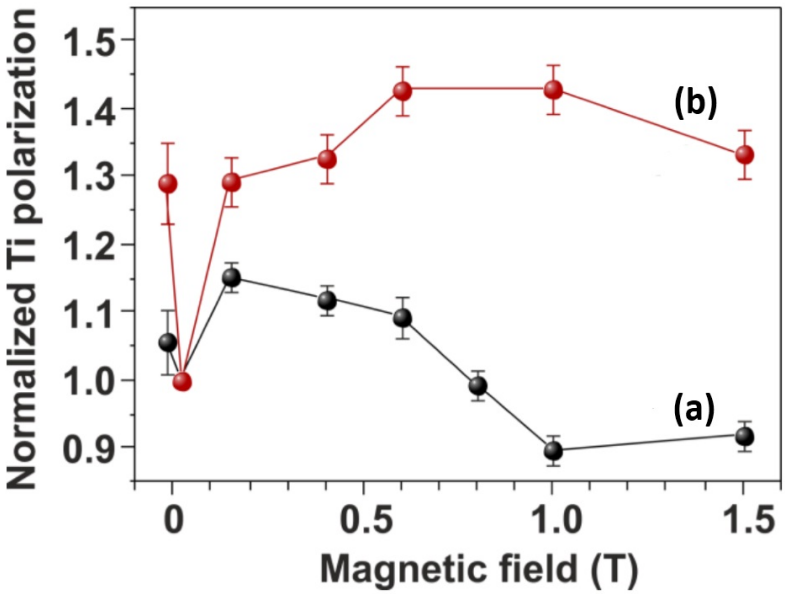

Fig. 6.20: Magnetic field dependence of electric polarization as extracted from XLD measurement at the Ti $L_{3,2}$ absorption edges for (a) annealed SPS sample (b) normally sintered sample at temperature 290K [image by C. Schmitz-Antoniak] [178].

covalent character of the bondings of Ti ions to their neighboring ions.

Figure (6.20) shows the magnetic field dependence of the square root of XLD amplitude which is a measure of the electric polarization according to [179]:

$$I = (1 - cos^2\theta_{P,E})\langle P^2 \rangle \tag{6.4}$$

where $\theta_{P,E}$ represents the angle between the electric field vector of X-rays and the electric polarization of the sample. Assuming that the electric polarization is either parallel or perpendicular to the magnetic field applied, the difference between the absorption signals for horizontally and vertically polarized X-rays is proportional to the statistical average of the squared local polarization. The data were normalized to the value obtained in a small magnetic field of 0.02 T. The XLD asymmetries used for the normalization are 2.8% for the SPS annealed sample, which is close to the asymmetry reported for epitaxial $CoFe_2O_4$-$BaTiO_3$ nanocomposites with an oriented c-axis perpen-

dicular to the sample surface (2.2%) [131] and 1.1% for the normally annealed sample. The different values for the XLD asymmetry correspond to a larger electric polarization of the annealed SPS sample with respect to the normally sintered one. For the SPS annealed sample, the maximum polarization is obtained at $\mu_o H_{ext} = 0.15$T and decreases with further increasing value of the magnetic field until it reaches a minimum at about 1.0T. For higher magnetic fields, it is again slightly increasing following the shape of a typical magnetostriction curve of $CoFe_2O_4$ [171, 180]. Interestingly, for large magnetic fields, the polarization is reduced to only about 90% of the value at very low magnetic fields. This may be explained in a simplistic picture by the compression of the $BaTiO_3$ grains in the $CoFe_2O_4$ matrix along the field direction due to the negative magnetostriction of $CoFe_2O_4$ along the magnetic field direction whose absolute value is twice as large as the positive magnetostriction in the sample plane yielding a smaller tetragonal distortion of the $BaTiO_3$ unit cell.

For the normally annealed sample, the maximum polarization is obtained between 0.5 T and 1.0T and is again slightly decreasing for further increasing external magnetic fields. In contrast to the annealed SPS sample, the polarization at high magnetic fields is always larger than the one at the lowest field of 0.02T. This can be explained in the same simplistic picture by the different connectivity (see **Chapter (5)**). In the annealed SPS sample, the $CoFe_2O_4$ matrix compresses the $BaTiO_3$ grains in a way that the unit cell becomes more cubic. The normally annealed sample, the grains shrink along the field direction and expand in the perpendicular directions forcing a larger tetragonal distortion of the $BaTiO_3$ unit cell with its long axis parallel to the applied magnetic field.

To compare the magnetic field dependence of the electric polarization obtained from XLD with measurements of the electrically induced magnetization using ac-SQUID susceptometry, one has to take into account that in the first case the *integral* magnetoelectric effect is measured, while in the second case

the *differential* ME response is probed. The XLD signal tracks the magnetic field induced strain, i.e. the field dependence of the magnetostriction. While, the electrically induced magnetization is $M_{ME} \simeq q_l d_l \mathrm{E}$ where E is weak probing electric field, d_l is the piezoelectric coefficient of the ferroelectric phase, and q_l is a piezomagnetic coefficient of the magnetic phase [177]. The latter can be defined as $q_l = \mathrm{d}\lambda/\mathrm{dH}$, where λ is the magnetostriction [181]. Thus, the magnetic field dependence of the ME effect measured by SQUID (**Figure 6.14**) should behave as a derivative of magnetic field dependence measured by XLD (**Figure (6.20)**). Indeed, for the annealed SPS sample, we observe that Ti polarization reaches the maximum at approximately 0.3 T and then decreases. This behavior well matches the change of the sign of the ME response by the SQUID measurements. For the normally annealed sample, the XLD signal is saturated around 1 T, correspondingly the ME induced magnetization drops to zero.

7. CONCLUSIONS AND FINAL REMARKS

7.1 Conclusions

This dissertation aims to give a better understanding of the ME effect in biphasic composites and the relation between the ME effect, microstructure, compositions, and magnetic and electrical properties. As a conclusion, I can say that I have successfully synthesized magnetoelectric composites with different fractions of barium titanate and cobalt ferrite and I believe that the following points are successfully achieved.

- I showed that cobalt iron oxide nanoparticles with particle sizes distribution 22-40 nm can be synthesized by the co-precipitation method. The particle sizes mainly depended on the amount of precipitation agent. I also decreased the degree of agglomeration of magnetic particles by controlling the process of milling and sonification. The sufficiently low agglomeration of the particles, made the particles a great candidate for fabrication of multiferroic magnetoelectric core shell nanoparticles. Indeed the complete separation of the particles is difficult to achieve, because of the tendency of magnetic particles to agglomerate due to the magnetic attractive forces. The magnetic behavior of the cobalt iron oxide nanoparticles is very close to superparamagnetic behavior with low coercive field and remnant polarization. Smaller cobalt iron oxide particle sizes are needed in order to have fully superparamagnetic behavior. However I highlighted that all of the magnetic properties and parameters of $CoFe_2O_4$ depend on the particle or grain sizes.

- I have combined the co-precipitation method to prepare $CoFe_2O_4$ with the organosol method to synthesize a core shell structure. Because the surface modification of the cobalt iron oxide particles is the main step in forming the core shell structure, stable hydrophobic $CoFe_2O_4$ nanoparticles in ferrofluid were successfully prepared and added to the $BaTiO_3$ organosol precursor. I have changed the mass content of cobalt ferrite in order to investigate the effect of composition on the ME properties. TEM and SEM confirmed the formation of some core shell structure with 40nm $CoFe_2O_4$ cores surround by 40nm shells of $BaTiO_3$. Mössbauer data show that the magnetic properties of the composite nanopowder are similar to those of pure cobalt iron oxide nanoparticles. The core shell nanoparticles showed similar magnetic behavior of cobalt ferrite nanoparticles which is close to superparamagnetism. For these core-shell nanoparticles, I found that there was no direct effect of barium titanate existence on the magnetic properties of the cobalt ferrite. On the other hand, the ferroelectriciy of barium titanate was not proven for the nanopowder due to small particle size. The cubic structure of barium titanate nanopowder was shown by x-ray diffraction and confirmed by dielectric spectroscopy and PFM. Compacting $CoFe_2O_4$-$BaTiO_3$ powder in order to have nanostructured core-shell composites is still a big challenge because of the high porosity. High leakage current in this case prevents poling and magnetoelectric measurements.

- Because the ferroelectricity of $BaTiO_3$ was not proven for the core shell nanopowder and because the ME effect mainly depends on the microstructure, I have improved the microstructure using different sintering methods. To achieve that, two sintering routes (SPS and conventional sintering) were followed in order to have different kinds of ceramic connectivities. Stable (0-3) and (3-0) composites have been synthesized by conventional and spark plasma sintering methods, respectively. The (0-

3) composite shows a good distribution of cobalt iron oxide magnetic regions in the barium titanate matrix forming highly resistive samples. The SPS technique kept the structure on the nano scale. Comparing to (0-3) samples, (3-0) showed higher conductivity due to the leakage current passing through the sample due to the semiconductor character of the $CoFe_2O_4$ matrix. Also, the paraelectric-ferroelectric phase transition of $BaTiO_3$ was affected by the existence of $CoFe_2O_4$ in the composites. Because having highly resistive ME samples is important for enhancing ME effect, I produced samples with high resistance and this improved the poling process and consequently enlarged the ME effect.

- I have proven that the poling process affects ME coupling. The depoled samples show very weak induced magnetization by an electric field. On the other hand, the poled samples show perfectly linear ME effect due to the enhancement of piezoelectricity by poling. The largest ME coefficient (25 ps/m) was recorded for the composition x=0.5. We related this value to the proper amount of cobalt iron oxide inclusions distributed in fine grains of $BaTiO_3$ matrix and the isolating properties. The maximum estimated direct ME effect was recorded for the composition of x=0.5 with a value of about 30 mV/cm·Oe. I also studied the effect of the dc magnetic field and the temperature on the ME effect. The samples showed typical α vs. H_{dc} behaviour with a pronounced peak of the magnetoelectric response at a certain field. This peak corresponds to the maximal piezomagnetic coefficient q. Another important point that I have notified, the temperature dependence of ME effect tracks the permittivity dependence of temperature so that the maximum ME effect was measured at T=285 K which is the phase transition of barium titanate from orthorhombic to the tetragonal phase. In the dependence of of ME effect on the dc magnetic field, it was concluded that the demagnetization field correction is very important in order to estimate the

effective magnetic field in the sample. I found that the maximum ME effect for longitudinal and traverse effect happens at the same dc magnetic field after subtracting the demagnetization field. In the sample orientation I found that the value of longitudinal converse ME effect is two times larger than the transverse one and that is related to the longitudinal piezomagnetic coefficient of cobalt ferrite which is larger than the traverse one.

- I have designed a custom-built ME measurement setup utilizing the lock-In technique for measuring the direct ME effect. Like for the converse effect, linear relations were measured between the applied magnetic field and the produced voltage. I found that the maximum value of direct ME coefficient 3.2 mV/cm·Oe was recorded for the composition x=0.5 from the direct ME measurement. This value is lower than the estimated one by a factor of 10. For different compositions, the measured values of the direct ME effect are much lower than the estimated one (derived from the converse effect). I related the differences to different factors such as, the dielectric permittivity values that should be used during the conversion, and the conductivity contribution which decrease the apparent values of the measured ME effect.

- The magnetic field dependence of electric polarization at the surface was investigated for two connectivity schemes (0-3) and (3-0) composites. This was done using the X-ray absorption spectroscopy and its associated linear and circular dichroisms. In spite of relatively high leakage current for the (3-0) composite, it exhibits small converse ME effect measured by SQUID but larger electric polarization measured by XLD asymmetry experiment. Comparison of both methods revealed that the magnetic field dependence of the electric polarization obtained by XLD is the measured of integral magnetoelectric effect, but in case of ac-SQUID susceptometer, the differential ME response is probed.

7.2 Recommendations and future works

According to the magnificent ME properties for such composites and with respect to the outcomes, there are always chances to enhance the ME effect by synthesizing different microstructures and thinking about different new connectivities that improve the properties and hence convert to useful ME technological devices. Going to the nanoscale in composites is still a challenge and still needs more investigations. The SPS techniques is an option in the future to keep the nanoscale in dense ceramics so that the door is still open for more investigation in order to fabricate an ideal core shell structure. This can be done by developing new chemical methods that can decrease the degree of agglomeration which is the key factor for perfect core shell structure synthesis. However, different shell and core thicknesses will produce new properties and effects. In reality and for ME measurement, the electric field is a highly heterogeneous matter. The type of electrodes used strongly affect the homogeneity of the applied electric field. This can be improved by using sputtered electrodes. However, the effect of calcination and sintering temperature and time and the effect of sample thickness on the ME effect should be taken into consideration in the future. In the measurement methods of the ME effect, the comparison and the relation between the converse and the direct effect should be investigated as well as the effect of frequency and temperature. Indeed the effect of different orientations of magnetic field, electrical field, and the sample position on the ME effect still need more investigation. However, the direct ME effect needs to be optimized and different structures rather than the core shell can be also applied. Comparing experimental values with the theoretical ones for the same microstructures, one can notify that the theoretical values are still not yet achieved so that more efforts should be put to improve the microstructure and reach optimized (0-3) composites.

Bibliography

[1] R. Ramesh and Nicola A. Spaldin. Multiferroics: progress and prospects in thin films. *Nature Materials*, 6(1):21–29, 2007.

[2] W. Eerenstein, N.D. Mathur, and J.F. Scott. Multiferroic and magnetoelectric materials. *Nature*, 442(7104):759–765, 2006.

[3] Y.K. Fetisov, D.A. Burdin, D.V. Chashin, and N.A. Ekonomov. High-sensitivity wideband magnetic field sensor using nonlinear resonance magnetoelectric effect. *Sensors Journal, IEEE*, 14(7):2252–2256, 2014.

[4] J. Zhai, S. Dong, Z. Xing, J. Li, and D. Viehland. Geomagnetic sensor based on giant magnetoelectric effect. *Applied Physics Letters*, 91(12):123513, 2007.

[5] S. Dong, J.-F. Li, and D. Viehland. Vortex magnetic field sensor based on ring-type magnetoelectric laminate. *Applied Physics Letters*, 85(12):2307–2309, 2004.

[6] Y. Jia, A. Xue, Z. Zhou, Z. Wu, J. Chen, K. Ma, Y. Zhang, J. Zhou, Y. Wang, and H. L. W. Chan. Magnetostrictive/piezoelectric drum magnetoelectric transducer for H_2 detection. *International Journal of Hydrogen Energy*, 38(34):14915–14919, 2013.

[7] C.M. Leung, S.W. Or, and S.L. Ho. Direct current force sensing device based on compressive spring, permanent magnet, and coil-wound magnetostrictive/piezoelectric laminate. *Review of Scientific Instruments*, 84(12):125003, 2013.

[8] S. Dong, J.F. Li, D. Viehland, J. Cheng, and L.E. Cross. A strong magnetoelectric voltage gain effect in magnetostrictive-piezoelectric composite. *Applied Physics Letters*, 85(16):3534–3536, 2004.

[9] S. Dong, J. Zhai, J. Li, and D. Viehland. Near-ideal magnetoelectricity in high-permeability magnetostrictive/piezofiber laminates with a (2-1) connectivity. *Applied Physics Letters*, 89(25):252904, 2006.

[10] T.-D. Onuta, Y. Wang, C.J. Long, and I. Takeuchi. Energy harvesting properties of all-thin-film multiferroic cantilevers. *Applied Physics Letters*, 99(20):203506, 2011.

[11] N. D'Souza, J. Atulasimha, and S. Bandyopadhyay. Four-state nanomagnetic logic using multiferroics. *Journal of Physics D: Applied Physics*, 44(26):265001, 2011.

[12] J.-M. Hu, Z. Li, L.-Q. Chen, and C.-W. Nan. High-density magnetoresistive random access memory operating at ultralow voltage at room temperature. *Nature Communications*, 2, 2011.

[13] C. Pettiford, S. Dasgupta, L. Jin, S.D. Yoon, and N.X. Sun. Bias field effects on microwave frequency behavior of PZT/YIG magnetoelectric bilayer. *Magnetics, IEEE Transactions on*, 43(7):3343–3345, 2007.

[14] J. Lou, D. Reed, M. Liu, and N.X. Sun. Electrostatically tunable magnetoelectric inductors with large inductance tunability. *Applied Physics Letters*, 94(11):112508, 2009.

[15] M. Vopsaroiu, J. Blackburn, and M. G. Cain. A new magnetic recording read head technology based on the magneto-electric effect. *Journal of Physics D: Applied Physics*, 40(17):5027, 2007.

[16] Y. Tokura. Multiferroics-toward strong coupling between magnetization and polarization in a solid. *Journal of Magnetism and Magnetic*

Materials, 310(2, Part 2):1145–1150, 2007. Proceedings of the 17th International Conference on Magnetism The International Conference on Magnetism.

[17] J. Ryu, A.V. Carazo, K. Uchino, and H.-E. Kim. Magnetoelectric properties in piezoelectric and magnetostrictive laminate composites. *Japanese Journal of Applied Physics*, 40(8R):4948, 2001.

[18] D. N. Astrov. The magnetoelectric effect in antiferromangetics. *Soviet Physics, Journal of Experimental and Theoretical Physics*, 11:708–709, 1960.

[19] H. Schmid. Multi-ferroic magnetoelectrics. *Ferroelectrics*, 162(1):317–338, 1994.

[20] M. Bibes. Nanoferronics is a winning combination. *Nature Materials*, 11(5):354–357, 2012.

[21] G. Catalan and J. F. Scott. Physics and applications of bismuth ferrite. *Advanced Materials*, 21(24):2463–2485, 2009.

[22] S. Dong and J.-M. Liu. Recent progress of multiferroic perovskite manganites. *Modern Physics Letters B*, 26(09):1230004, 2012.

[23] D. Khomskii. Classifying multiferroics: Mechanisms and effects. *Physics*, 2:20, 2009.

[24] J. V. D. Boomgaard, D.R. Terrell, R. A. J. Born, and H. F. J. I Giller. An in situ grown eutectic magnetoelectric composite material. *Journal of Materials Science*, 9(10):1705–1709, 1974.

[25] J. Zhai, N. Cai, Z. Shi, Y. Lin, and C.-W. Nan. Magnetic-dielectric properties of $NiFe_2O_4$ /PZT particulate composites. *Journal of Physics D: Applied Physics*, 37(6):823, 2004.

[26] M. Ziese, A. Bollero, I. Panagiotopoulos, and N. Moutis. Magnetoresistance switch effect in a multiferroic Fe_3O_4-Ba$TiO3$ bilayer. *Applied Physics Letters*, 88(21):212502, 2006.

[27] Y.G. Ma, W.N. Cheng, M. Ning, and C.K. Ong. Magnetoelectric effect in epitaxial $Pb(Zr_{0.52}Ti_{0.48})O_3$-$La_{0.7}Sr_{0.3}MnO_3$ composite thin film. *Applied Physics Letters*, 90(15):152911, 2007.

[28] J.F. Scott. Applications of magnetoelectrics. *Journal of Materials Chemistry*, 22:4567–4574, 2012.

[29] Martin Gajek, Manuel Bibes, Stephane Fusil, Karim Bouzehouane, Josep Fontcuberta, Agnes Barthelemy, and Albert Fert. Tunnel junctions with multiferroic barriers. *Nature Materials*, 6(4):296–302, 2007.

[30] E.Y. Tsymbal, A. Gruverman, V. Garcia, M. Bibes, and A. Barthélémy. Ferroelectric and multiferroic tunnel junctions. *MRS Bulletin*, 37:138–143, 2012.

[31] C. Kittel. *Introduction to solid state physics*. John Wiley and Sons, Inc., 1986.

[32] J. Valasek. Piezo-electric and allied phenomena in rochelle salt. *Physical Review B*, 17:475–481, 1921.

[33] F. Jona and G.Shirane. *Ferroelectric crystals*. Dover Publications, inc, New York, 1993.

[34] C.B. Sawyer and C.H. Tower. Rochelle salt as a dielectric. *Physical Review*, 35:269–273, 1930.

[35] B. Jaffe, W. R. Cook Jr., and H. Jaffe. *Piezoelectric ceramics*. Academic Press Limited, 1971.

[36] R.E. Newnham. *Properties of materials, anisotropy, symmetry, structure*. Oxford university press Inc., New York, 2005.

[37] K. Uchino. *Piezoelectric Actuators and Ultrasonic Motors*. Kluwer academic, 1996.

[38] P. Curie. Sur la symétrie dans les phénoménes physiques, symétrie d'un champ électrique et d'un champ magnétique. *Journal of Theoretical Applied Physics*, 3(1):393–415, 1894.

[39] P. Debye. Bemerkung zu einigen neuen versuchen über einen magnetoelektrischen richteffekt. *Zeitschrift für Physik*, 36(4):300–301, 1926.

[40] N.A. Spaldin and M. Fiebig. The renaissance of magnetoelectric multiferroics. *Science*, 309(5733):391–392, 2005.

[41] W.C. Röntgen. über die durch bewegung eines im homogenen electrischen felde befindlichen dielectricums hervorgerufene electrodynamische kraft. *Annalen der Physik*, 271(10):264–270, 1888.

[42] H. Wilson. On the electric effect of rotating a dielectric in a magnetic field. *Philosophical Transactions of the Royal Society of London*, 204:121–137, 1905.

[43] G.T. Rado and V.J. Folen. Observation of the magnetically induced magnetoelectric effect and evidence for antiferromagnetic domains. *Physical Review Letters*, 7:310–311, 1961.

[44] V.J. Folen, G.T. Rado, and E.W. Stalder. Anisotropy of the magnetoelectric effect in Cr_2O_3. *Physical Review Letters*, 6:607–608, 1961.

[45] T. Kimura, T. Goto, H. Shintani, K. Ishizaka, T. Arima, and Y. Tokura. Magnetic control of ferroelectric polarization. *Nature*, 426(6962):55–58, 2003.

[46] M. Fiebig. Revival of the magnetoelectric effect. *Journal of Physics D: Applied Physics*, 38(8):R123, 2005.

[47] C.-W. Nan, M.I. Bichurin, S. Dong, D. Viehland, and G. Srinivasan. Multiferroic magnetoelectric composites: Historical perspective, status, and future directions. *Journal of Applied Physics*, 103(3):031101, 2008.

[48] J. Ma, J. Hu, Z. Li, and C.-W. Nan. Recent progress in multiferroic magnetoelectric composites: from bulk to thin films. *Advanced Materials*, 23(9):1062–1087, 2011.

[49] A. Perrier and A. J. Staring. *Archives des Sciences Physiques et Naturelles*, 4:373–382, 1922.

[50] A. Perrier and A. J. Staring. *Archives des Sciences Physiques et Naturelles*, 5:333–360, 1923.

[51] I. E. Dzyaloshinskii. On the magnetoelectrical effect in antiferromagnetics. *Soviet Physics, Journal of Experimental and Theoretical Physics*, 10:628–629, 1960.

[52] L.D. Landau and E.M. Lifshitz. *Electrodynamics of continuous Media*, volume 8. Pergamon Press, 1960.

[53] B. I. AlSHIN and D. N. Astrov. Magnetoelectric effect in titanium oxide Ti_20_3. *Soviet Physics, Journal of Experimental and Theoretical Physics*, 17(4):809–811, 1963.

[54] G.T. Rado. Observation and possible mechanisms of magnetoelectric effects in a ferromagnet. *Physical Review Letters*, 13:335–337, 1964.

[55] D. C. Lupascu, H. Wende, M. Etier, A. Nazrabi, I. Anusca, H. Trivedi, V. V. Shvartsman, J. Landers, S. Salamon, and C. Schmitz-Antoniak. Measuring the magnetoelectric effect across scales. *GAMM Mitteilungen*, 38(1):25–74, 2015.

[56] J. F. Nye. *Physical Properties of crystals*. Oxford university press Inc., New York, 1985.

[57] J.-P. Rivera. On definitions, units, measurements, tensor forms of the linear magnetoelectric effect and on a new dynamic method applied to Cr-Cl boracite. *Ferroelectrics*, 161(1):165–180, 1994.

[58] W. F. Brown, R.M. Hornreich, and S. Shtrikman. Upper bound on the magnetoelectric susceptibility. *Physical Review*, 168:574–577, 1968.

[59] G.T. Rado, J.M. Ferrari, and W.G. Maisch. Magnetoelectric susceptibility and magnetic symmetry of magnetoelectrically annealed $TbPO_4$. *Physical Review B*, 29:4041–4048, 1984.

[60] D. N. Astrov. Magnetoelectric effect in antiferromagnetic Cr_2O_3. *Soviet Physics, Journal of Experimental and Theoretical Physics*, 13:729–733, 1961.

[61] Y. F. Popov, A.M. Kadomtseva, G.P. Vorob'ev, V.A. Timofeeva, M.-M. Tehranchi, and A.K. Zvezdin. Linear magnetostriction and magnetoelectric effect in piezoelectric $Ga_{2-x}Fe_xO_3$. *Ferroelectrics*, 204(1):269–277, 1997.

[62] R. V. Chopdekar and Y. Suzuki. Magnetoelectric coupling in epitaxial $CoFe_2O_4$ on $BaTiO_3$. *Applied Physics Letters*, 89(18):182506, 2006.

[63] Y. Zhang, C. Deng, J. Ma, Y. Lin, and C.-W. Nan. Enhancement in magnetoelectric response in $CoFe_2O_4$-$BaTiO_3$ heterostructure. *Applied Physics Letters*, 92(6):062911, 2008.

[64] M. I. Bichurin, D. A. Filippov, V. M. Petrov, V. M. Laletsin, N. Paddubnaya, and G. Srinivasan. Resonance magnetoelectric effects in layered magnetostrictive-piezoelectric composites. *Physical Review B*, 68:132408, 2003.

[65] S. Lopatin, I. Lopatina, and I. Lisnevskaya. Magnetoelectric PZT/ferrite composite material. *Ferroelectrics*, 162(1):63–68, 1994.

[66] G. Liu, C.-W. Nan, and J. Sun. Coupling interaction in nanostructured piezoelectric/magnetostrictive multiferroic complex films. *Acta Materialia*, 54(4):917–925, 2006.

[67] H. Zheng, J. Wang, S.E. Lofland, Z. Ma, L. Mohaddes-Ardabili, T. Zhao, L. Salamanca-Riba, S.R. Shinde, S.B. Ogale, F. Bai, D. Viehland, Y. Jia, D.G. Schlom, M. Wuttig, A. Roytburd, and R. Ramesh. Multiferroic $CoFe_2O_4$-$BaTiO_3$ nanostructures. *Science*, 303(5658):661–663, 2004.

[68] J. Li, I. Levin, J. Slutsker, V. Provenzano, P.K. Schenck, R. Ramesh, J. Ouyang, and A.L. Roytburd. Self-assembled multiferroic nanostructures in the $CoFe_2O_4$-$PbTiO_3$ system. *Applied Physics Letters*, 87(7):072909, 2005.

[69] J. Gao, L. Shen, Y. Wang, D. Gray, J. Li, and D. Viehland. Enhanced sensitivity to direct current magnetic field changes in metglas/$Pb(Mg_{1/3}Nb_{2/3})O_3$-$PbTiO_3$ laminates. *Journal of Applied Physics*, 109(7):074507, 2011.

[70] R. M. Bozorth and J. G. Walker. Magnetostriction of single crystals of cobalt and nickel ferrites. *Physical Review*, 88:1209–1209, 1952.

[71] A. Muhammad, S.R. Turtelli, M. Kriegisch, R. Grössinger, F. Kubel, and T. Konegger. Large enhancement of magnetostriction due to compaction hydrostatic pressure and magnetic annealing in $CoFe_2O_4$. *Journal of Applied Physics*, 111(1):013918, 2012.

[72] V.L. Mathe and A.D. Sheikh. Magnetostrictive properties of nanocrystalline Co-Ni ferrites. *Physica B: Condensed Matter*, 405(17):3594–3598, 2010.

[73] O. Caltun, I. Dumitru, M. Feder, N. Lupu, and H. Chiriac. Substituted cobalt ferrites for sensors applications. *Journal of Magnetism and*

Magnetic Materials, 320(20):e869–e873, 2008. Proceedings of the 18th International Symposium on Soft Magnetic Materials.

[74] K.H. Rao B. P. Rao C. Kim C. Kim I. Dumitru N. Lupu O.F. Caltun, G.S.N. Rao and H. Chiriac. High magnetostrictive cobalt ferrite for sensor application. *Sensor Letters*, 5:1–3, 2007.

[75] A. Grunwald and A.G. Olabi. Design of a magnetostrictive (MS) actuator. *Sensors and Actuators A: Physical*, 144(1):161–175, 2008.

[76] F. Claeyssen, N. Lhermet, R. L. Letty, and P. Bouchilloux. Actuators, transducers and motors based on giant magnetostrictive materials. *Journal of Alloys and Compounds*, 258(1):61–73, 1997. International Conference on Giant-Magnetostrictive.

[77] O. Caltun, G.S.N. Rao, K.H. Rao, B. P. Rao, I. Dumitru, C.-O. Kim, and C. Kim. The influence of mn doping level on magnetostriction coefficient of cobalt ferrite. *Journal of Magnetism and Magnetic Materials*, 316(2):e618–e620, 2007. Proceedings of the Joint European Magnetic Symposia.

[78] G. Engdahl. *Handbook of Giant Magnetostrictive Materials*. Academic Press, 2000.

[79] E. Burcsu, G. Ravichandran, and K. Bhattacharya. Large electrostrictive actuation of barium titanate single crystals. *Journal of the Mechanics and Physics of Solids*, 52(4):823–846, 2004.

[80] Z.Y. Meng, U. Kumar, and L.E. Cross. Electrostriction in lead lanthanum zirconate-titanate ceramics. *Journal of the American Ceramic Society*, 68(8):459–462, 1985.

[81] E. Burcsu, G. Ravichandran, and K. Bhattacharya. Large strain electrostrictive actuation in barium titanate. *Applied Physics Letters*, 77(11):1698–1700, 2000.

[82] Z.-Y. Cheng, V. Bharti, T.-B. Xu, H. Xu, T. Mai, and Q.M. Zhang. Electrostrictive poly(vinylidene fluoride-trifluoroethylene) copolymers. *Sensors and Actuators A: Physical*, 90(1-2):138–147, 2001.

[83] JingboZhao, S. Qu, H. Du, Y. Zheng, and Z. Xu. Preparation and temperature dependence of electrostriction properties for PMN-based composite ceramics. *Materials Science and Engineering: B*, 162(1):9–13, 2009.

[84] J. Van Suchetelene. Product properties: a new application of composite materials. *Philips Research Reports*, 27:28–37, 1972.

[85] A. von Hippel, R.G. Breckenridge, F.G. Chesley, and L. Tisza. High dielectric constant ceramics. *Industrial & Engineering Chemistry*, 38(11):1097–1109, 1946.

[86] H.F. Kay and P. Vousden. Xcv. symmetry changes in barium titanate at low temperatures and their relation to its ferroelectric properties. *Philosophical Magazine Series 7*, 40(309):1019–1040, 1949.

[87] A. Franco and F.C. e Silva. High temperature magnetic properties of cobalt ferrite nanoparticles. *Applied Physics Letters*, 96(17):172505, 2010.

[88] G.A. Sawatzky, F. VAN DER Woude, and A.H. Morrish. Cation distributions in octahedral and tetrahedral sites of the ferrimagnetic spinel $CoFe_2O_4$. *Journal of Applied Physics*, 39(2):1204–1205, 1968.

[89] S. K. Banerjee and B. M. Moskowitz. Ferrimagnetic properties of magnetite, in magnetite biomineralization and magnetoreception in organisms. *A New Magnetism*, pages 17–41, 1985.

[90] H.S. Mund, S. Tiwari, J. Sahariya, M. Itou, Y. Sakurai, and B.L. Ahuja. Investigation of orbital magnetization in inverse spinel cobalt

ferrite using magnetic compton scattering. *Journal of Applied Physics*, 110(7):073914, 2011.

[91] A. Goldman. *Handbook of modern ferromagnetic materials*. Kluwer Academic Publishers, 1999.

[92] Y. Zhang, Y. Liu, C. Fei, Yang Z, Z. Lu, R. Xiong, D. Yin, and J. Shi. The temperature dependence of magnetic properties for cobalt ferrite nanoparticles by the hydrothermal method. *Journal of Applied Physics*, 108(8):084312, 2010.

[93] R.M. Mohamed, M.M. Rashad, F.A. Haraz, and W. Sigmund. Structure and magnetic properties of nanocrystalline cobalt ferrite powders synthesized using organic acid precursor method. *Journal of Magnetism and Magnetic Materials*, 322(14):2058–2064, 2010.

[94] G. Baldi, D. Bonacchi, C. Innocenti, G. Lorenzi, and C. Sangregorio. Cobalt ferrite nanoparticles: The control of the particle size and surface state and their effects on magnetic properties. *Journal of Magnetism and Magnetic Materials*, 311(1):10–16, 2007. Proceedings of the Sixth International Conference on the Scientific and Clinical Applications of Magnetic Carriers SCAMC-06.

[95] B.G. Toksha, S. E. Shirsath, S.M. Patange, and K.M. Jadhav. Structural investigations and magnetic properties of cobalt ferrite nanoparticles prepared by sol-gel auto combustion method. *Solid State Communications*, 147(11-12):479–483, 2008.

[96] V. Kumar, A. Rana, M.S. Yadav, and R.P. Pant. Size-induced effect on nano-crystalline $CoFe_2O_4$. *Journal of Magnetism and Magnetic Materials*, 320(11):1729–1734, 2008.

[97] Y. Wang, J. Hu, Y. Lin, and C.-W. Nan. Multiferroic magnetoelectric composite nanostructures. *NPG Asia Materials*, 2:61–68, 2010.

[98] J. W. Cahn. On spinodal decomposition. *Acta Metallurgica*, 9(9):795–801, 1961.

[99] A.M.J.G. Van Run, D.R. Terrell, and J.H. Scholing. An in situ grown eutectic magnetoelectric composite material. *Journal of Materials Science*, 9(10):1710–1714, 1974.

[100] M. Rafique, S. Q. Ul-Hassan, M.S. Awan, and S. Manzoor. Dependence of magnetoelectric properties on the magnetostrictive content in 0-3 composites. *Ceramics International*, 39, Supplement 1(0):S213–S216, 2013. The 8th Asian Meeting on Electroceramics (AMEC-8).

[101] V. Giap, R. Groessinger, and R.S. Tuertelli. Magnetoelectric properties of $CoFe_2O_4$-$BaTiO_3$ core-shell structure composites. In *Magnetics Conference, 2006. INTERMAG 2006. IEEE International*, pages 830–830, 2006.

[102] L.M. Hrib and O.F. Caltun. Effects of the chemical composition of the magnetostrictive phase on the dielectric and magnetoelectric properties of cobalt ferrite-barium titanate composites. *Journal of Alloys and Compounds*, 509(23):6644–6648, 2011.

[103] S. Agarwal, O.F. Caltun, and K. Sreenivas. Magneto electric effects in $BaTiO_3$-$CoFe_2O_4$ bulk composites. *Solid State Communications*, 152:1951–1955, 2012.

[104] V.V. Shvartsman, F. Alawneh, P. Borisov, D. Kozodaev, and D.C. Lupascu. Converse magnetoelectric effect in $CoFe_2O_4$-$BaTiO_3$ composites with a core shell structure. *Smart Materials and Structures*, 20(7):075006, 2011.

[105] D. Bueno-Baques, R. Grossinger, M. Schonhart, G. Doung, R. Sato, V. Corral-Flores, and J. Matutes-Aquino. The magnetoelectric effect in pulsed magnetic fields. *Journal of Applied Physics*, 99(8):08D908, 2006.

[106] J. Nie, G. Xu, Y. Yang, and C. Cheng. Strong magnetoelectric coupling in $CoFe_2O_4$-$BaTiO_3$ composites prepared by molten-salt synthesis method. *Materials Chemistry and Physics*, 115(1):400–403, 2009.

[107] V. Corral-Flores, D. Bueno-Baqués, D. Carrillo-Flores, and J.A. Matutes-Aquino. Enhanced magnetoelectric effect in core-shell particulate composites. *Journal of Applied Physics*, 99(8):08J503, 2006.

[108] V. Corral-Flores, D. Bueno-Baqués, and R.F. Ziolo. Synthesis and characterization of novel $CoFe_2O_4$-$BaTiO_3$ multiferroic core-shell type nanostructures. *Acta Materialia*, 58(3):764–769, 2010.

[109] C.-W. Nan. Magnetoelectric effect in composites of piezoelectric and piezomagnetic phases. *Physical Review B*, 50:6082–6088, 1994.

[110] K. Raidongia, A. Nag, A. Sundaresan, and C.N.R. Rao. Multiferroic and magnetoelectric properties of core-shell $CoFe_2O_4$-$BaTiO_3$ nanocomposites. *Applied Physics Letters*, 97(6):062904, 2010.

[111] F. Bai, H. Zhang, J. Li, and D. Viehland. Magnetic and magnetoelectric properties of as-deposited and annealed $BaTiO_3$-$CoFe_2O_4$ nanocomposite thin films. *Journal of Physics D: Applied Physics*, 43(28):285002, 2010.

[112] W. Heywang, K. Lubitz, and W. Wersing. *Piezoelectricity: Evolution and Future of a Technology*. Springer Series in Materials Science. Springer Berlin Heidelberg, 2008.

[113] R.A. Islam, V. Bedekar, N. Poudyal, J.P. Liu, and S. Priya. Magnetoelectric properties of core-shell particulate nanocomposites. *Journal of Applied Physics*, 104(10):104111, 2008.

[114] L. Alexander and H. P. Klug. Determination of crystallite size with the x-ray spectrometer. *Journal of Applied Physics*, 21(2):137–142, 1950.

[115] Y. Martin and H.K. Wickramasinghe. Magnetic imaging by force microscopy with 1000 angstrom resolution. *Applied Physics Letters*, 50(20):1455–1457, 1987.

[116] D. Rugar, H.J. Mamin, P. Guethner, S.E. Lambert, J.E. Stern, I. McFadyen, and T. Yogi. Magnetic force microscopy: General principles and application to longitudinal recording media. *Journal of Applied Physics*, 68(3):1169–1183, 1990.

[117] Y.-A. Soh, G. Aeppli, N.D. Mathur, and M.G. Blamire. Magnetic phase transitions studied by magnetic force microscopy. *Journal of Magnetism and Magnetic Materials*, 226-230, Part 1(0):857–859, 2001. Proceedings of the International Conference on Magnetism (ICM 2000).

[118] T.K. Song, Y.W. So, D.J. Kim, J.Y. Jo, and T.W. Noh. Ferroelectric switching dynamics and pulse-switching polarization measurements. *Integrated Ferroelectrics*, 78(1):191–197, 2006.

[119] J.A. Giacometti, C. Wisniewski, W.A. Moura, and P.A. Ribeiro. Constant current: A method for obtaining hysteresis loops in ferroelectric materials. *Review of Scientific Instruments*, 70(6):2699–2702, 1999.

[120] V.M. Petrov, M.I. Bichurin, and G. Srinivasan. Maxwell-Wagner relaxation in magnetoelectric composites. *Technical Physics Letters*, 30(4):341–344, 2004.

[121] R. Nagendran, N. Thirumurugan, N. Chinnasamy, M.P. Janawadkar, and C.S. Sundar. Development of high field squid magnetometer for magnetization studies up to 7 T and temperatures in the range from 4.2 to 300 K. *Review of Scientific Instruments*, 82(1):015109, 2011.

[122] U. Gonser. *Topics in Applied Physics: Mössbauer spectroscopy*, volume 5. Springer-Verlag Berlin Heidelberg, 1975.

[123] R.S. Singh, T. Bhimasankaram, G.S. Kumar, and S.V. Suryanarayana. Dielectric and magnetoelectric properties of $Bi_5FeTi_3O_{15}$. *Solid State Communications*, 91(7):567–569, 1994.

[124] G.V. Duong, R.S. Turtelli, and R. Groessinger. Magnetoelectric properties of $CoFe_2O_4$-$BaTiO_3$ core-shell structure composite studied by a magnetic pulse method. *Journal of Magnetism and Magnetic Materials*, 322(9-12):1581–1584, 2010. Proceedings of the Joint European Magnetic Symposia.

[125] M. M. Kumar, A. Srinivas, S.V. Suryanarayana, G.S. Kumar, and T. Bhimasankaram. An experimental setup for dynamic measurement of magnetoelectric effect. *Bulletin of Materials Science*, 21(3):251–255, 1998.

[126] V. G. Duong, R. Groessinger, M. Schoenhart, and D. Bueno-Basques. The lock-in technique for studying magnetoelectric effect. *Journal of Magnetism and Magnetic Materials*, 316(2):390–393, 2007. Proceedings of the Joint European Magnetic Symposia.

[127] Y.K. Fetisov, K.E. Kamentsev, A.Y. Ostashchenko, and G. Srinivasan. Wide-band magnetoelectric characterization of a ferrite-piezoelectric multilayer using a pulsed magnetic field. *Solid State Communications*, 132(1):13–17, 2004.

[128] E. Kita, A. Tasaki, and K. Siratori. Application of squid magnetometer to the measurement of magnetoelectric effect in Cr_2O_3. *Japanese Journal of Applied Physics*, 18(7):1361, 1979.

[129] P. Borisov, A. Hochstrat, V.V. Shvartsman, and W. Kleemann. Superconducting quantum interference device setup for magnetoelectric measurements. *Review of Scientific Instruments*, 78(10):106105, 2007.

[130] Helmholtz-Zentrum Berlin (HZB). http://www.helmholtz-berlin.de/.

[131] C. Schmitz-Antoniak, D. Schmitz, P. Borisov, F.M.F. de Groot, S. Stienen, A. Warland, B. Krumme, R. Feyerherm, E. Dudzik, W. Kleemann, and H. Wende. Electric in-plane polarization in multiferroic $CoFe_2O_4/BaTiO_3$ nanocomposite tuned by magnetic fields. *Nature Communications*, 4, 2013.

[132] M.M. El-Okr, M.A. Salem, M.S. Salim, R.M. El-Okr, M. Ashoush, and H.M. Talaat. Synthesis of cobalt ferrite nano-particles and their magnetic characterization. *Journal of Magnetism and Magnetic Materials*, 323(7):920–926, 2011.

[133] Y. Zhang, Z. Yang, D. Yin, Y. Liu, C. Fei, R. Xiong, J. Shi, and G. Yan. Composition and magnetic properties of cobalt ferrite nano-particles prepared by the co-precipitation method. *Journal of Magnetism and Magnetic Materials*, 322(21):3470–3475, 2010.

[134] Z. Zi, Y. Sun, X. Zhu, Z. Yang, J. Dai, and W. Song. Synthesis and magnetic properties of $CoFe_2O_4$ ferrite nanoparticles. *Journal of Magnetism and Magnetic Materials*, 321(9):1251–1255, 2009.

[135] K. Maaz, A. Mumtaz, S.K. Hasanain, and A. Ceylan. Synthesis and magnetic properties of cobalt ferrite ($CoFe_2O_4$) nanoparticles prepared by wet chemical route. *Journal of Magnetism and Magnetic Materials*, 308(2):289–295, 2007.

[136] N. Hanh, O.K. Quy, N.P. Thuy, L.D. Tung, and L. Spinu. Synthesis of cobalt ferrite nanocrystallites by the forced hydrolysis method and investigation of their magnetic properties. *Physica B: Condensed Matter*, 327(2-4):382–384, 2003. Proceedings of the International Symposium on Advanced Magnetic M aterials.

[137] T. Meron, Y. Rosenberg, Y. Lereah, and G. Markovich. Synthesis and assembly of high-quality cobalt ferrite nanocrystals prepared by a modified sol-gel technique. *Journal of Magnetism and Magnetic Materials*, 292(0):11–16, 2005.

[138] Y. Köseoğlu, F. Alan, M. Tan, R. Yilgin, and M. öztürk. Low temperature hydrothermal synthesis and characterization of Mn doped cobalt ferrite nanoparticles. *Ceramics International*, 38(5):3625–3634, 2012.

[139] National bureau of standards monograph, 25,9, 1971.

[140] E.P. Wohlfarth. *Ferromagnetic Materials*, volume 3. Elsevier Science Publishers, 1982.

[141] M.F. Etier, V.V. Shvartsman, F. Stromberg, J. Landers, H. Wende, and D.C. Lupascu. Synthesis and magnetic properties of cobalt ferrite nanoparticles. In *Symposium Q - Magnetoelectric Composites*, volume 1398 of *MRS Proceedings*, 2012.

[142] S. Imine, F. Schoenstein, S. Mercone, M. Zaghrioui, N. Bettahar, and N. Jouini. Bottom-up and new compaction processes: A way to tunable properties of nanostructured cobalt ferrite ceramics. *Journal of the European Ceramic Society*, 31(15):2943–2955, 2011.

[143] R.H Kodama. Magnetic nanoparticles. *Journal of Magnetism and Magnetic Materials*, 200(1-3):359 – 372, 1999.

[144] T. Ibusuki, S. Kojima, O. Kitakami, and Y. Shimada. Magnetic anisotropy and behaviors of fe nanoparticles. *IEEE Transactions on Magnetics*, 37(4):2223–2225, 2001.

[145] E. De Grave, R.M. Persoons, R.E. Vandenberghe, and P.M.A. de Bakker. Mössbauer study of the high-temperature phase of Co-substituted magnetites, $Co_xFe_{3-x}O_4$. i. x≤0.04. *Physical Review B*, 47:5881–5893, 1993.

[146] M. Bibes and A. Barthelemy. Multiferroics: Towards a magnetoelectric memory. *Nature Materials*, 7(6):425–426, 2008.

[147] K. Yue, R. Guduru, J. Hong, P. Liang, M. Nair, and S. Khizroev. Magneto-electric nano-particles for non-invasive brain stimulation. *Public Library of Science ONE*, 7(9):e44040, 2012.

[148] R. Liu, Y. Zhao, R. Huang, Y. Zhao, and H. Zhou. Multiferroic ferrite/perovskite oxide core/shell nanostructures. *Journal of Materials Chemistry*, 20:10665–10670, 2010.

[149] M. Etier, Y. Gao, V.V. Shvartsman, A. Elsukova, J. Landers, H. Wende, and D.C. Lupascu. Cobalt ferrite/barium titanate core/shell nanoparticles. *Ferroelectrics*, 438(1):115–122, 2012.

[150] Yanling Gao, Vladimir V. Shvartsman, Anna Elsukova, and Doru C. Lupascu. Low-temperature synthesis of crystalline $BaTiO_3$ nanoparticles by one-step "organosol"-precipitation. *Journal of Materials Chemistry*, 22:17573–17583, 2012.

[151] H.-W. Lee, S. Moon, C.-H. Choi, and D. K. Kim. Synthesis and size control of tetragonal barium titanate nanopowders by facile solvothermal method. *Journal of the American Ceramic Society*, 95(8):2429–2434, 2012.

[152] M. Etier, V.V. Shvartsman, Y. Gao, J. Landers, H. Wende, and D.C. Lupascu. Magnetoelectric effect in (0-3) $CoFe_2O_4$-$BaTiO_3$(20/80) composite ceramics prepared by the organosol route. *Ferroelectrics*, 448(1):77–85, 2013.

[153] Z. Zhao, V. Buscaglia, M. Viviani, M.T. Buscaglia, L. Mitoseriu, A. Testino, M. Nygren, M. Johnsson, and P. Nanni. Grain-size effects on the ferroelectric behavior of dense nanocrystalline $BaTiO_3$ ceramics. *Physical Review B*, 70:024107, 2004.

[154] G. Concas, G. Spano, C. Cannas, A. Musinu, D. Peddis, and G. Piccaluga. Inversion degree and saturation magnetization of different nanocrystalline cobalt ferrites. *Journal of Magnetism and Magnetic Materials*, 321(12):1893–1897, 2009.

[155] P. Didukh, J.M. Greneche, A. Ślawska-Waniewska, P.C. Fannin, and Ll. Casas. Surface effects in $CoFe_2O_4$ magnetic fluids studied by mössbauer spectrometry. *Journal of Magnetism and Magnetic Materials*, 242-245, Part 1(0):613–616, 2002. Proceedings of the Joint European Magnetic Symposia (JEMS'01).

[156] H.-I. Hsiang and F.-S. Yen. Effect of crystallite size on the ferroelectric domain growth of ultrafine $BaTiO_3$ powders. *Journal of the American Ceramic Society*, 79(4):1053–1060, 1996.

[157] M.B. Smith, K. Page, T. Siegrist, P.L. Redmond, E.C. Walter, R. Seshadri, L.E. Brus, and M.L. Steigerwald. Crystal structure and the paraelectric-to-ferroelectric phase transition of nanoscale $BaTiO_3$. *Journal of the American Chemical Society*, 130(22):6955–6963, 2008.

[158] H. Neumann and G. Arlt. Maxwell-wagner relaxation and degradation of $SrTiO_3$ and $BaTiO_3$ ceramics. *Ferroelectrics*, 69(1):179–186, 1986.

[159] P. Jeppson, R. Sailer, E. Jarabek, J. Sandstrom, B. Anderson, M. Bremer, D.G. Grier, D.L. Schulz, A. N. Caruso, S.A. Payne, P. Eames, M. Tondra, H. He, and D.B. Chrisey. Cobalt ferrite nanoparticles: Achieving the superparamagnetic limit by chemical reduction. *Journal of Applied Physics*, 100(11):114324, 2006.

[160] E.C. Stoner and E.P. Wohlfarth. A mechanism of magnetic hysteresis in heterogeneous alloys. *Philosophical Transactions of the Royal Society of London A: Mathematical, Physical and Engineering Sciences*, 240(826):599–642, 1948.

[161] H. Trivedi, V.V. Shvartsman, D.C. Lupascu, M.S.A. Medeiros, R.C. Pullar, A.L. Kholkin, P. Zelenovskiy, A. Sosnovskikh, and V.Y. Shur. Local manifestations of a static magnetoelectric effect in nanostructured $BaTiO_3$-$BaFe_{12}O_9$ composite multiferroics. *Nanoscale*, 7:4489–4496, 2015.

[162] L. Dong, D.S. Stone, and R. S. Lakes. Enhanced dielectric and piezoelectric properties of x$BaZrO_3$-(1-x)$BaTiO_3$ ceramics. *Journal of Applied Physics*, 111(8):084107, 2012.

[163] F.D. Ma, Y.M. Jin, Y.U. Wang, S.L. Kampe, and S. Dong. Phase field modeling and simulation of particulate magnetoelectric composites: Effects of connectivity, conductivity, poling and bias field. *Acta Materialia*, 70(0):45–55, 2014.

[164] I.C. Nlebedim, N. Ranvah, Y. Melikhov, P.I. Williams, J.E. Snyder, A.J. Moses, and D.C. Jiles. Effect of temperature variation on the magnetostrictive properties of $CoAl_xFe_{2-x}O_4$. *Journal of Applied Physics*, 107(9):09A936, 2010.

[165] B. Gojdka, V. Hrkac, J. Xiong, M. Gerken, L. Kienle, T. Strunskus, V. Zaporojtchenko, and F. Faupel. A critical evaluation of the 0-3 approach for magnetoelectric nanocomposites with metallic nanoparticles. *Journal of Applied Physics*, 112(4):044303, 2012.

[166] I.C. Nlebedim and D.C. Jiles. Dependence of the magnetostrictive properties of cobalt ferrite on the initial powder particle size distribution. *Journal of Applied Physics*, 115(17):17A928, 2014.

[167] S. Chikazumi. *Physics of Ferromagnetism*. Oxford university press Inc., New York, 1997.

[168] D.-X. Chen, E. Pardo, and A. Sanchez. Fluxmetric and magnetometric

demagnetizing factors for cylinders. *Journal of Magnetism and Magnetic Materials*, 306(1):135–146, 2006.

[169] U. Laletin, G. Sreenivasulu, V.M. Petrov, T. Garg, A.R. Kulkarni, N. Venkataramani, and G. Srinivasan. Hysteresis and remanence in magnetoelectric effects in functionally graded magnetostrictive-piezoelectric layered composites. *Physical Review B*, 85:104404, 2012.

[170] R. Skomski, G.C. Hadjipanayis, and D.J. Sellmyer. Effective demagnetizing factors of complicated particle mixtures. *IEEE Transactions on Magnetics*, 43(6):2956–2958, 2007.

[171] S.D. Bhame and P.A. Joy. Enhanced magnetostrictive properties of $CoFe_2O_4$ synthesized by an autocombustion method. *Sensors and Actuators A: Physical*, 137(2):256–261, 2007.

[172] Yu Huan, Xiaohui Wang, Jian Fang, and Longtu Li. Grain size effects on piezoelectric properties and domain structure of $BaTiO_3$ ceramics prepared by two-step sintering. *Journal of the American Ceramic Society*, 96(11):3369–3371, 2013.

[173] M. Labusch, M. Etier, D.C. Lupascu, J. Schröder, and M.-A. Keip. Product properties of a two-phase magneto-electric composite: Synthesis and numerical modeling. *Computational Mechanics*, 54(1):71–83, 2014.

[174] J. Lou, G.N. Pellegrini, M. Liu, N.D. Mathur, and N.X. Sun. Equivalence of direct and converse magnetoelectric coefficients in strain-coupled two-phase systems. *Applied Physics Letters*, 100(10):102907, 2012.

[175] P. Record, C. Popov, J. Fletcher, E. Abraham, Z. Huang, H. Chang, and R.W. Whatmore. Direct and converse magnetoelectic effect in laminate bonded terfenol-D-PZT composites. *Sensors and Actuators B: Chemical*, 126(1):344–349, 2007. Functional Materials for Micro and Nanosystems

{EMRS} Containing Selected papers from the European Materials research Society (E-MRS 2006) Symposium G:.

[176] C. Popov, H. Chang, P.M. Record, E. Abraham, R.W. Whatmore, and Z. Huang. Direct and converse magnetoelectric effect at resonant frequency in laminar piezoelectric-magnetostrictive composite. *Journal of Electroceramics*, 20(1):53–58, 2008.

[177] T. Wu, C.-M. Chang, T.-K. Chung, and G. Carman. Comparison of effective direct and converse magnetoelectric effects in laminate composites. *Magnetics, IEEE Transactions on*, 45(10):4333–4336, 2009.

[178] M. Etier, C. Schmitz-Antoniak, S. Salamon, H. Trivedi, Y. Gao, A. Nazrabi, J. Landers, D. Gautam, M. Winterer, D. Schmitz, H. Wende, V.V. Shvartsman, and D.C. Lupascu. Magnetoelectric coupling on multiferroic cobalt ferrite-barium titanate ceramic composites with different connectivity schemes. *Acta Materialia*, 90(0):1–9, 2015.

[179] S. Polisetty, J. Zhou, J. Karthik, A.R. Damodaran, D. Chen, A. Scholl, L.W. Martin, and M. Holcomb. X-ray linear dichroism dependence on ferroelectric polarization. *Journal of Physics: Condensed Matter*, 24(24):245902, 2012.

[180] Y.X. Zheng, Q.Q. Cao, C.L. Zhang, H.C. Xuan, L.Y. Wang, D.H. Wang, and Y.W. Du. Study of uniaxial magnetism and enhanced magnetostriction in magnetic-annealed polycrystalline $CoFe_2O_4$. *Journal of Applied Physics*, 110(4):043908, 2011.

[181] G. Srinivasan, E.T. Rasmussen, and R. Hayes. Magnetoelectric effects in ferrite-lead zirconate titanate layered composites: The influence of zinc substitution in ferrites. *Physical Review B*, 67:014418, 2003.